REPORT DOCUMENTATION PAGE

Form Approved OMB NO. 0704-0188

1. REPORT DATE (DD-MM-YYYY)	2. REPORT TYPE	3. DATES COVERED (From - To)
12-05-2018	Final Report	15-Aug-2015 - 14-Aug-2016

4. TITLE AND SUBTITLE

Final Report: DURIP: In situ Solute and Grain Character Mapping of Nanocrystalline Alloys at Elevated Temperatures using Sub-Second Heating Capability

5a. CONTRACT NUMBER
W911NF-15-1-0405

5b. GRANT NUMBER

5c. PROGRAM ELEMENT NUMBER
611103

6. AUTHORS

5d. PROJECT NUMBER

5e. TASK NUMBER

5f. WORK UNIT NUMBER

7. PERFORMING ORGANIZATION NAMES AND ADDRESSES

University of Alabama - Tuscaloosa
Box 870104

Tuscaloosa, AL 35487 -0104

8. PERFORMING ORGANIZATION REPORT NUMBER

9. SPONSORING/MONITORING AGENCY NAME(S) AND ADDRESS (ES)

U.S. Army Research Office
P.O. Box 12211
Research Triangle Park, NC 27709-2211

10. SPONSOR/MONITOR'S ACRONYM(S)
ARO

11. SPONSOR/MONITOR'S REPORT NUMBER(S)
66908-MS-RIP.1

12. DISTRIBUTION AVAILIBILITY STATEMENT

Approved for public release; distribution is unlimited.

13. SUPPLEMENTARY NOTES

The views, opinions and/or findings contained in this report are those of the author(s) and should not contrued as an official Department of the Army position, policy or decision, unless so designated by other documentation.

14. ABSTRACT

15. SUBJECT TERMS

16. SECURITY CLASSIFICATION OF:			17. LIMITATION OF ABSTRACT	15. NUMBER OF PAGES	19a. NAME OF RESPONSIBLE PERSON
a. REPORT	b. ABSTRACT	c. THIS PAGE			Gregory Thompson
UU	UU	UU	UU		19b. TELEPHONE NUMBER 205-348-1589

RPPR Final Report
as of 04-Jun-2018

Agency Code:

Proposal Number: 66908MSRIP **Agreement Number: W911NF-15-1-0405**
INVESTIGATOR(S):

Name: Gregory Thompson
Email: gthompson@eng.ua.edu
Phone Number: 2053481589
Principal: Y

Organization: **University of Alabama - Tuscaloosa**
Address: Box 870104, Tuscaloosa, AL 354870104
Country: USA
DUNS Number: 045632635 EIN: 636001138
Report Date: 14-Nov-2016 Date Received: 12-May-2018
Final Report for Period Beginning 15-Aug-2015 and Ending 14-Aug-2016
Title: DURIP: In situ Solute and Grain Character Mapping of Nanocrystalline Alloys at Elevated Temperatures using Sub-Second Heating Capability
Begin Performance Period: 15-Aug-2015 **End Performance Period:** 14-Aug-2016
Report Term: 0-Other
Submitted By: Gregory Thompson Email: gthompson@eng.ua.edu
Phone: (205) 348-1589
Distribution Statement: 1-Approved for public release; distribution is unlimited.

STEM Degrees: 2 **STEM Participants:** 4

Major Goals: Nanocrystalline materials have received considerable attention for their size dependent properties. Much of these attributes rely on the stability of the nano-grains. Recent efforts have shown the use of solute segregates as a means to stabilize these structures.

This grant enabled the acquisition of a rapid thermal annealing unit (105 oC/sec.) and a rapid X-ray energy dispersive spectroscopy (chemical) detector to be coupled with an existing precession electron diffraction system to provide a combined platform that will link site specific grain boundary character to solute composition. This structural and chemical connection enabled these microstructural features to be characterized in situ at elevated temperatures. This has provided for direct, real-time quantification of specific grain types that are stabilized or destabilized effects under annealing with respect to the solute additions. In addition, residual oxygen present in the TEM allowed the early stages of oxidation to be observed, and linked, to the grain boundary evolution. The use of this instrumentation was applied to a prior ARO grant - W911NF1310436 – where the work shared here was also reported in that grant's final report.

In the subsequent section, the use of this instrumentation is illustrated with respect to the oxidation behavior in an Fe(Cr) nanocrystalline alloy. The DURIP award is now being applied to a new ARO effort - W911NF1710528 – studying the effects of solutes on nanogranular stability.

Accomplishments: Per the request in the proposal, the following instruments was acquired. (1) DENSsolution in situ heating platform – Single Tilt holder SH30. And (2) EDAX Octane TEAM Silicon Drift Detector System and Platform.

As will be shown in the subsequent (uploaded) section, we have successfully demonstrated the linkage of chemical mapping to grain boundary type and its evolution under heating. In the shown example, the early stages of oxidation is presented in a Fe(Cr) nanocrystalline film. The results revealed that the Fe-4Cr (at%) formed Cr2O3 oxides precipitates within the grain whereas the Fe-16Cr sample revealed oxidation on the grain boundaries, with high angle grain boundaries being the preferred nucleation site. The growth of the oxide rapidly occurred along these boundaries, whereas special character boundaries were less sensitive to the initial oxidation reaction, which is suspected to be a result of solute segregation specificity to grain boundaries.

RPPR Final Report
as of 04-Jun-2018

Training Opportunities: The following graduate students have been trained in the use of the SSD, who are members of Prof. Thompson's research group.

Thomas Koenig
Xuyang (Rhett) Zhou
Tyler Kaub
Dallin Barton
Alicia Wadsworth

Prof. Thompson also taught MTE 655 Transmission Electron Microscopy in the Spring 2017 term and trained 16 additional graduate students in the use of this equipment.

Results Dissemination: The following paper is currently under review:

Xuyang Zhou and Gregory B. Thompson “In situ TEM observations of initial oxidation behavior in Fe-rich Fe-Cr alloys” submitted to Journal of Materials Science (2018).

Professor Thompson gave an invited talk at the Materials Science & Technology Meeting in Fall 2016 entitled "Cross-correlative Precession Electron Diffraction: ♂A study on solute-grain boundary segregation." In this talk, this equipment was demonstrated. The slides of which are included in the uploaded section.

Professor Thompson also gave a seminar at U. of Sydney entitled "Application of Precession Electron Diffraction to Cross-Correlative in situ Microscopy." In this lecture, this equipment was again demonstrated. This seminar was given on M, April 30, 2018. The slides of which are included in the uploaded section.

Honors and Awards: 2017 – Professor Gregory B. Thompson was recognized at The Minerals Metals and Materials Society Brimacombe Medalist, with the citation reading “ For notable contributions in linking analytical microscopy with phase and property studies across materials and length scales, commitment to STEM education, and service to TMS.”

Protocol Activity Status:

Technology Transfer: Nothing to Report

PARTICIPANTS:

Participant Type: PD/PI
Participant: Gregory Bruce Thompson
Person Months Worked: 1.00
Project Contribution:
International Collaboration:
International Travel:
National Academy Member: N
Other Collaborators:

Funding Support:

RPPR Final Report
as of 04-Jun-2018

In situ TEM observations of initial oxidation behavior in Fe-rich Fe-Cr alloys

Xuyang Zhou[*,1] and Gregory B. Thompson[1]

[1]The University of Alabama, Department of Metallurgical & Materials Engineering, Tuscaloosa, AL USA

* Address correspondence to E-mail: xzhou41@crimson.ua.edu, Phone: +1 205-887-3194

ABSTRACT: Two nanocrystalline alloys of Fe-4Cr and Fe-16Cr were sputter deposited and formed a solid solution A2 phase. Each alloy was then in situ annealed up to 800^{o}C with the phase and microstructure quantified by transmission electron microscopy (TEM). The low partial pressure of oxygen in the TEM column ($\sim 2.6 \times 10^{-6}$Pa) oxidized both films at temperatures at and above 700^{o}C. However, the oxide morphologies were quite different. The Fe-4Cr revealed nanosphere Cr oxide clusters within the grains which has been explained by the thermodynamic preference for Cr to be in solution. The Fe-16Cr precipitated distinct Cr_2O_3 grains which has been described by Cr phase separation at the grain boundaries. Iron oxide was not observed and demonstrating Cr's strong preference for oxygen, even in very low oxygen environments. Using precession electron diffraction (PED), the grain characters of these boundaries were determined revealing a significant effect of high angle grain boundaries on the growth and precipitation behavior of the oxides. The collective results reveal the initial stages of oxidation evolution in nanocrystalline grains, the role of Cr content on such behavior.

KEYWORDS: *in situ* transmission electron microscopy, FeCr, oxidation, X-ray energy dispersion spectroscopy, precession electron diffraction

1. Introduction

The Fe-rich Cr alloys provide two of the major constituent components in stainless steels enabling these materials to exhibit decent corrosion resistance and good mechanical properties [1-4]. As a result, these alloys are a critical material for a variety of technologies used in the nuclear, manufacturing, and energy industries [1, 3, 5-8]. Once the Cr content extends 11 at.% in these steels [1], a stable chromia (Cr_2O_3) surface scale will form and provide for passivity protection to the metal [9-13]. If the diffusion is predominated by metal ion transport, this oxide scale, on low-alloy steels, will grow outward by the metal diffusion; if the diffusion is predominated by oxygen

ion diffusion, the oxide scale will then grow inwards into the metal [14]. Besides the metal or oxygen transport type, the formation of the oxide scale is also a kinetic process that will also be related to the temperature and oxygen partial pressure, with the oxidation rates being linear, logarithmic or parabolic dependent on the active mechanism [14]. At high temperatures, the oxidation rate is typically parabolic and is regulated by diffusion through the scale. At such temperatures, the inward diffusion mentioned above contributes substantially to the overall oxidation process by the fast oxygen diffusion along grain boundaries [15]. Since grain boundaries provide high diffusivity pathways, the amount of grain boundary area will then play a critical role in controlling oxidation behavior. This is particularly relevant for nanocrystalline alloys, whose small grain size may be advantageous for higher strengthening but may be more susceptible to rapid oxidation [15]. Besides grain boundaries, phase boundaries can also contribute to enhanced diffusivities as noted in the work by Golden *et al.* who reported a fast path for oxygen to diffuse along phase boundaries [16].

Despite the extensive studies of oxidation and corrosion behavior on Fe-Cr alloys [17-20], capturing the initial stages of oxidation and its effects on the microstructure is still relatively elusive. To date, most characterization of oxidation is done post-mortem requiring one to infer how the final structure was achieved. However, *in situ* microscopy can enable one to track and even quantify real-time reactions, as well as observing potential mechanisms that are only active during the time of the event, that can lead to final microstructure [21-23]. Such imaging capability can provide for new and unique insights to behaviors that can be lost in post-mortem analysis [24-27]. The advent of various temperature and now liquid and gas stages has enabled many of these observations that were previously not seen, to be elucidated. For example, Banerjee *et al.* employed *in situ* environmental transmission electron microscopy (TEM) to monitor the nanoscale growth of Ni on silica-supported metal model catalysts [28] and Unocic *et al.* directly visualized the dynamic structural and chemical changes during high-temperature oxidation of β-NiAl nanoparticles [29].

Here, we extend these studies to quantify how oxidation initiates and evolves as a function of nanocrystalline granular evolution for a low (4 at.%Cr) and high (16 at.% Cr) binary Fe(Cr) alloy. The aim of the study is then to better understand how the initial stages of passivation occurs for different Cr contents and how that evolves in a nanocrystalline metal, as most efforts have been directed towards ‘bulk’ stainless steels. By using a binary system, we also reduce the complexity

of additional interactions with other solutes that may complicate the observed interaction and structural evolution and provide a basis for future studies to compare too. Furthermore, by annealing in a low partial pressure oxygen environment, the rate of oxidation can be reduced enabling the ability to capture this reaction with respect to potential chemical partitioning and structural changes, such as grain growth or grain boundary re-orientations. To quantify these effects, *in situ* imaging needs to be coupled with, for example, rapid X-ray energy dispersion spectroscopy (XEDS) for compositional measurements. To quantify microstructural changes, precession electron diffraction (PED) can provide quantification for both nanoscale grain boundary and grain texture imaging. In particular, both of these techniques – XEDS and PED - are amenable to TEM, which provides the ability to regularly image nanocrystalline granular structures. By applying these complementary techniques, as will be developed in this paper, one will be able to quantitatively understand nanocrystalline stability during passivation and how Cr solute concentration partitions in response for a series of low and high Cr content Fe(Cr) samples.

2. Materials and methods

To fabricate the nanocrystalline alloy, thin films of either Fe-4 at.% Cr or Fe-16 at.% Cr were magnetron sputter deposited in an AJA ATC-1500 system from 99.95% pure pre-alloyed targets. The sputtering rates were found to be approximately 0.100 nm/s for Fe-4Cr and 0.106 nm/s for Fe-16Cr with the deposition rates determined by dividing the film thickness, measured from x-ray reflectivity (XRR) [30], by the deposition time. The XRR was performed on an X'pert Philips diffractometer operated with Cu K_α radiation (λ = 0.15406 nm) at 40 kV and 30 mA. Before deposition, the chamber had a base pressure < 6×10^{-6} Pa evacuated by mechanical and turbo-pumps. High-purity Argon then flowed into the sputtering chamber as the working gas at a rate of 10 standard cubic centimeters per minute to a pressure of 0.27 Pa. The films were grown to an approximate thickness of 40 nm onto SiN_x windows in a DENS® chip [31] at room temperature, which ensured direct electron transparency in the TEM. The DENS® chip is based on a microelectromechanical systems (MEMS) chip that can provide rapid heating/cooling with 0.001 ^{o}C temperature stability, in set images in Figure 1(a) [31]. The low amount of thermal mass to heat also ensures very stable positioning for imaging at temperature (negligible thermal drift) which is advantageous to both chemical mapping and PED collection [32]. The Fe(Cr) films were annealed *in situ* using the chip in the TEM with the heating cycles shown in Figure 1(a). The oxidation

behavior occurred from the partial pressure of oxygen that is present in the TEM column, Figure 1(b), which will further be discussed shortly.

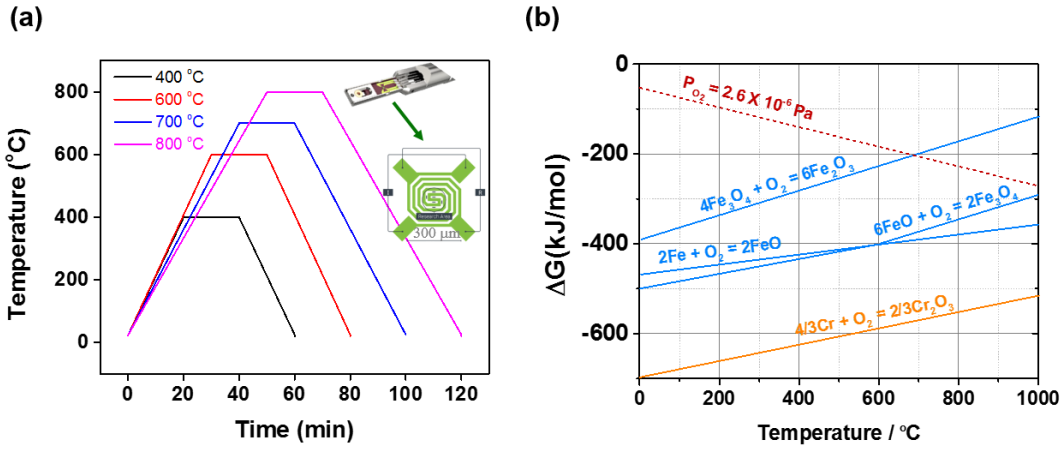

Figure 1 (a) *in situ* heat treatment history and the sketch of a DENS chip included **(b)** Ellingham diagram of Fe and Cr

After deposition, the Fe(Cr) films were immediately transferred into a FEI Tecnai SupertwinF20 (S)TEM. The TEM column evacuated pressure was $\sim 1.2 \times 10^{-5}$Pa, and assuming an air mixture of 78%N_2-22%O_2, the oxygen partial pressure was $\sim 2.6 \times 10^{-6}$Pa. The Ellingham diagram, Figure 1(b), shows that the thermodynamic driving force for oxidation will change with temperature. Thus, the lower oxygen content and the ability to anneal the film provides an ideal situation where the rate of oxidation can be slowed such that the initial stages of oxidation can be captured. Furthermore, under these controlled conditions, the immiscible phase separation between Fe-Cr prior to and after oxidation would reveal the hierarchy of microstructure evolution in these nanocrystalline alloys.

Therefore, we can provide for a very controlled (slow) rate of oxidation by increasing the temperature. Considering that the material is very minimal (required to be a thin foil), this provides a mechanism to study these effects in a controlled manner, particularly if one does not have a specialized gas reaction system. Also, by providing a low O_2 environment, we can observe the phase separation of the Fe-Cr (immiscible system) prior to and after oxidation initiates to determine the hierarchy of the microstructure evolution.

A NanoMEGAS platform on the TEM was employed to conduct PED scans [33-35]. The PED scans were collected using a 0.3° procession angle and a scanning step size of 3 nm, in the same size of region of interest (ROI), which was 800 × 800 nm^2. After scanning, the data was

converted for analysis using TSL OIM Analysis 7 software and analyzed after grain dilation optimization. The composition, in the same ROI, was characterized by XEDS mapping using an EDAX® silicon drift detector (SDD).

3. Results and discussion

Figure 2(a) shows the series of bright field images, diffraction patterns, and PED orientation maps for the Fe-4Cr and Fe-16Cr films at room temperature and annealed settings at 400ºC, 600ºC, 700ºC, and 800ºC. Each image is from the same ROI so specific microstructural features can be tracked. From the diffraction patterns, the Fe-4Cr films only revealed a single body center cubic (bcc) solid solution A2 phase for all temperature conditions. Similarly, the Fe-16Cr film revealed an A2 phase but only up to 600ºC after which additional reflections indexed for the Cr_2O_3 phase [36] were noted at 700ºC and 800ºC.

Orientation maps for the nanocrystalline Fe-4Cr sample revealed a mixture of grain textures evident by the multiple colors seen in the PED scan, Figure 2(a; i-v). Interestingly, as the temperature increased, the grain size was rather invariant with only modest increase in the mean grain size occurred at the highest temperatures, Figure 2(b), which was only a 10% increase from the room temperature film. Furthermore, the multiple textures within the film were maintained. The Fe-16Cr film was quite different. Here, the film adopted a strong [001] fiber texture, Figure 2(a; vi-x), which was also retained throughout the annealing stages. What is particularly interesting in the PED scans is the presence of much smaller [101] grains. As the temperature increased, evident grain growth occurred at 700ºC, Figure 2(b), with several of these smaller [101] grains now consumed by the [001] grains shown in sequence of images in Figure 2(a; vi-viii). With this grain growth, the grain shapes also changed. In the room temperature and lower annealed samples, the grains boundaries are curved; with increasing temperature, these boundaries become much more faceted (linear) between each other, Figure 2(a; x). By 800ºC, the Fe-16Cr mean grain size was ~ 50% larger than the initial grain size with clear oxidation and formation of Cr_2O_3 over portions of the grains, Figure 2(a; x).

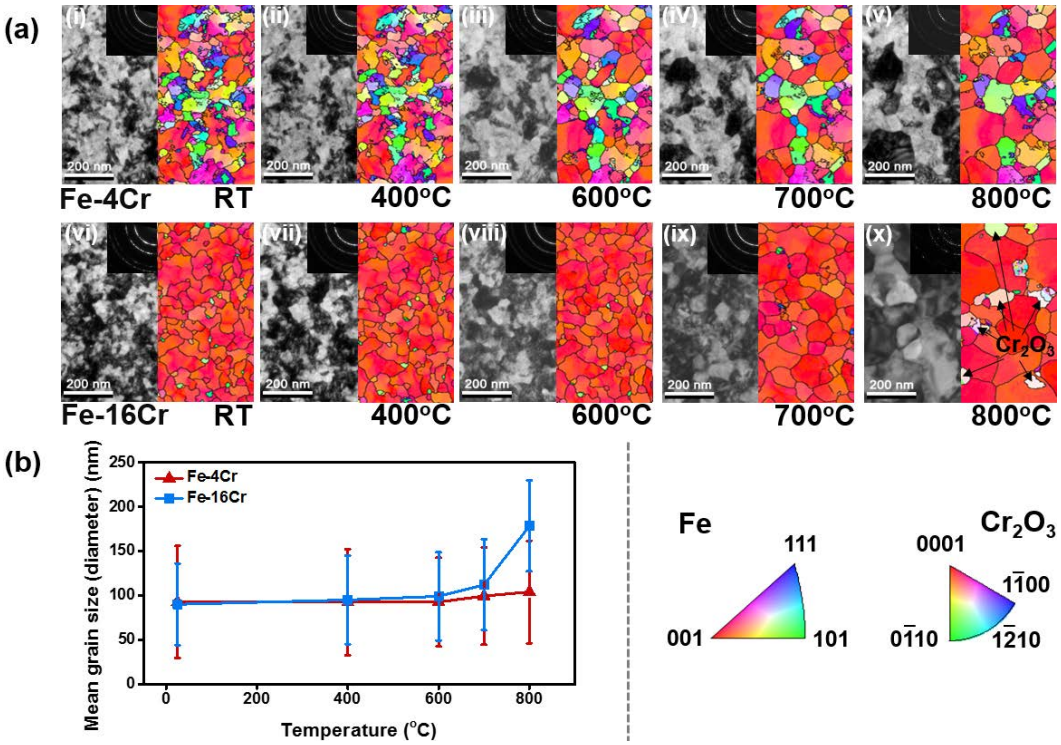

Figure 2 (a) Bright field images, diffraction patterns, and orientation maps of the **(i)-(v)** Fe-4Cr films and the **(vi)-(x)** Fe-16Cr films at RT or annealed at 400°C, 600°C, 700°C, 800°C **(b)** Mean grain size varying with temperatures for the Fe-4Cr and Fe-16Cr films.

This Cr_2O_3 phase was only resolved in the PED scan at the 700°C and 800°C for Fe-16Cr films. However, the favorable formation of chrome oxide as compared to iron oxide, Figure 1(b), would suggest that it should have also reacted with the Fe-4Cr film. A high angle annular dark field (HAADF) image taken over a larger ROI than the prior PED scans is shown in Figure 3(a)-(b). The image clearly reveals dark, very small nanosphere features within the grains. As will be shown later through XEDS analysis, these feature are indeed oxides and such contrast in the HAADF would be expected since the image's contrast will scale as ~ Z^2, where Z is the atomic number. The small scale of these oxide clusters did not provide sufficient diffraction volume in the SAD pattern, but it is clear that the initial stages of oxidation were initiated in this particular nanocrystalline Fe-4Cr sample. In comparison, similar dark features are seen for the Fe-16Cr film, but are much larger in size and appear as independent grains, Figure 3(c), which would be in agreement with the PED and XEDS images in Figure 4. To further verify that the dark features are a result of the Cr content in either film, an elemental Fe nanocrystalline film annealed in an equivalent means to 800°C is shown in Figure 3(d). This HAADF feature does not show any dark

contrast nano-spheres within the grains nor any large grains with comparable dark contrast as seen in Figure 3(c). Thus, one can conclude from the microstructure, that the oxidation is facilitated by the presence of the Cr content in the nanocrystalline alloys but the morphological evolution of the oxide is composition dependent.

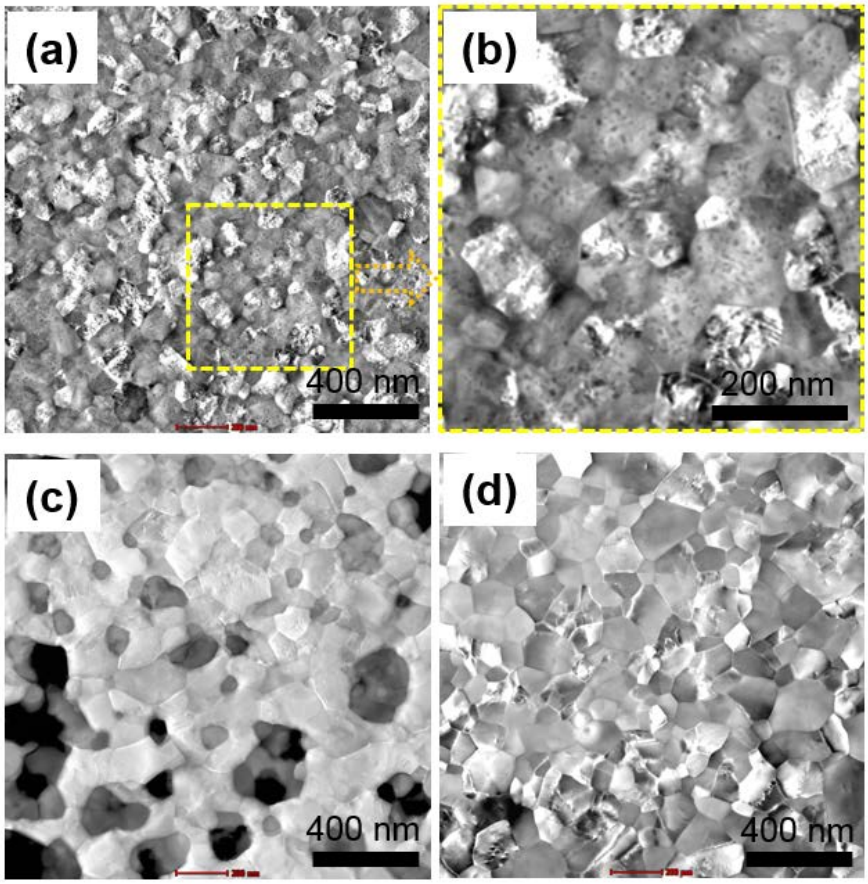

Figure 3 HAADF image of the **(a)** Fe-4Cr annealed at 800^{o}C. **(b)** is a magnified view of (a). HAADF images of the **(c)** Fe-16Cr and **(d)** Fe films annealed at 800^{o}C.

To better understand the oxygen migration that created these different oxide morphologies in each alloy, an XEDS scan was done at each sequential step of annealing with the amount of oxygen content quantified. A negligible amount of oxygen is observed in the as-deposited Fe-4Cr film and Fe-16Cr film with both films retaining this near zero value up to 600^{o}C, Figure 4(a). At 600^{o}C, a clear increase of oxygen to ~1.5 at.% is observed in the Fe-4Cr film and an increase to ~ 5 at.% was measured in the Fe-16Cr film. This uptake in oxygen is noted to occur in distinct regions within each alloy. Upon raising the temperature, the oxygen levels further increased for both films, Figure 4(a). With this increase in oxygen, it occurred in distinct regions within each

film. As noted in Figure 3, the Fe-4Cr film revealed the oxygen within the grains as small clusters (or nano-spheres) whereas the Fe-16Cr film revealed dominate oxygen content as a distinct C_2O_3 granular phases. These specific compositional distinctions can be observed in the representative XEDS maps in Figure 4(b). Based on the XEDS quantification of the oxygen content, Figure 4(a), it is clear that the Cr_2O_3 phase formed in the Fe-16Cr film, in agreement with the prior diffraction results in Figure 2. The much lower oxygen content in the Fe-4Cr film was not the Cr_2O_3 phase and would also be in agreement with the diffraction findings that did not reveal such reflections. Thus, the uptake of oxygen and the formation of Cr_2O_3 is dependent on both Cr composition, as noted in the bulk alloys [1], and temperature.

This dependence is further confirmed in tracking the Cr content in the Fe-16Cr film. Figure 4(c) is a plot of how the Cr/(Fe+Cr) ratio changes with temperature. With the onset of Cr_2O_3 precipitation in the Fe-16Cr film at 800^{o}C, the Cr content within the bulk of the alloy decreases with a corresponding increase in the precipitate composition. Thus, the oxide extracts out the Cr from the bulk of the film to grow the oxide phase. At 800^{o}C, the Cr_2O_3 phase occupied approximately 12 vol.% of the sample based on the XEDS compositional map, Figure 4(b) and PED scan in Figure 2(a; x). In contrast, the deviation of the Cr content at the clusters and within the alloy only revealed a much smaller deviation.

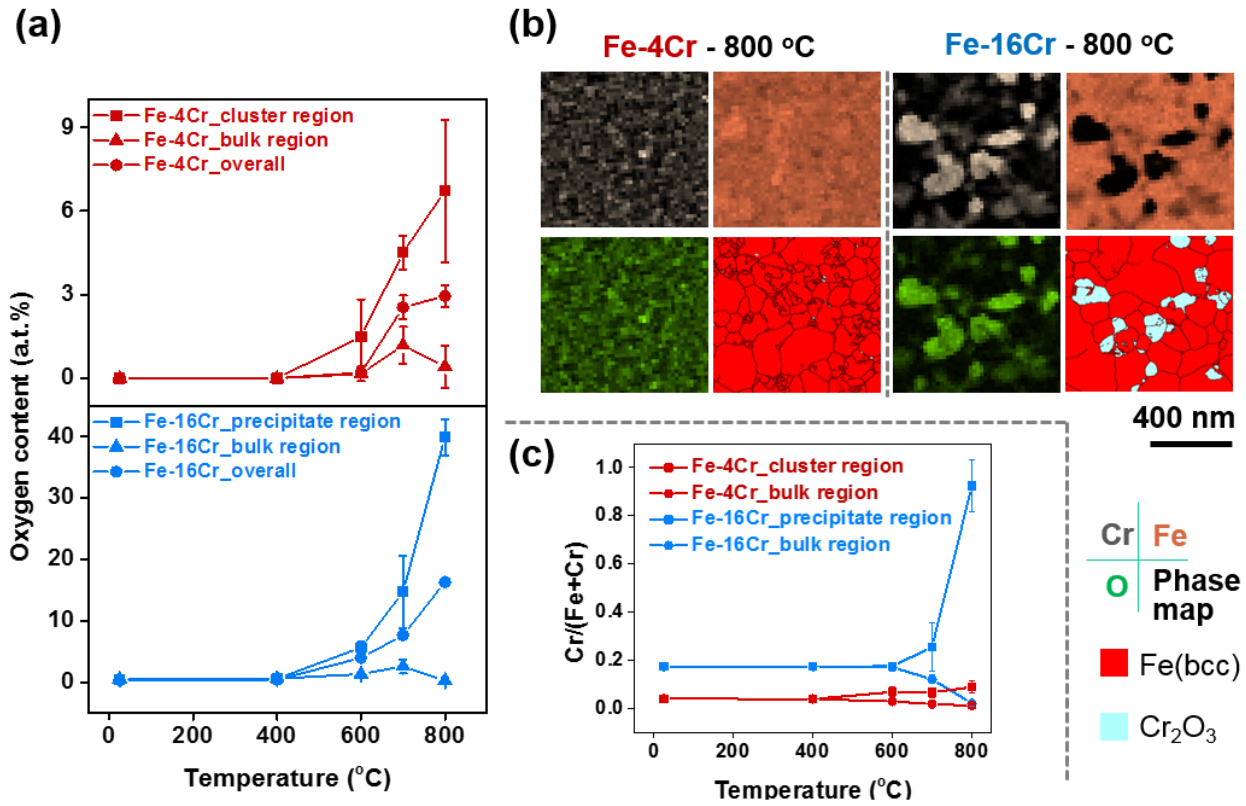

Figure 4 (a) The overall oxygen content, oxygen content of low and high Cr regions of the Fe-4Cr and Fe-16Cr films at different annealing temperature **(b)** Cr, Fe, O elemental distribution maps and phase map of the Fe-4Cr and Fe-16Cr films annealed at 800°C **(c)** the ratio of Cr/(Fe+Cr) in low and high Cr region of the Fe-4Cr and Fe-16Cr films at different annealing temperatures. bcc represents body center cubic.

The formation of the nanoscale clusters reveals an interesting thermodynamic competition that controls the morphology of the oxidation in the microstructure. The solubility of Cr in Fe, at ambient temperatures, is approximately 5 at.% and increases with temperature. Thus, the Fe-4Cr alloy is within this single phase field with no driving force for phase separation. However, the thermodynamic preference for Cr to react with oxygen has allowed it to occur within the grains itself. What is particularly interesting is that the elemental Fe film, annealed at 800°C, did not oxidize further confirming the strong preference of Cr to react with oxygen even when in solution and at very low concentrations.

Unlike the Fe-4Cr alloy, the Fe-16Cr reaction with oxygen yielded a distinct phase that had separated itself from the Fe-rich matrix microstructure. The Cr_2O_3 scale had grown into grains. Since sputtering yielded a supersaturated solid solution, upon annealing, the Fe-16Cr system was

driven to phase separate. However, as the Cr came out of solution, it reacted with the oxygen as no distinct bcc Cr reflections. The differences in the oxide morphology (clusters vs. distinct grains) is driven by this phase separation behavior. In a complimentary study to this in situ work, a 200 nm Fe-16Cr film was annealed at 700^{o}C under an equivalent vacuum condition as the TEM and a cross-sectional foil was extracted using a focus ion beam lift out method similar to that reported in [37]. Figure 5(a) reveals the XEDS cross section where one can clearly see the formation of the scale between the grains and its migration towards the surface of the film. As the Cr phase separated into the grain boundaries, it reacted with the oxygen whereupon the Cr_2O_3 consumed the grain as it grew until the Cr was depleted out of the grain. Since the Fe was less reactive to oxygen at these partial pressures and temperatures, the oxidation appeared to cease once the Cr had reacted. We can better understand this migration of the oxide along the boundaries by considering the boundary types themselves.

Using PED, the various boundary types have been identified. Figure 5(b) and (c) shows the grain boundary maps for the *in situ* 700^{o}C and 800^{o}C annealed Fe-16Cr film respectively. By comparing the ROI-A between the 700^{o}C and 800^{o}C, the Cr_2O_3 phase precipitation evolution is evident in multi-grain boundary junction, pointed to by the larger solid red arrow. At 700^{o}C, no oxides was yet present at this junction which composed three high angle gain boundaries (HAGBs, labeled #1-#3) and one Σ5 boundary (labeled #4). Also note that a low angle grain boundary (LAGB) is very near this junction (labeled #5). Upon annealing to 800^{o}C, the Cr_2O_3 precipitate became readily apparent at this former junction as well as a few other smaller oxide precipitates along one of the HAGBs (#1). The larger oxide at the junction would not be unexpected as a multi-boundary junction would be the convergence point for Cr solute from multiple sources as well as provide multiple interfaces from which the oxide could heterogeneously nucleate from and remove prior grain boundaries, albeit replacing it with an inter-phase boundary. At 800^{o}C, we can see that two of the HAGBs (#2 and #3) are now replaced by a LAGB. Upon annealing, the LAGB noted at 700^{o}C (#5) appears to have swept through the microstructure. The oxide is now bridging three distinct boundary types – LAGB (#5), a Σ5 boundary (#4), and a HAGB (#1) This convergence allows us to measure the dihedral angle at all three (different) boundary types, shown in Figure 5(d), with those values found to be 149^{o}, 116^{o}, and 97^{o} respectively. When all three boundaries are 120^{o}, the boundary energies are in geometrically stable condition; however, this is not the case. The lower 97^{o} angle for the HABG, which is the lowest among the three, suggests

that it is the preferred (or fastest) growing direction for the oxide. A HAGB can readily transport Cr solute to the precipitate because of its higher diffusivity [38, 39]. Furthermore, a LAGB and a Σ5 boundary have lower segregation of Cr solutes to it, as previously reported by the authors [39]. Collectively this would then explain why additional oxides, pointed to by the smaller dash red arrow in Figure 5(c), were only observed on the HAGB and not on the LAGB or Σ5. Using Young's equation [38],

$$\frac{\gamma_{12}}{sin\alpha_3} = \frac{\gamma_{23}}{sin\alpha_1} = \frac{\gamma_{31}}{sin\alpha_2} \qquad (1)$$

where γ is the interfacial energy, α is the contact angle of grain boundary. The relative boundary energies for the three different boundary types at each junction with the oxide were computed and tabulated in Table 1 and angle as labeled in Figure 5(e).

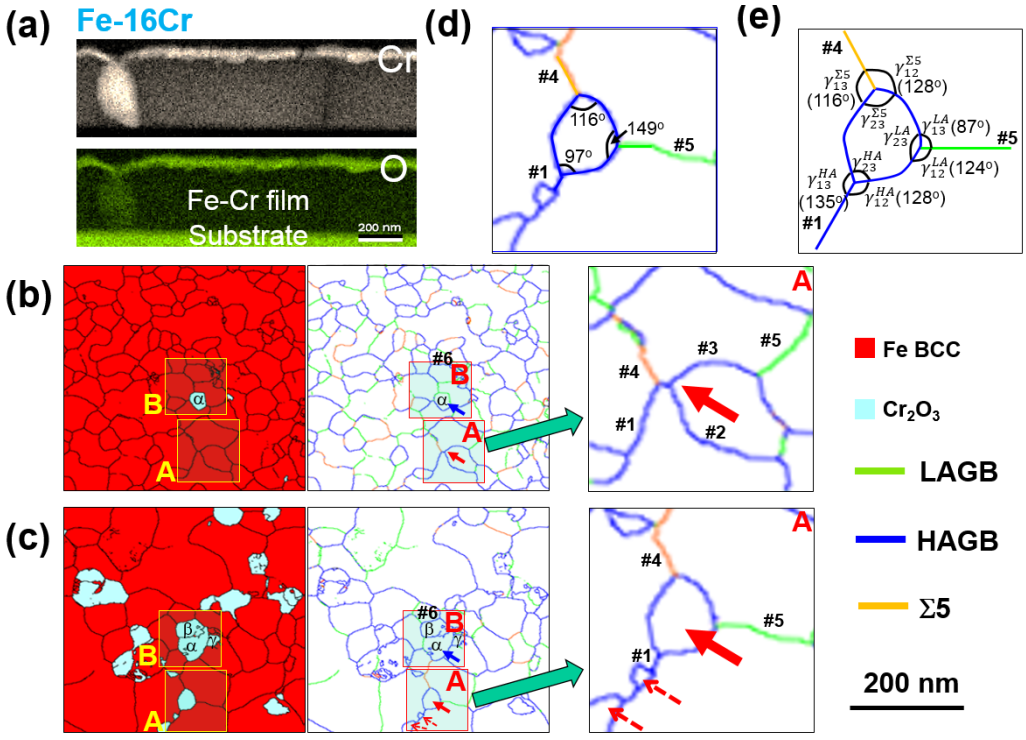

Figure 5 (a) XEDS cross section map of the Fe-16Cr film annealed at 700°C for 1 hour. Phase maps and grain boundary evolution of Fe-16Cr film after annealing at **(b)** 700°C, and **(c)** 800°C. Two cyan rectangular blocks locate ROI-A and ROI-B. **(d)** and **(e)** are the magnified grain boundary map of ROI-A of the 800°C annealed Fe-16Cr film

Table 1. The relative boundary energies for the three different boundary types at each junction with the oxide.

$\gamma_{23}^{GB} - \gamma_{12}^{GB} - \gamma_{13}^{GB}$	$\gamma_{23}^{GB}/\gamma_{12}^{GB}$	$\gamma_{23}^{GB}/\gamma_{13}^{GB}$	$\gamma_{12}^{GB}/\gamma_{13}^{GB}$
LAGB-HAGB-HAGB	0.62	0.52	0.83
HAGB-HAGB-HAGB	1.26	1.40	1.11
Σ5 - HAGB - HAGB	1.14	1.00	0.88

Looking ROI-B, Figure 5(b), we can note that a Cr_2O_3 precipitate (labeled α) was already present in a junction at 700°C, unlike ROI-A where an oxide precipitate had not yet nucleated. This α oxide was bounded between LAGBs and HAGBs. After annealing at 800°C, the size of the oxide phase increased from ~50 nm to ~100 nm and was still bounded by the same types of GBs but a part of the LAGB, which was just above the α-designated precipitate in the ROI-B, has been consumed by Cr_2O_3 growth creating a HAGB that separate itself from another Cr_2O_3 precipitate, denoted as β in ROI-B in Figure 5(c). This new Cr_2O_3 precipitate (β), as well as another Cr_2O_3 precipitate labeled γ in the same ROI-B in Figure 5(c) are all now in contact with each other as separate grains, with the contact boundaries between each being a HAGB, Figure 5(c). For these oxides to now have formed, the β and γ oxide particles must have grown from a different direction and then impinged into the α oxide particle to create a HAGB. If the α oxide particle had facilitated their nucleation, one would not expect a boundary between the oxides. Upon closer inspection of the PED scan at 700°C, the region from which the β and γ oxides originated from had HAGBs (labeled #6 in Figure 5(b)) which are is still present at 800°C, Figure 5(c). This again provides strong experimental evidence of the dominance of HAGBs in the evolution of the oxide growth.

4. Conclusion

Two nanocrystalline alloys of Fe-4Cr and Fe-16Cr were sputter deposited and formed a solid solution A2 phase. Each alloy was then in situ annealed in a TEM. At temperatures at and above 700^{o}C, both alloys revealed Cr oxidation. The oxygen source was from the low partial pressure of oxygen presence in the TEM column. Though both alloys oxidized, the morphology of the oxide was different. For the Fe-4Cr, nanoscale oxide clusters were characterized to be within the Fe matrix grains whereas large, distinct granular Cr_2O_3 phases present in the Fe-16Cr alloy. Neither oxide produced a continuous passive layer for the Fe-rich matrix. Though Fe oxide is also a favorable reaction, at these temperatures and partial pressures of oxygen, no Fe oxides were not observed. This demonstrates the very strong oxidation tendencies of Cr, even in environments that are not necessary oxygen-rich.

The formation of the oxide clusters in Fe-4Cr was contributed to Cr being thermodynamically favorable in solution with Fe. However, for Fe-16Cr, the solid solution was supersaturated and upon annealing, the Cr would be driven to phase separate from Fe. However, upon separating, the Cr reacted with the low partial pressure of oxygen in the column and formed Cr_2O_3. This phase separation and oxidation reaction occurred at the grain boundaries within the microstructure. With the higher Cr content, this alloy was able to continue to provide sufficient Cr content for the scale in the boundary to grow and become distinct grains within the microstructure. Furthermore, through the use of in situ analysis, coupled with PED for grain boundary character quantification, the evolution of the oxide from these boundaries was tracked and measured. The oxides most readily grow from HAGBs. The dominance of the HAGB was noted for a particular oxide precipitate that was connected to a HABG, a LAGB, and a $\Sigma 5$. Upon annealing, the oxide demonstrated preference for growth along the HAGB evident by a lower dihedral angle and the additional precipitation of oxides on the same boundary. This has been contributed to the higher Cr diffusivity of this boundary compared to the other types. In this case, the lower oxygen content within the TEM column provided a controlled oxidation response in the material allowing us to observe these initial stages of reactions and nucleation. Such reactions should be expected to occur even if the diffraction does not indicate it, as evident by our Fe-4Cr alloy which formed clusters but no clear diffraction change in the A2 solid solution.

ACKNOWLEDGMENT

The authors gratefully recognize support from the Army Research Office, grant W911NF1310436, as well as the University of Alabama's Central Analytical Facility. The SDD for the EDS and DENS heating stage was purchased under the DURIP award W911NF1510405.

REFERENCES

[1] KH Lo, CH Shek, JKL Lai (2009) Materials Science & Engineering R-Reports 65: 39. Doi:10.1016/j.mser.2009.03.001
[2] RL Klueh, AT Nelson (2007) Journal of Nuclear Materials 371: 37. Doi:10.1016/j.jnucmat.2007.05.005
[3] EA Little (1979) Journal of Nuclear Materials 87: 11. Doi:https://doi.org/10.1016/0022-3115(79)90122-3
[4] RA Lula, JG Parr (1986) Stainless steel. American Society for Metals,
[5] RK Gupta, N Birbilis (2015) Corrosion Science 92: 1. Doi:10.1016/j.corsci.2014.11.041
[6] T Horita, Y Xiong, H Kishimoto, K Yamaji, N Sakai, H Yokokawa (2004) Journal of Power Sources 131: 293. Doi:https://doi.org/10.1016/j.jpowsour.2003.10.017
[7] D Terentyev, P Olsson (2008).
[8] M Ziętala, T Durejko, M Polański, et al. (2016) Materials Science and Engineering: A 677: 1. Doi:https://doi.org/10.1016/j.msea.2016.09.028
[9] K Sugimoto, S Matsuda (1980) Materials Science and Engineering 42: 181. Doi:10.1016/0025-5416(80)90027-0
[10] B Pujilaksono, T Jonsson, H Heidari, M Halvarsson, JE Svensson, LG Johansson (2011) Oxid Met 75: 183. Doi:10.1007/s11085-010-9229-z
[11] HJ Grabke (2000) Surface and Interface Analysis 30: 112. Doi:Doi 10.1002/1096-9918(200008)30:1
[12] A Ponomareva, E Isaev, N Skorodumova, Y Vekilov, I Abrikosov (2007) Physical Review B 75: 245406. Doi:10.1103/PhysRevB.75.245406
[13] M Ropo, K Kokko, M Punkkinen, et al. (2007) Physical Review B 76: 220401(R). Doi:10.1103/PhysRevB.76.220401
[14] P Alnegren (2012) Institutionen för kemi- och bioteknikChalmers tekniska högskola, Göteborg
[15] VB Trindade, U Krupp, PEG Wagenhuber, HJ Christ (2005) Materials and Corrosion 56: 785. Doi:10.1002/maco.200503879
[16] RA Golden, EJ Opila (2018) Journal of Materials Science 53: 3981. Doi:10.1007/s10853-017-1823-x
[17] N Das, T Shoji, Y Takeda (2010) Corrosion Science 52: 2349. Doi:10.1016/j.corsci.2010.04.006
[18] S Lozano-Perez, D Saxey, T Yamada, T Terachi (2010) Scripta Materialia 62: 855. Doi:10.1016/j.scriptamat.2010.02.021
[19] M Punkkinen, K Kokko, H Levamaki, et al. (2013) Journal of Physics-Condensed Matter 25: 495501. Doi:10.1088/0953-8984/25/49/495501
[20] COA Olsson, D Landolt (2003) Electrochimica Acta 48: 1093. Doi:10.1016/S0013-4686(02)00841-1
[21] CR Xue, T Narushima, Y Ishida, T Tokunaga, T Yonezawa (2014) Acs Appl Mater Inter 6: 19924. Doi:10.1021/am505333v
[22] GH Cui, DZ Wu, SL Qi, S Jin, ZP Wu, RG Jin (2011) Acs Appl Mater Inter 3: 789. Doi:10.1021/am1011468
[23] CM Wang, DK Schreiber, MJ Olszta, DR Baer, SM Bruemmer (2015) Acs Appl Mater Inter 7: 17272. Doi:10.1021/acsami.5b04341

[24] DE Eakins, DF Bahr, MG Norton (2004) Journal of Materials Science 39: 165. Doi:DOI 10.1023/B:JMSC.0000007741.97288.bd
[25] BA Cook, XZ Wei, JL Harringa, MJ Kramer (2007) Journal of Materials Science 42: 7643. Doi:10.1007/s10853-007-1898-x
[26] ARS Gautam, JM Howe (2009) Journal of Materials Science 44: 601. Doi:10.1007/s10853-008-3080-5
[27] MY Zheng, WC Zhang, K Wu, CK Yao (2003) Journal of Materials Science 38: 2647. Doi:Doi 10.1023/A:1024486619379
[28] R Banerjee, PA Crozier (2012) Journal of Physical Chemistry C 116: 11486. Doi:10.1021/jp2073446
[29] K Unocic, D Shin, R Unocic, L Allard (2017) Oxid Met 88: 495. Doi:10.1007/s11085-016-9676-2
[30] Y Sasanuma, M Uchida, K Okada, K Yamamoto, Y Kitano, A Ishitani (1991) Thin Solid Films 203: 113. Doi:http://dx.doi.org/10.1016/0040-6090(91)90522-Y
[31]
[32] J Brons, G Thompson (2014) Jom 66: 165. Doi:10.1007/s11837-013-0799-5
[33] JG Brons, GB Thompson (2013) JOM 66: 165. Doi:10.1007/s11837-013-0799-5
[34] P Moeck, S Rouvimov, EF Rauch, et al. (2011) Crystal Research and Technology 46: 589. Doi:10.1002/crat.201000676
[35] EF Rauch, J Portillo, S Nicolopoulos, D Bultreys, S Rouvimov, P Moeck (2010) Zeitschrift für Kristallographie 225: 103. Doi:10.1524/zkri.2010.1205
[36] AH Hill, A Harrison, C Dickinson, WZ Zhou, W Kockelmann (2010) Micropor Mesopor Mat 130: 280. Doi:10.1016/j.micromeso.2009.11.021
[37] LA Giannuzzi, FA Stevie (1999) Micron 30: 197. Doi:https://doi.org/10.1016/S0968-4328(99)00005-0
[38] G Gottstein (2004) Physical Foundations of Materials Science. Springer Berlin Heidelberg,
[39] X Zhou, X-x Yu, T Kaub, RL Martens, GB Thompson (2016) Scientific Reports 6: 34642. Doi:10.1038/srep34642

Cross-correlative Precession Electron Diffraction:
A study on solute-grain boundary segregation

Xuyang Zhou[1], Xiao-xiang Yu[1*], Tyler Kaub[1], Richard Martens[2], and Gregory B. Thompson[1]

University of Alabama
[1] Metallurgical And Materials Engineering
[2] Central Analytical Facility
Tuscaloosa, Alabama, USA
**now at Northwestern University*

This work was funded with support from the Army Research Office, ARO-W911NF-13-1-0436 and W911NF1510405 (DURIP)

Solute-grain boundary interactions

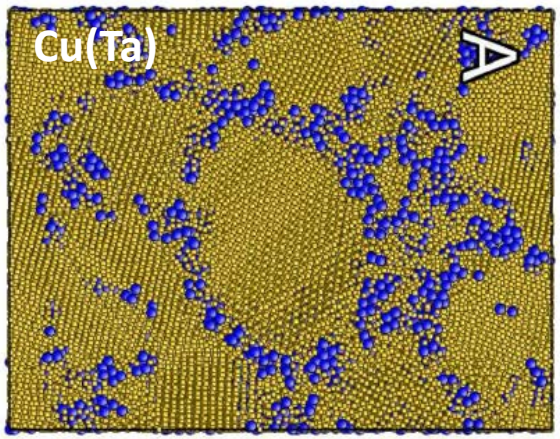

T. Frolov, K.A Darling, L.J. Kecskes, Y.Mishin. Stabilization and strengthening of nanocrystalline copper by alloying with Ta. ***Acta Materialia 60 (2012) 2158-2168.***

Examples:

- Solute segregation stabilizing nanocrystalline grains against thermally driven grain growth
- Grain size influences intrinsic stress states in thin films

$$\Delta G = \frac{2\gamma V_m}{r}$$

ΔG is the free energy change created by the pressure difference across a curved boundary, γ is the grain boundary energy per unit area, V_m is the molar volume, and r is the grain boundary radius of curvature

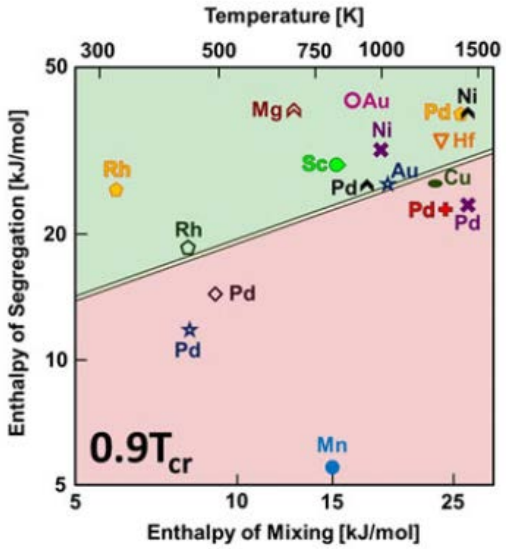

H. A. Murdoch, C. A. Schuh. Estimation of grain boundary segregation enthalpy and its role in stable nanocrystalline alloy design. ***Journal of Materials Research 28 (2013) 2154-2163.***

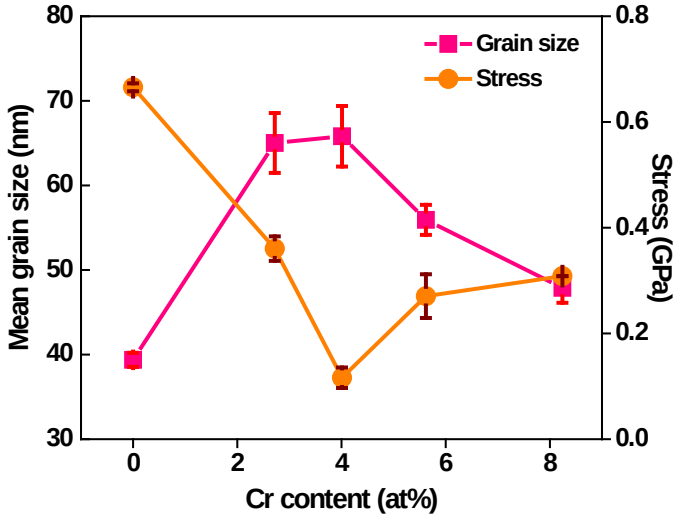

X. Zhou, T. Kaub, R. Martens, and G.B. Thompson. Influence of Fe(Cr) miscibility on thin film grain size and stress. ***Thin Solid Films 612 (2016) 29-35***

.

CAPSTONE ENGINEERING

Grain Boundary Structure & Energy

$$d\gamma = -\Gamma d\mu_{dop}$$

The grain boundary energy, γ, can be reduced by the preferential segregation of a solute over the grain boundary area, Γ, and μ_{dop} is the chemical potential of the dopant

Grain boundaries are diverse in their energy, structure, and mobility

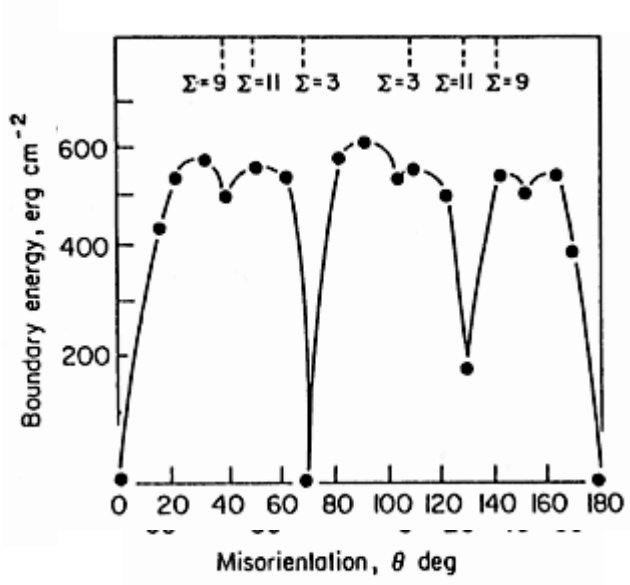

http://www.bing.com/images/search?q=concident+site+lattices+energies&view=detailv2&&id=6FE00B5BFE42DB142F14022C33DC3B6A737084F0&selectedIndex=0&ccid=1Yh1GLU7&simid=608012120133861912&thid=OIP.Md5887518b53ba78a5dbeb292d64d8921o0&ajaxhist=0

CSL or special character grain boundaries

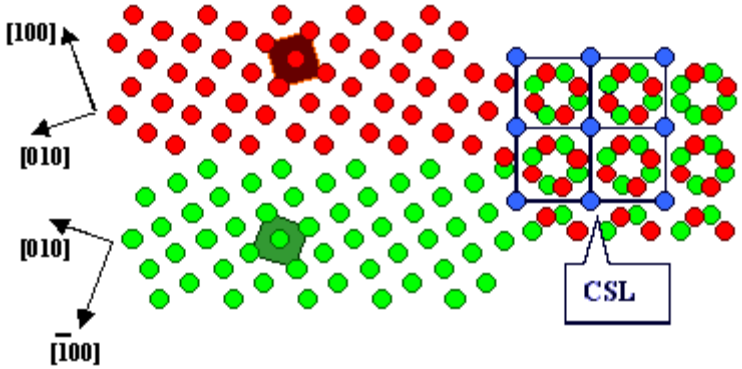

http://www.bing.com/images/search?q=concident+site+lattices+energies&view=detailv2&&id=6FE00B5BFE42DB142F14E4333C5083F589F2D15D&selectedIndex=1&ccid=7n4lN%2fZq&simid=608017398656994819&thid=OIP.Mee7e2537f66a3d9911d5b19927a1e5c2o0&ajaxhist=0

Quantifying Solutes in GBs – Cross correlation microscopy

- Requires **high spatial resolution** and **high chemical sensitivity**

Precession Electron Diffraction (PED)

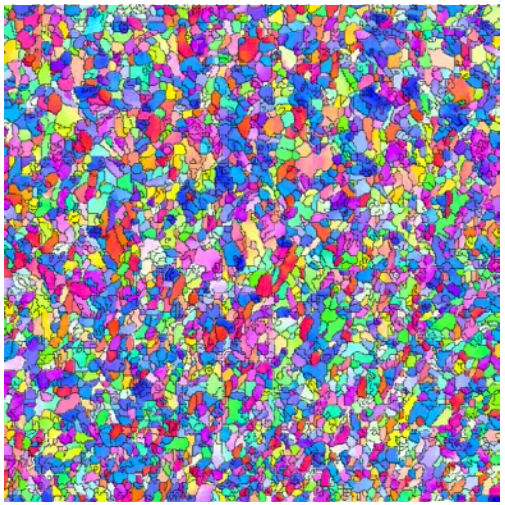

400 nm

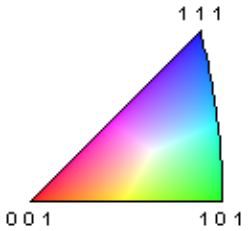

Atom Probe Tomography (APT)

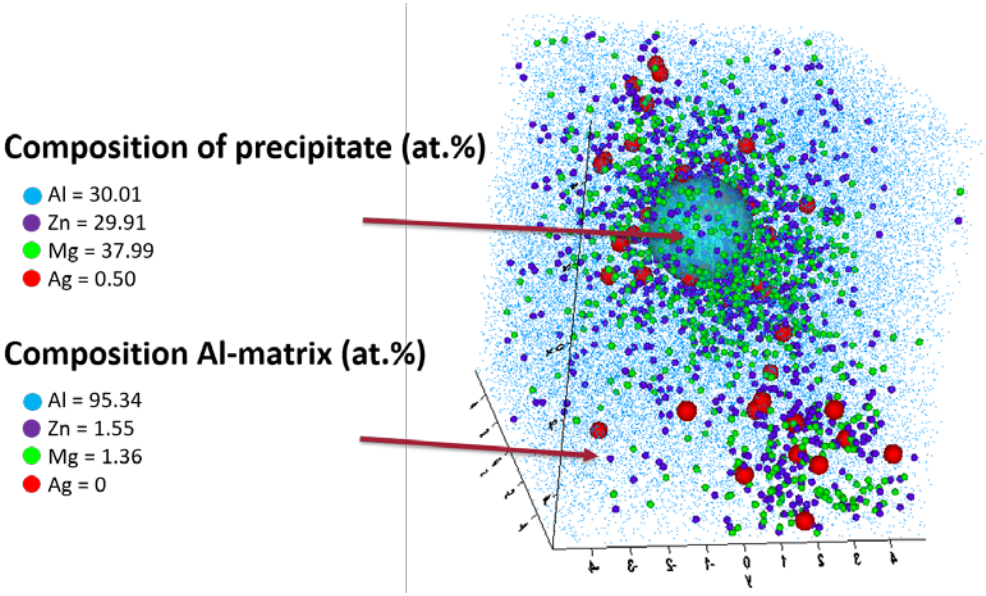

Atom Probe Tomography

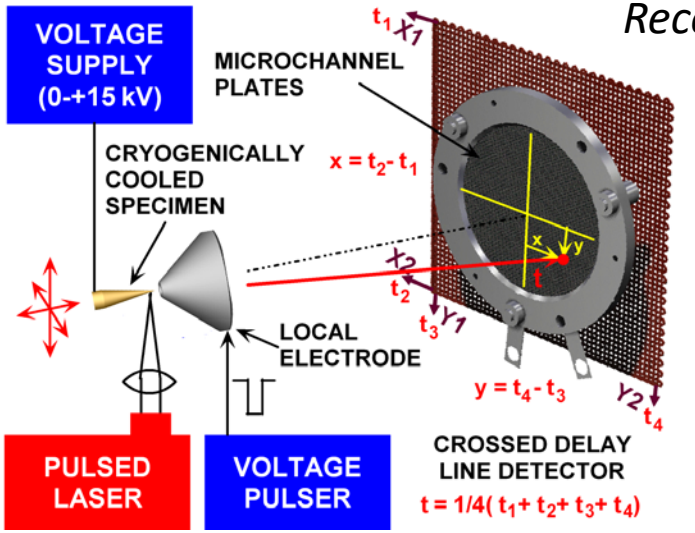

Image courtesy of M. Miller, ORNL

Reconstructed volume

Assumes a constant field of evaporation

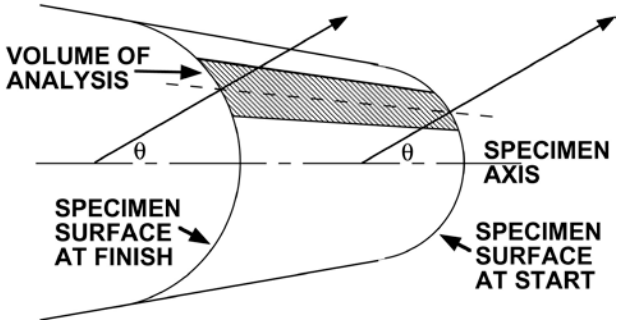

$$r_t = \frac{V}{k_f F}$$

r_t – radius of curvature
k_f – geometric field factor
V – apex voltage
F – evaporation field

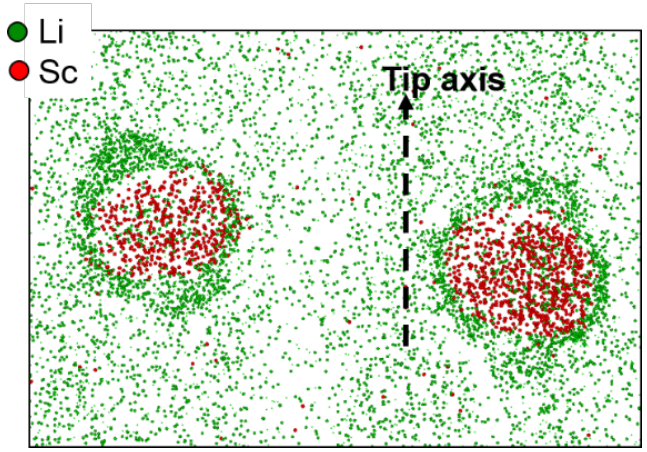

V. Radmilovic, A. Tolley, E.A.Marquis et al., Scripta Mater. 58 (2008) 529

Consequence, loss of perfect lattice rectification

Precession-Electron-Diffraction (PED) for Orientation Mapping

#1: Precess the beam

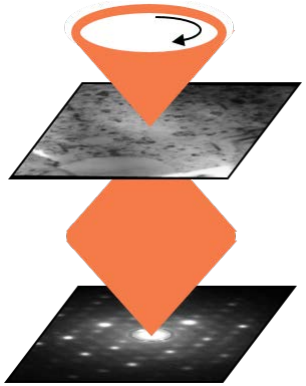

#2: Raster

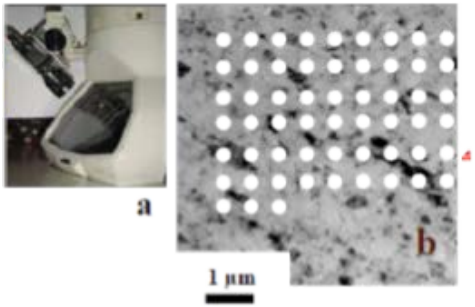

#3: Compare experimental DP to simulated orientations for matching

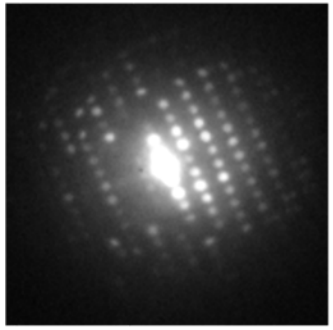

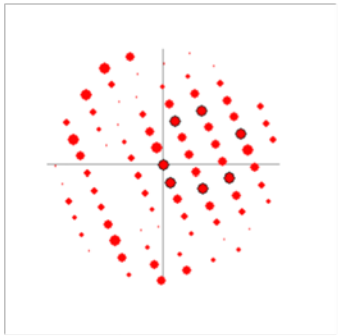

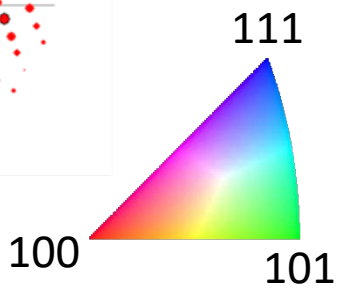

#4: Out put phase and orientation maps

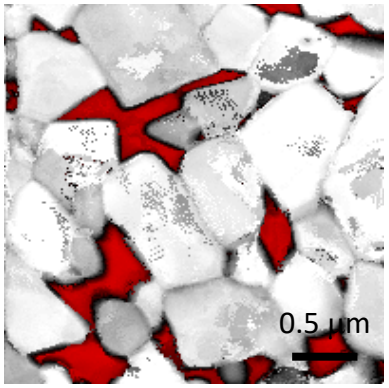

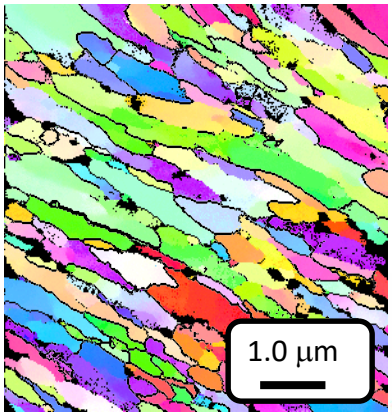

Images courtesy of E. Rauch

Case study: Fe(Cr)

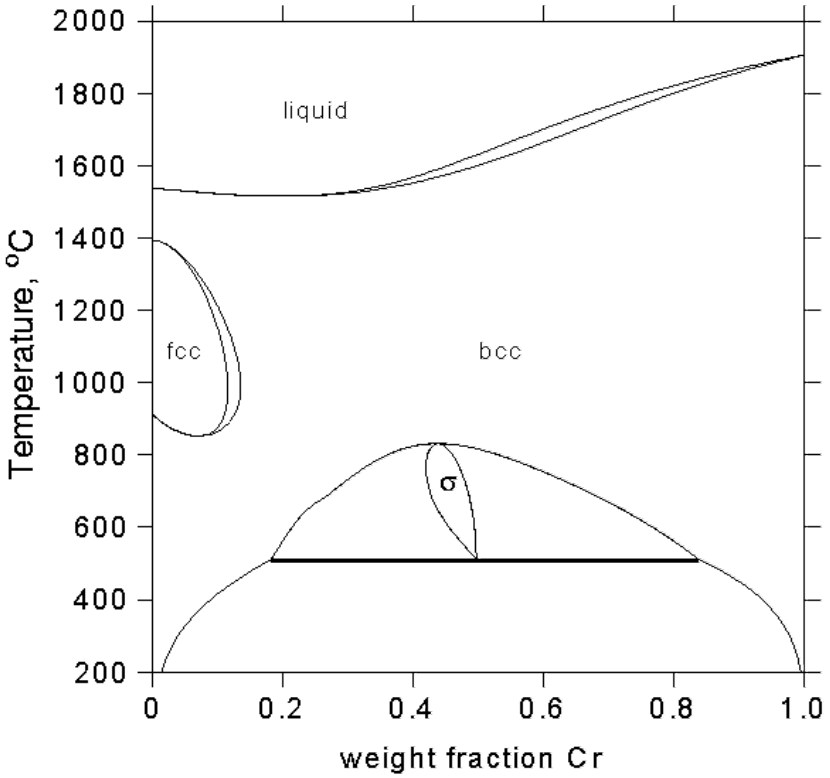

- Both BCC structures
- Exhibits a miscibility gap
- Technically important as basic building block species for stainless steel

- How does segregation regulate nanocrystalline grain behavior in Fe-Cr?
- How does segregation scale with grain boundary types?

Sputter-deposited Fe(Cr) nanocrystalline films

- <10^{-8} Torr
- ~2 mTorr UHP Ar
- Co-deposition from Fe and Cr targets
- RT deposition (and elevated temperature depositions when indicated)
- 30-300 nm thicknesses

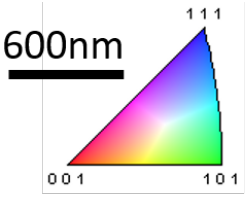

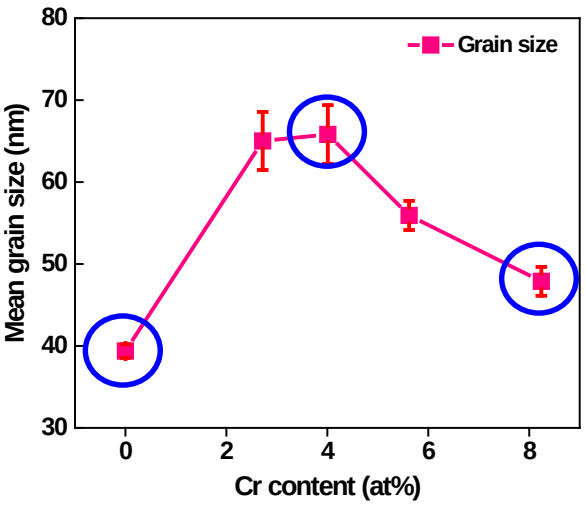

Cr solute changes the Fe grain size

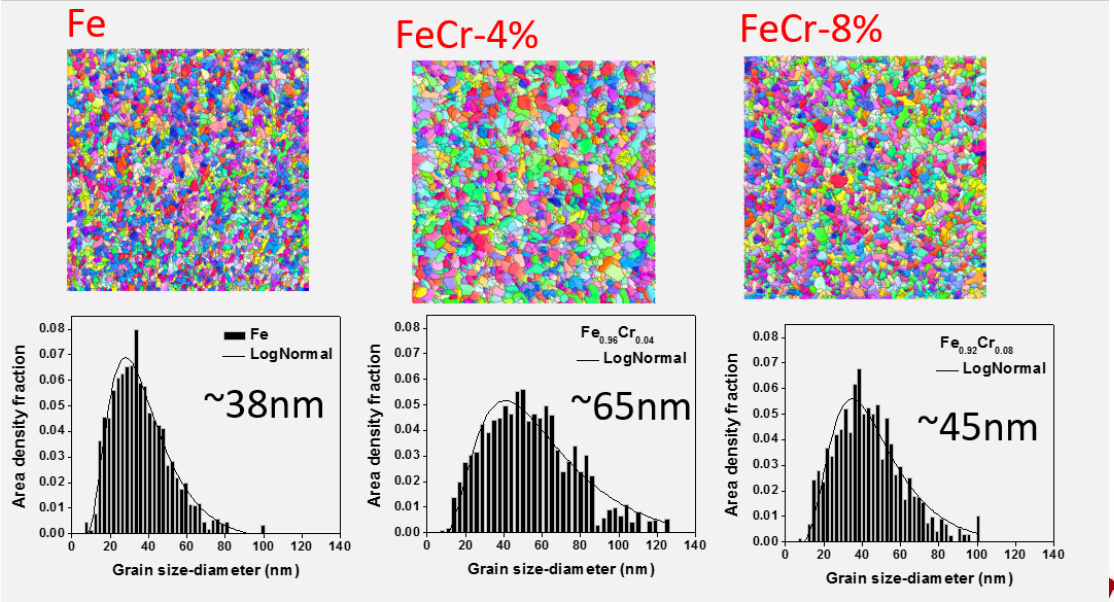

*X. Zhou, et al. Thin Solid Films **612** (2016) 29-35.*

Initial APT analysis

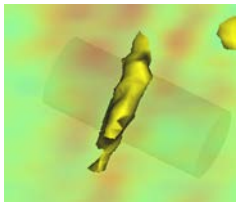

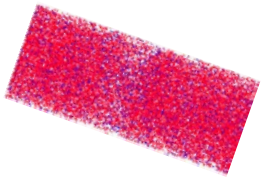

Fe
Cr

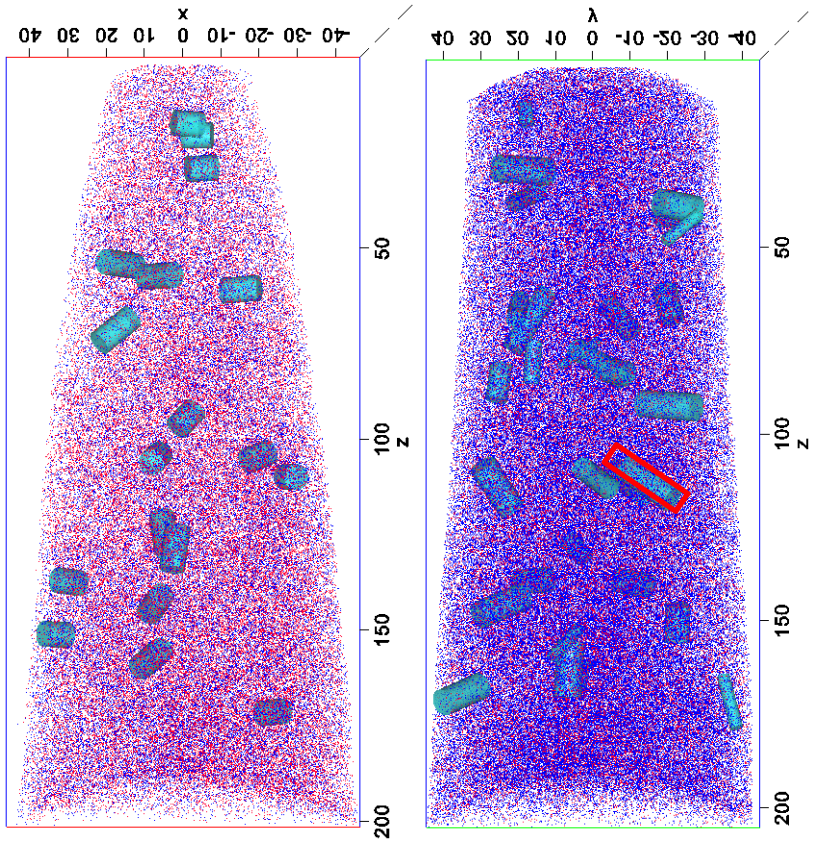

FeCr-3%

FeCr-8%

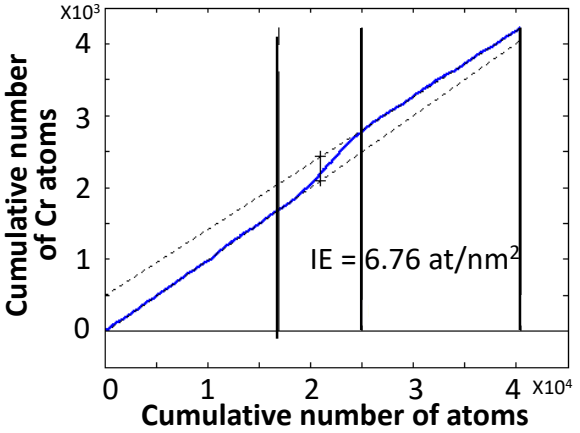

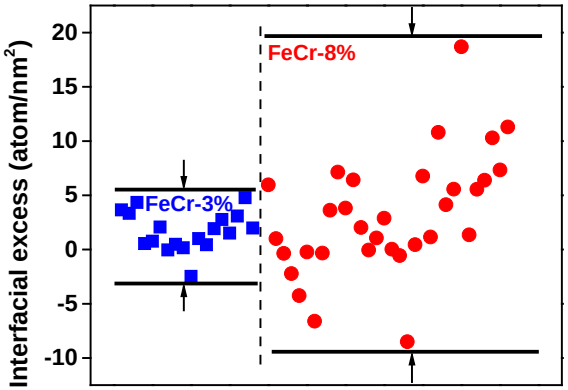

- The Interfacial Excess (IE) values of different GBs are quite different
- The range of IE value of FeCr-8% is larger than FeCr-3%.

*X. Zhou, et al. Thin Solid Films **612** (2016) 29-35.*

Phase separation → grain refinement growth

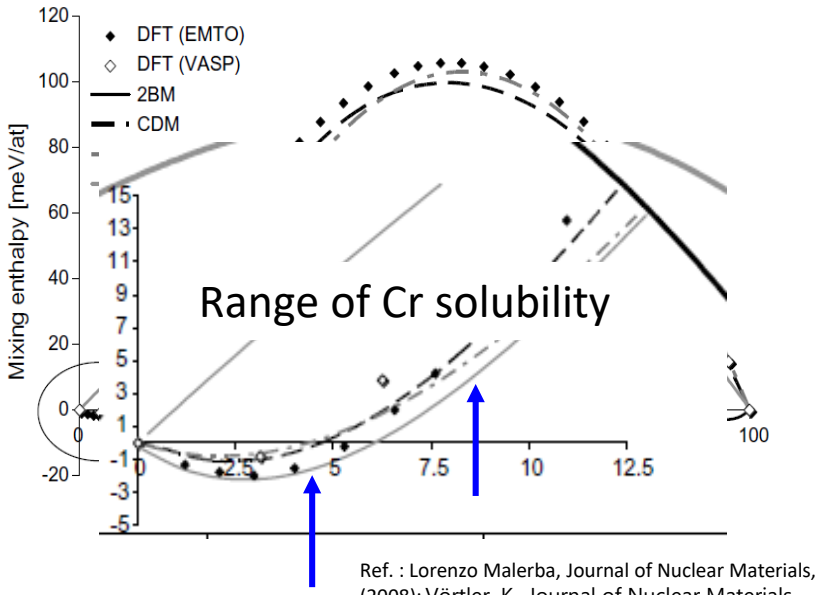

Ref. : Lorenzo Malerba, Journal of Nuclear Materials, (2008); Vörtler, K., Journal of Nuclear Materials, (2008)

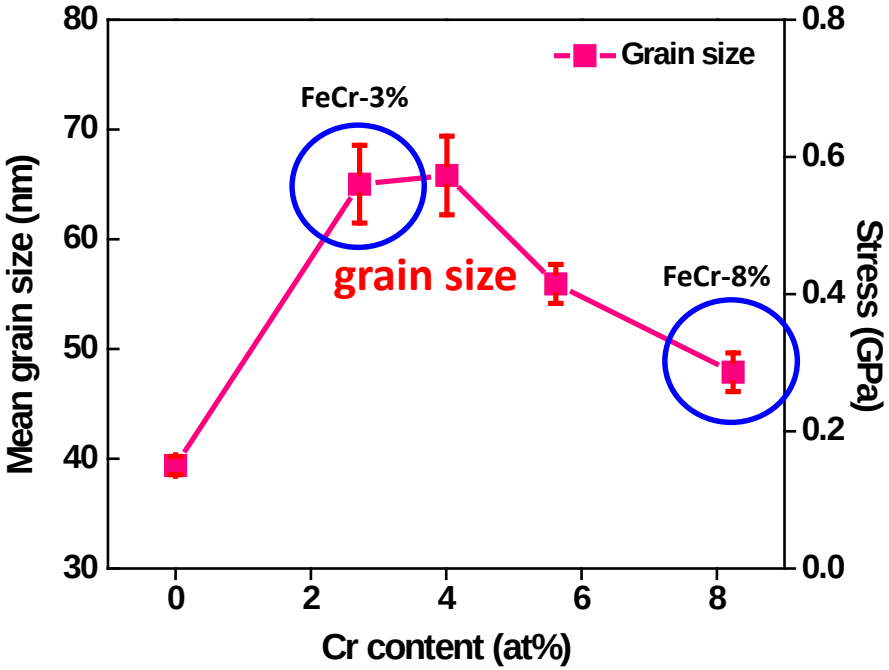

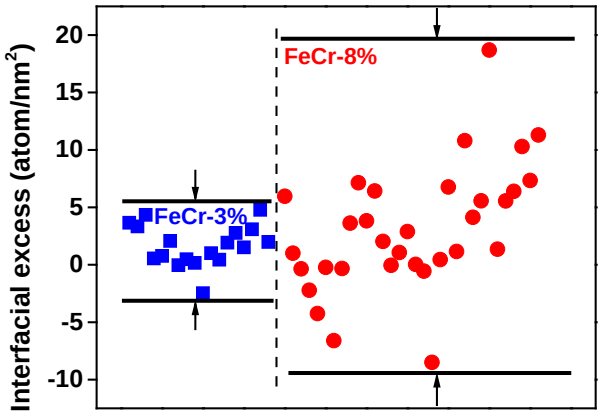

Cr content in the grain boundaries acts as a grain refiner.

*X. Zhou, et al. Thin Solid Films **612** (2016) 29-35.*

What is contributing to the interfacial excess spread?

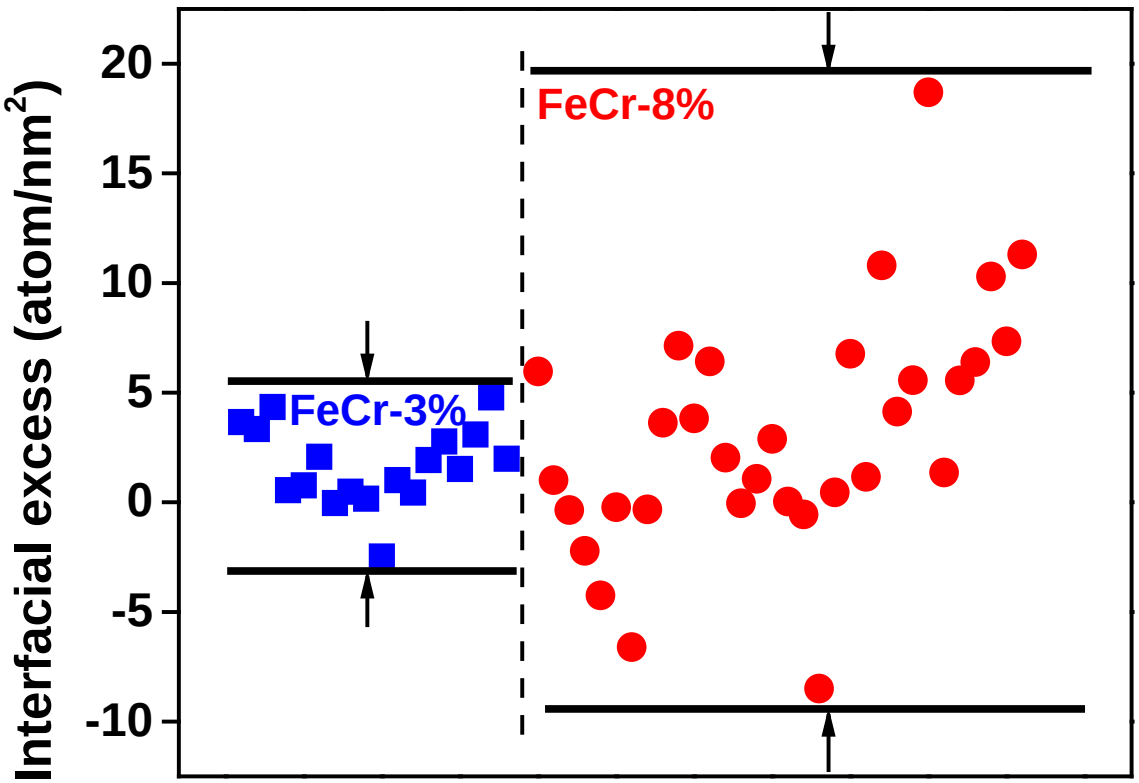

Correlative PED & APT – sample preparation

Cut the edge by Ga⁺ ➡ **Lift-out a wedge** ➡ **Mount the wedge on Si half grid**

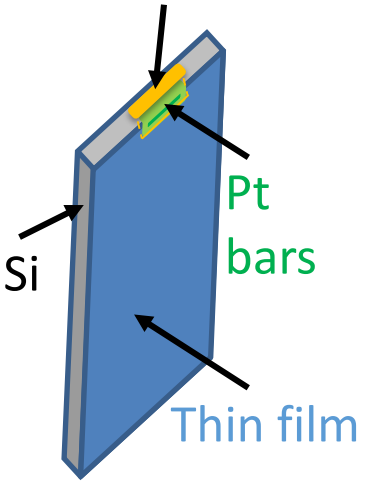

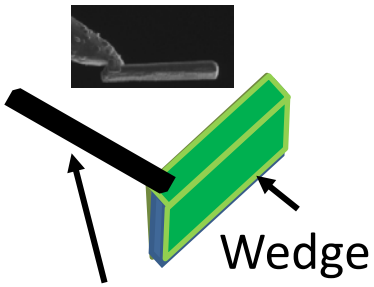

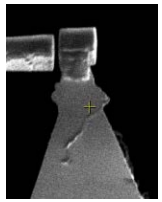

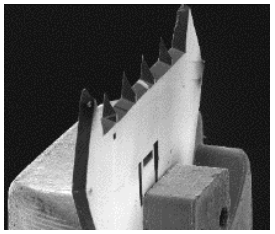

Sharpen tips by Ga⁺

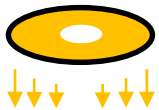

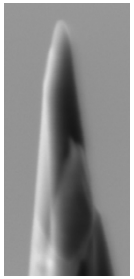

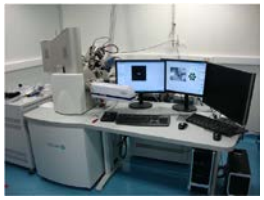

Image tips in TEM

Evaporate tips in LEAP

Zhou, X. et al. Sci. Rep. ***6****, 34642; doi: 10.1038/srep34642 (2016)*

Correlative TEM & APT – Segregation to specific GBs

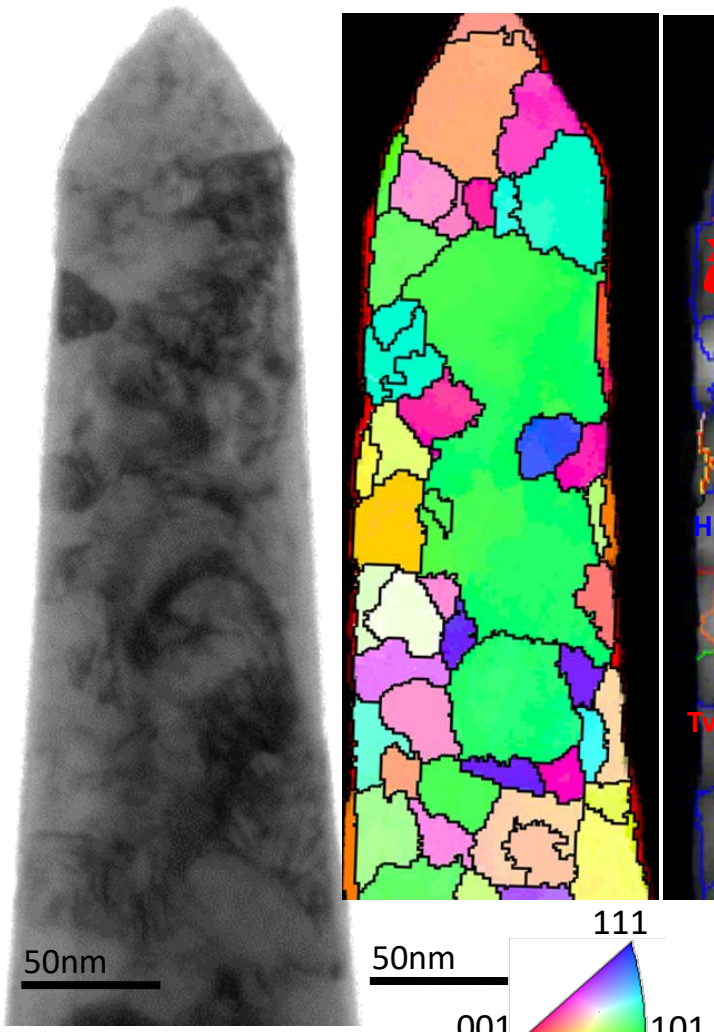

Zhou, X. et al. Sci. Rep. ***6****, 34642; doi: 10.1038/srep34642 (2016)*

Experimental Results of Cr Segregation to specific GBs

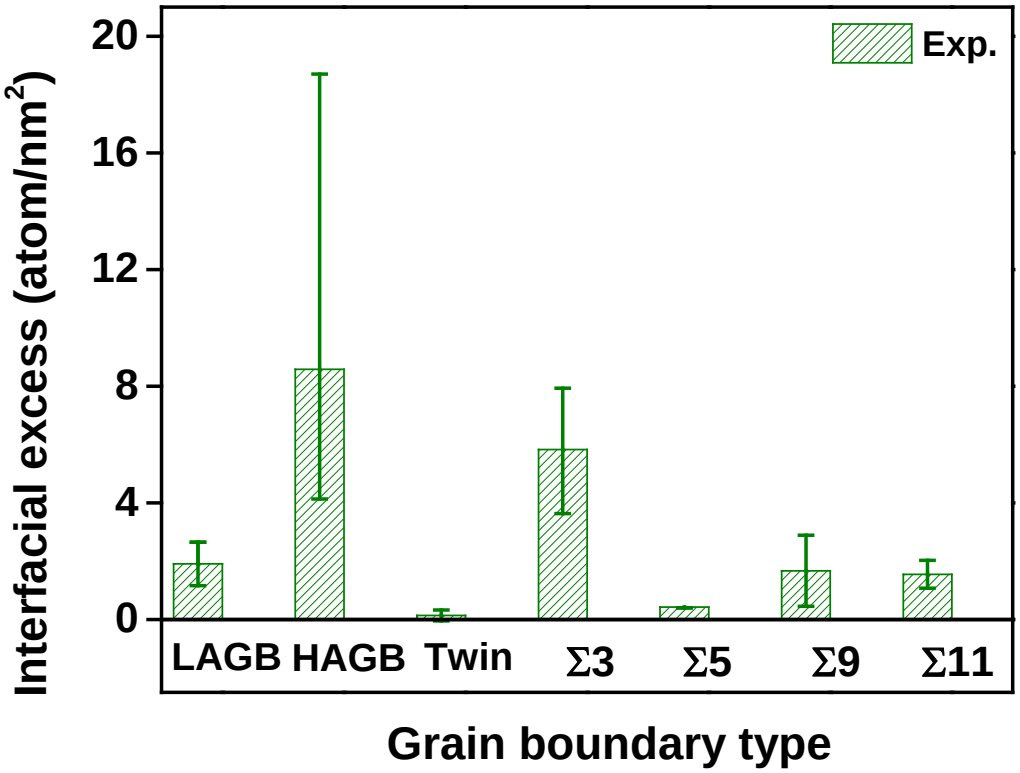

- Cr segregation is strongly related with GB types
- HAGBs appear to have both the largest Cr segregation and largest range
- **What is contributing to the range of values for the same mis-orientation?**

*Zhou, X. et al. Sci. Rep. **6**, 34642; doi: 10.1038/srep34642 (2016)*

Need to fully quantify the grain boundary character

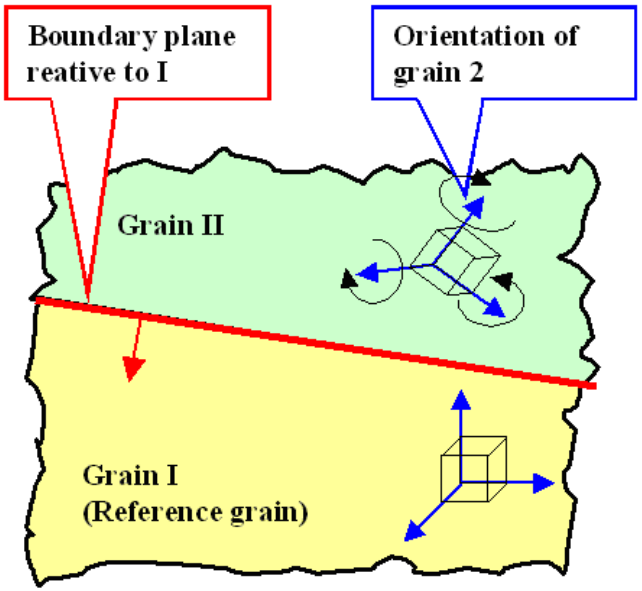

- Defining a grain boundary needs 5 parameters:
  - 3 for orientations related to adjacent grains
  - 2 for orientation GB plane inclination

http://www.tf.uni-kiel.de/matwis/amat/iss/kap_5/advanced/a5_3_1.html

GB Inclination:

Proof 1: Cross-section image

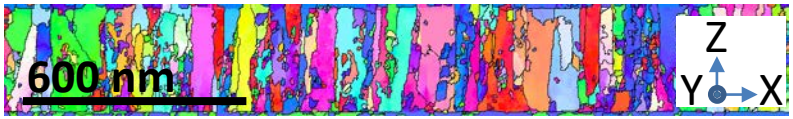

Proof 2: Measure the GB inclination

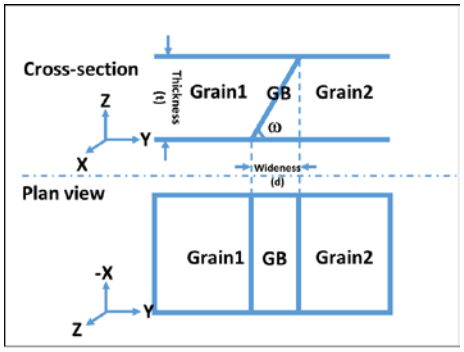

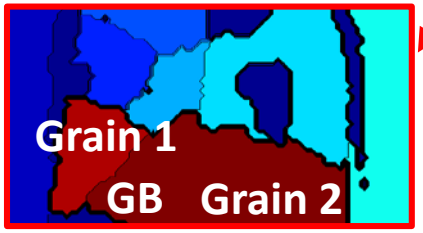

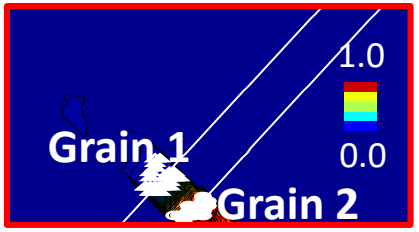

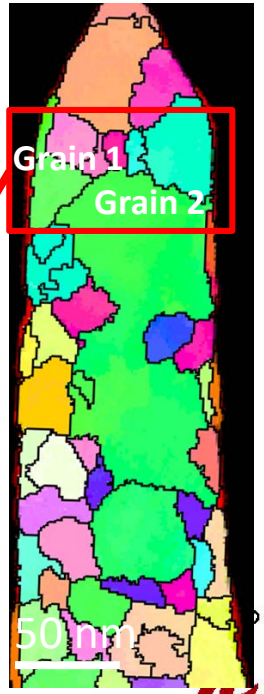

*Zhou, X. et al. Sci. Rep. **6**, 34642; doi: 10.1038/srep34642 (2016)*

Kiss and Labar, Micro. Microanal. 2016

Quantifying the GB inclination

- Determine the GB plane projection (PED and/or planar assumption)
- Rotate the two lattices in each grain until a common (reference) plane is found
- The angle between the GB projection plane to the shared reference lattice plane defines the GB inclination

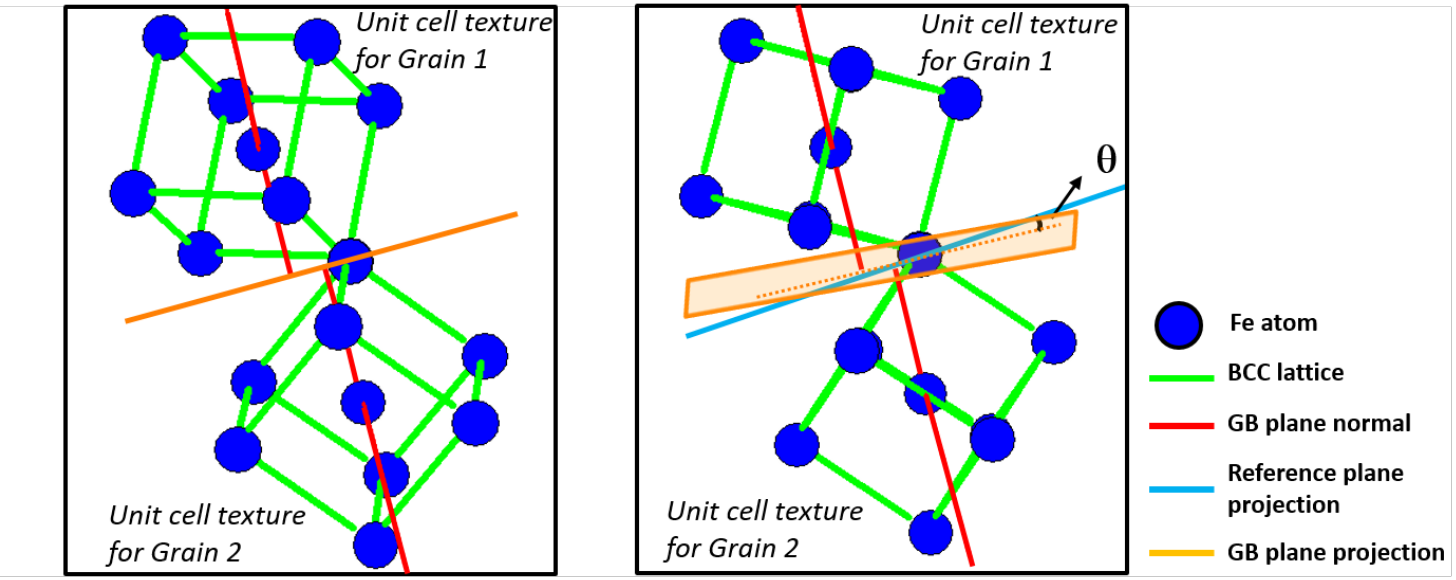

Zhou, X. et al. Sci. Rep. **6**, 34642; doi: 10.1038/srep34642 (2016)

Cr Segregation dependency on GB inclination

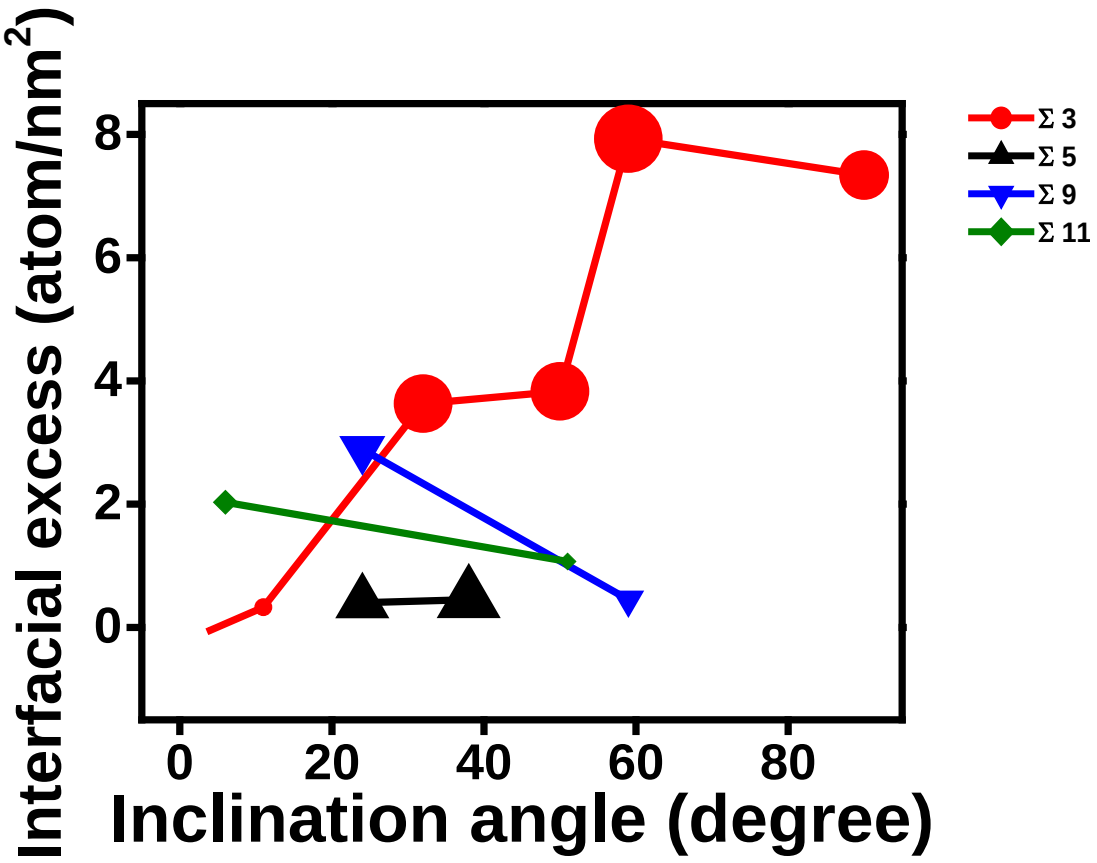

GB Simulation: *Hybrid Molecular Dynamics/Monte Carlo Calculation*

- Using the fully defined GB, equivalent GBs were simulated to determine solute behavior within the GBs
- A hybrid MD/MC simulation* was conducted in LAMMPS
- The segregated Fe(Cr) structure was obtained at a temperature of 300 K by using the Fe-Cr binary concentration dependent embedded atom model potential.

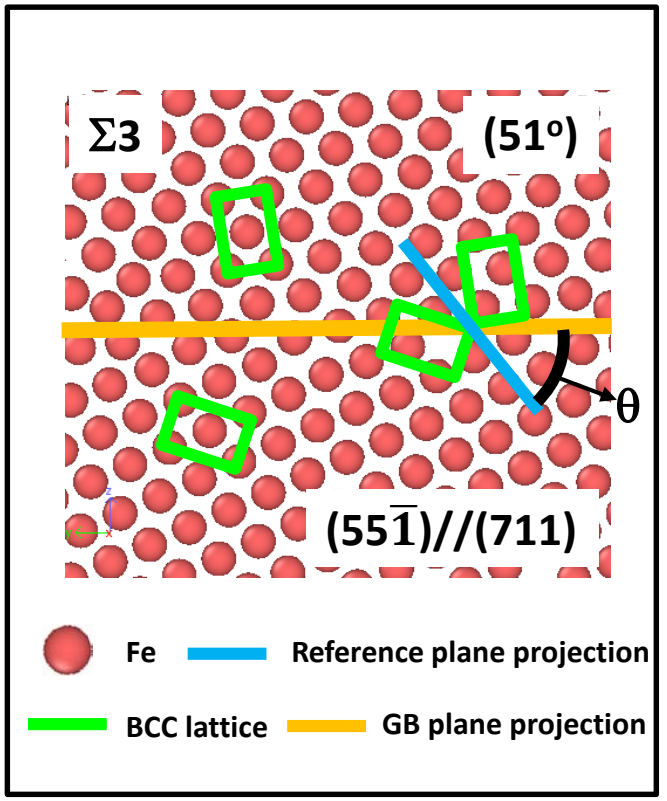

**Babak Sadigh, PRB, 2012*)

https://staff.aist.go.jp/h.ogawa/GBstudio/gbs3/GBs_PJ.html

Comparisons between experimental & simulated results

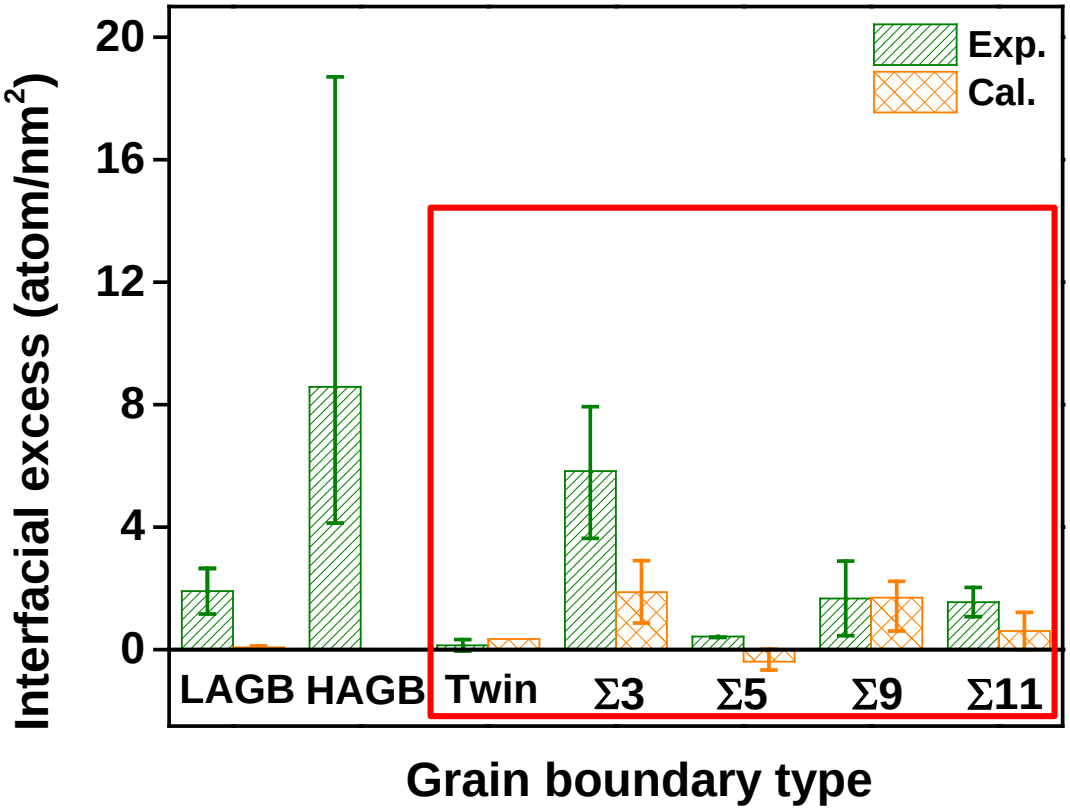

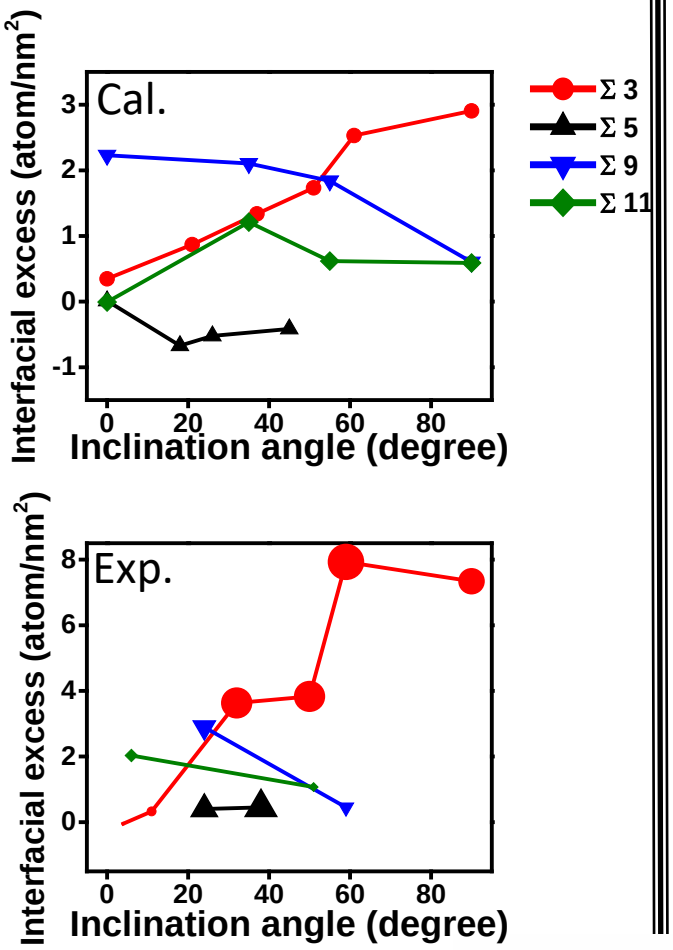

- Experimental IE values are similar to predicted values.

Zhou, X. et al. Sci. Rep. ***6****, 34642; doi: 10.1038/srep34642 (2016)*

Comparisons between experimental & simulated results

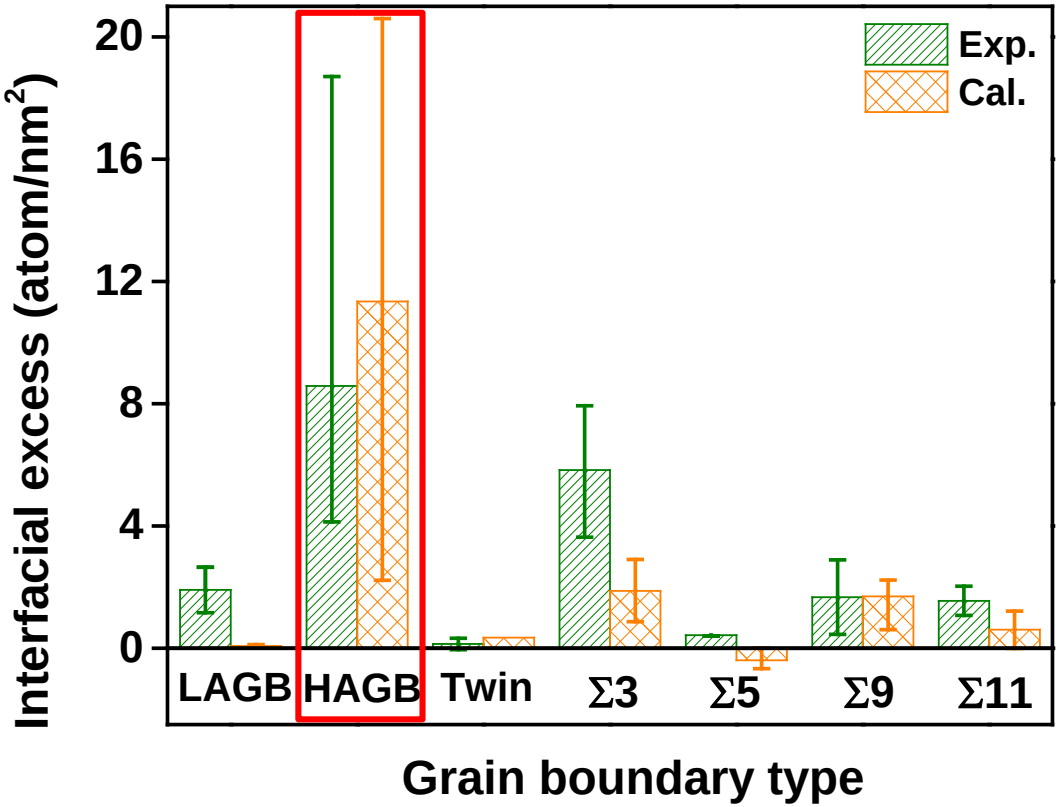

Clustering Analysis

Exp.

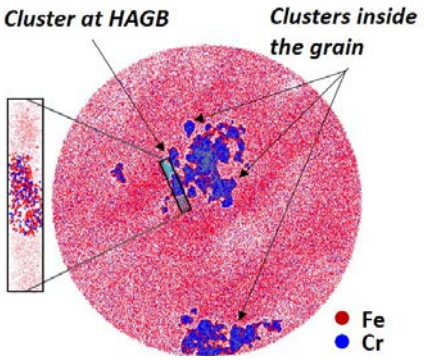

Cal.*

Poly-Crystal

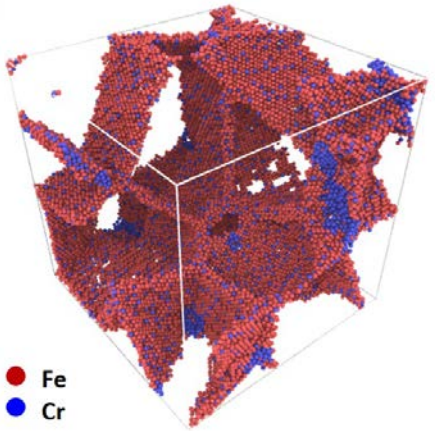

- Experimental IE values are similar to predicted values.
- Clusters form at high angle grain boundaries.

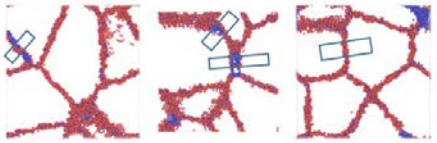

Comparison of GB behavior: specific types

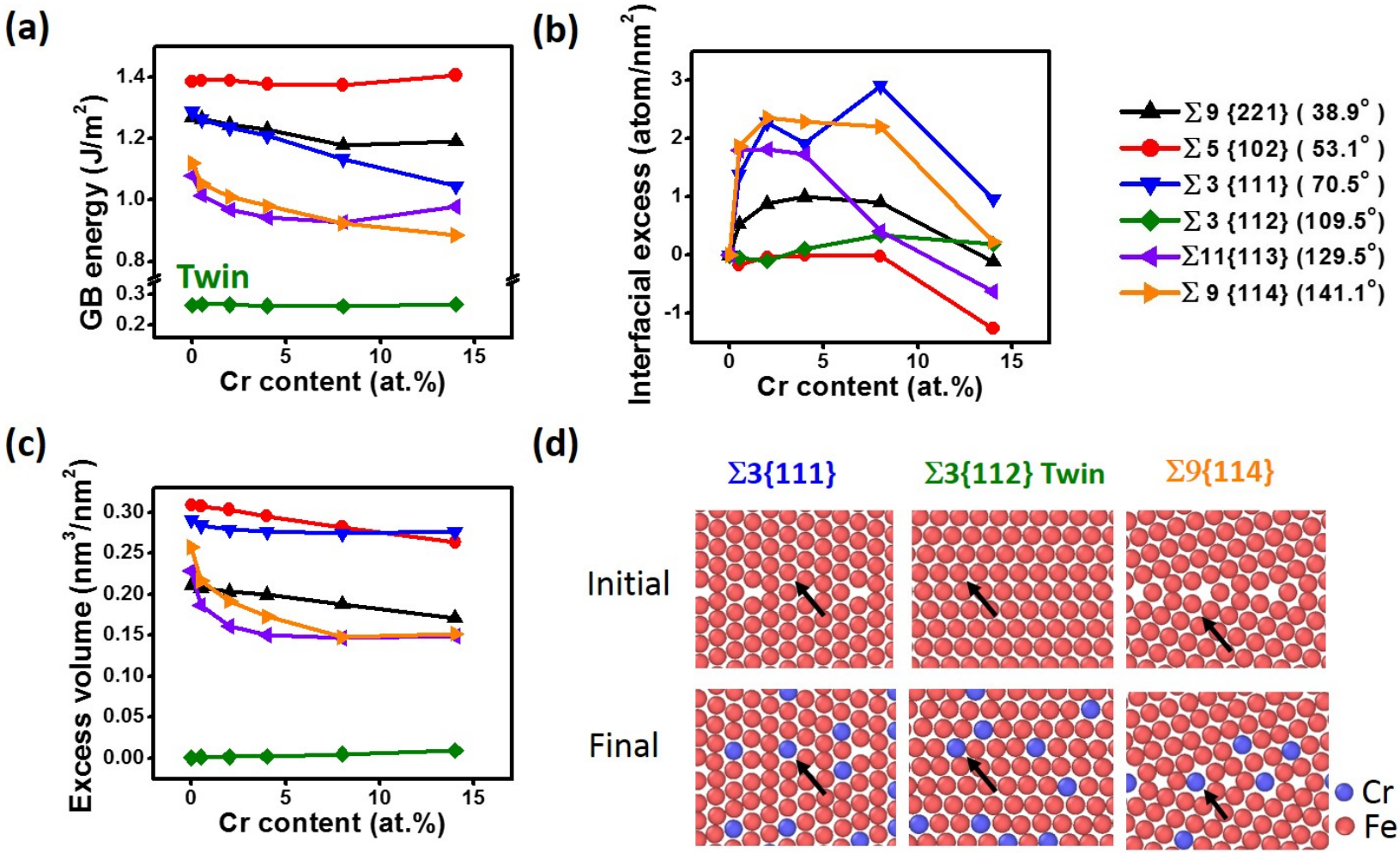

- In general, GB energy trended the excess volume behavior

(a) Calculated grain boundary energies **(b)** Interfacial excess **(c)** Excess volume for various Cr contents **(d)** Simulated atomic configuration for Σ-GBs with and without Cr segregation. The arrows direct to local lattice locations where relaxation from the initial to final states were tracked.

Zhou, X. et al. Sci. Rep. ***6****, 34642; doi: 10.1038/srep34642 (2016)*

Energetic distribution

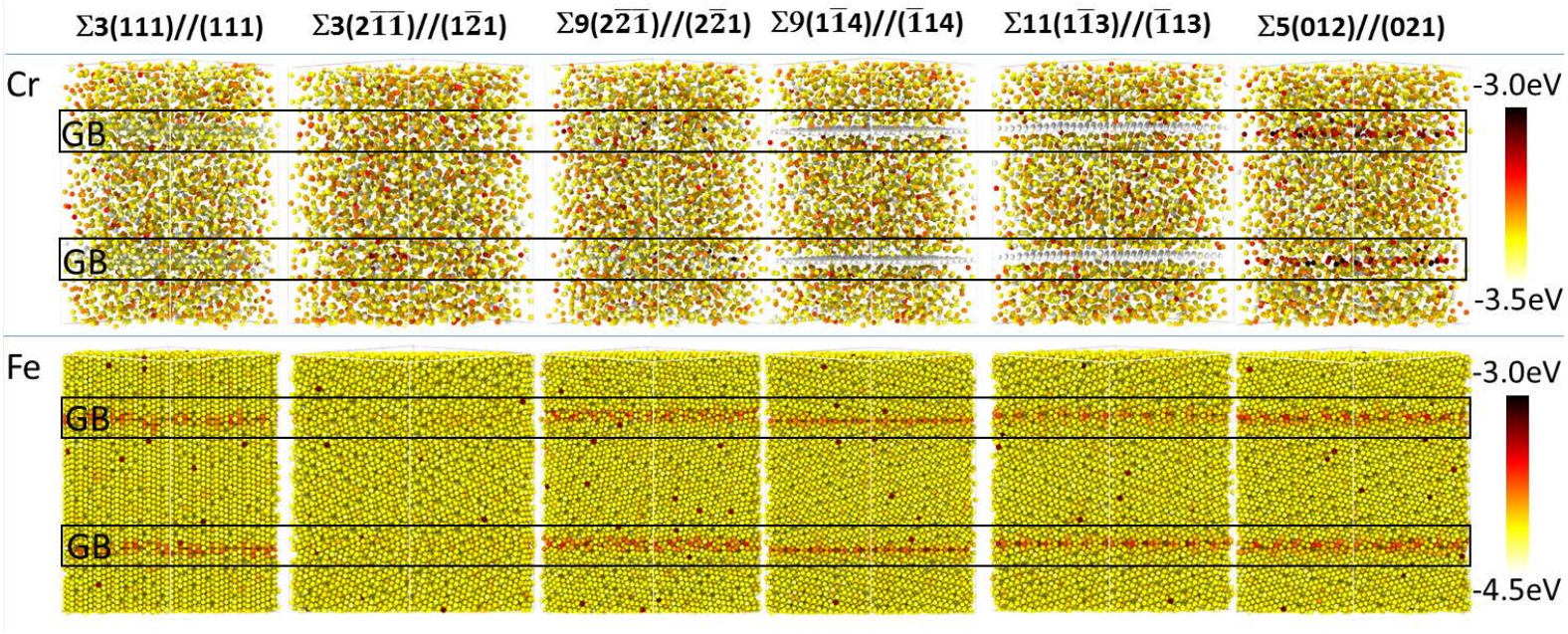

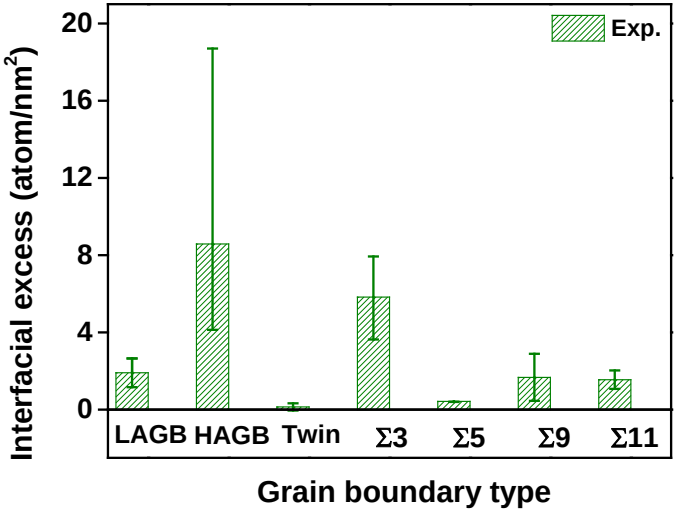

Most favorable energy state = white spheres

Least favorable energy state = red spheres

Good agreement of Cr preference in Σ9 and Σ 11 boundaries

*Zhou, X. et al. Sci. Rep. **6**, 34642; doi: 10.1038/srep34642 (2016)*

Heating during deposition

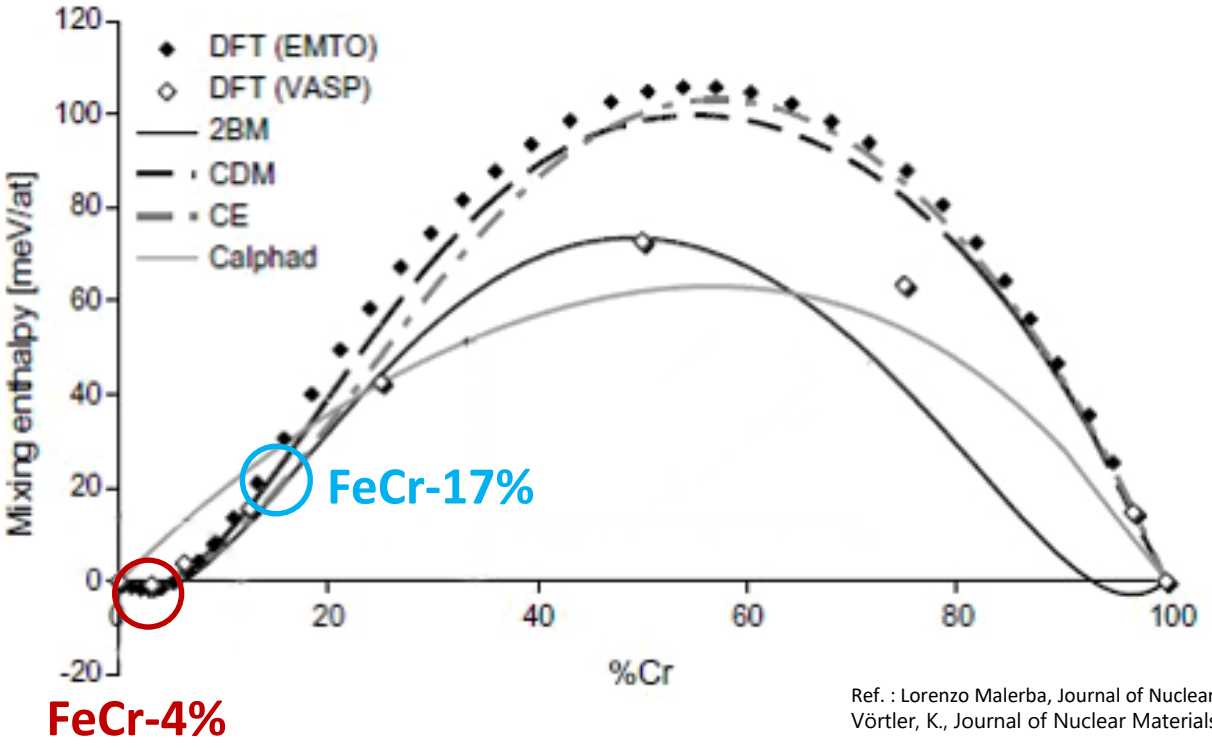

Ref. : Lorenzo Malerba, Journal of Nuclear Materials, (2008); Vörtler, K., Journal of Nuclear Materials, (2008)

- Two alloy targets, **FeCr-4%** and **FeCr-17%**, were chosen to deposit films
- Films were deposited at **room temperature**, **250 ºC** and **400 ºC** respectively

Grain size verses Deposition temperature

RT-FeCr4%

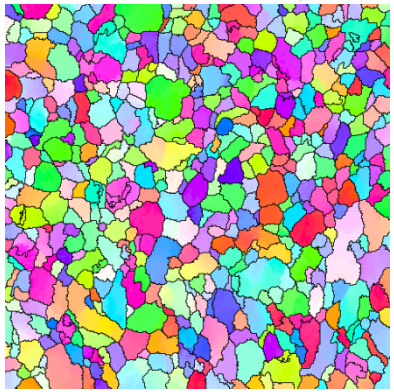

RT-FeCr17%

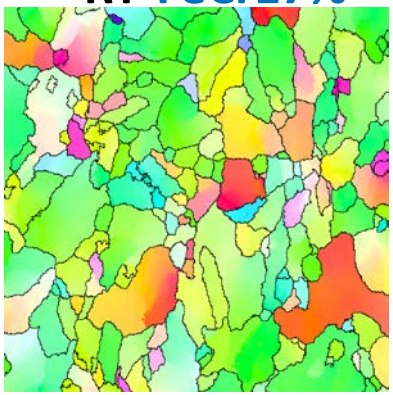

600 nm

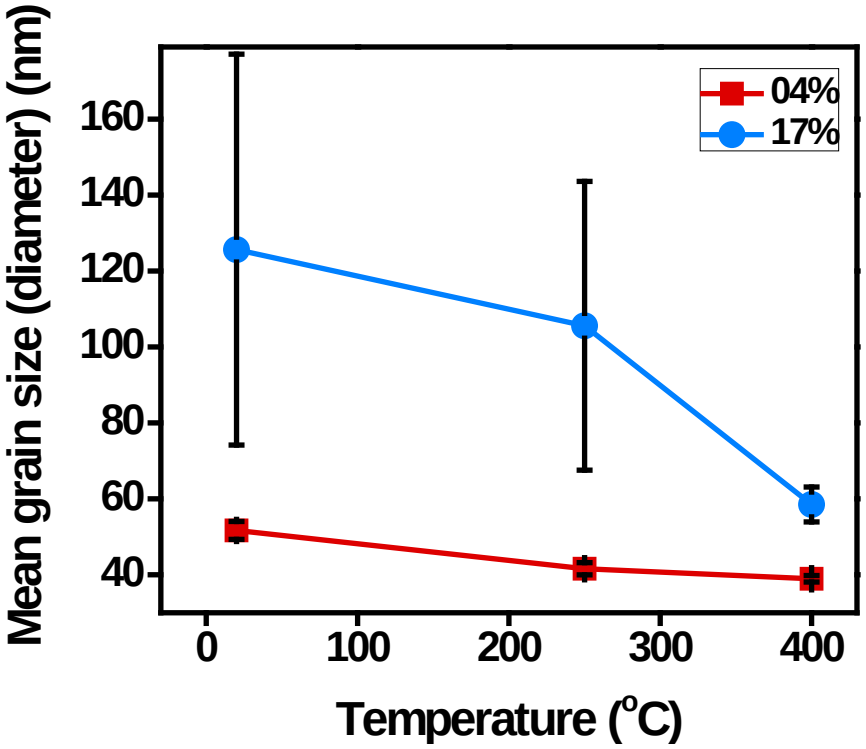

- At RT, increase of Cr promotes 101 texture
- Abnormal grain growth was found in FeCr-17%
- Grain size was reduced at elevated temperature.

400°C-FeCr4%

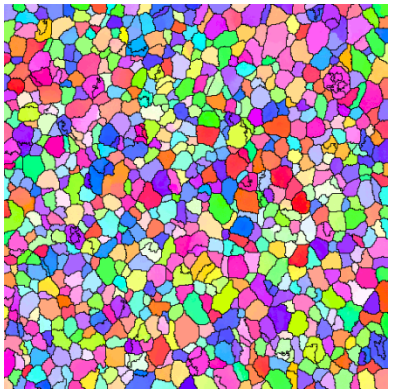

400°C-FeCr17%

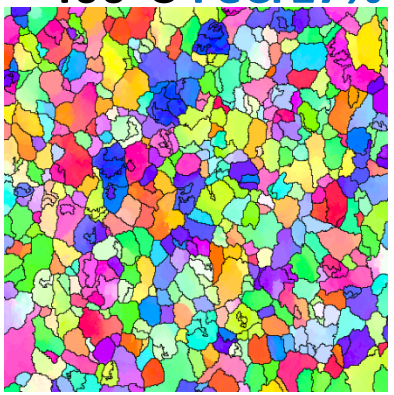

600 nm

APT analysis (FeCr17%) – *room temperature (RT)*

Plan-view tip - RT

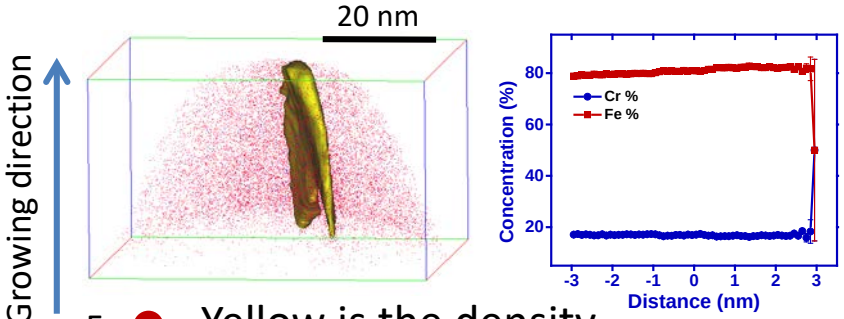

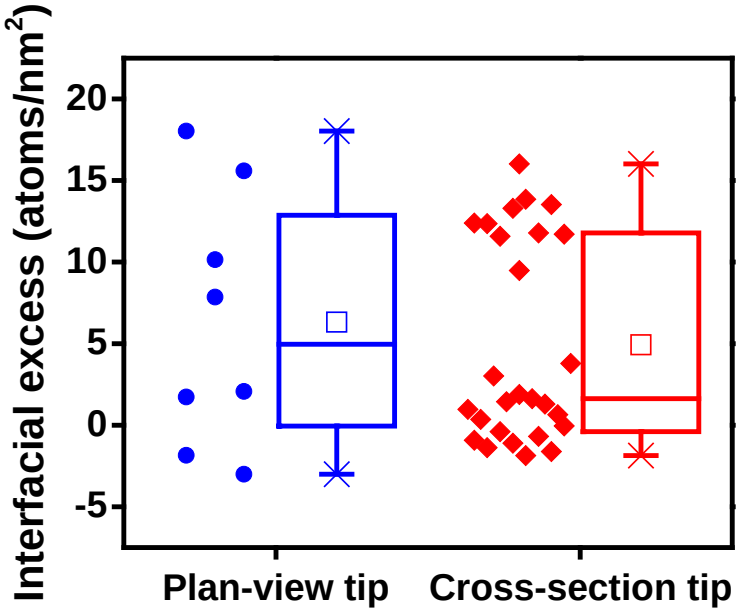

Cross-section tip - RT

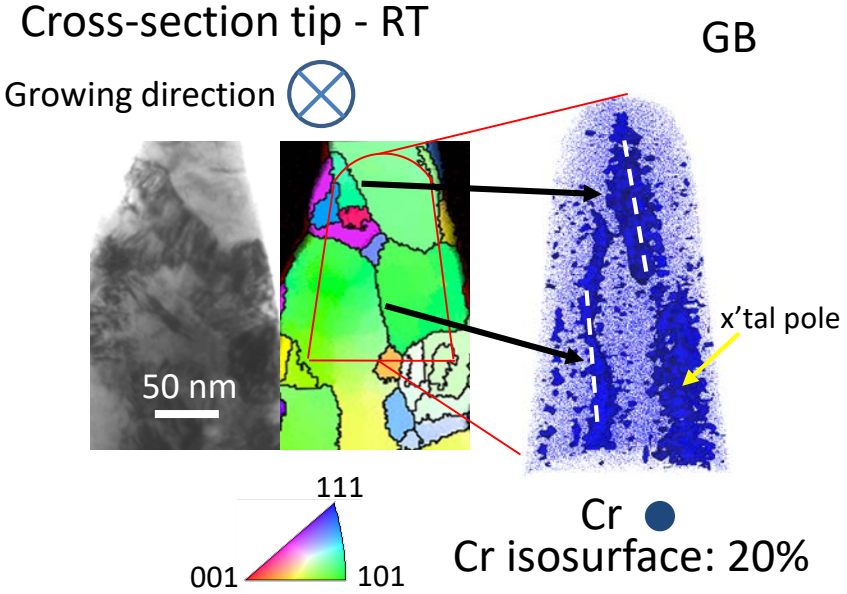

- **GB-solute specificity**
- **Inhomogeneous GB segregation changes the function Cr stabilization of grain size. Promoted AGG @ RT**

Zhou, X. et al. Sci. Rep. **6, 34642; doi: 10.1038/srep34642 (2016)*

Identifying GBs from APT data? *Difficult to ascertain decomposition and GB locations (for annealed films)*

2D contour plot from the APT data for the FeCr17% sample at 400^{o}C

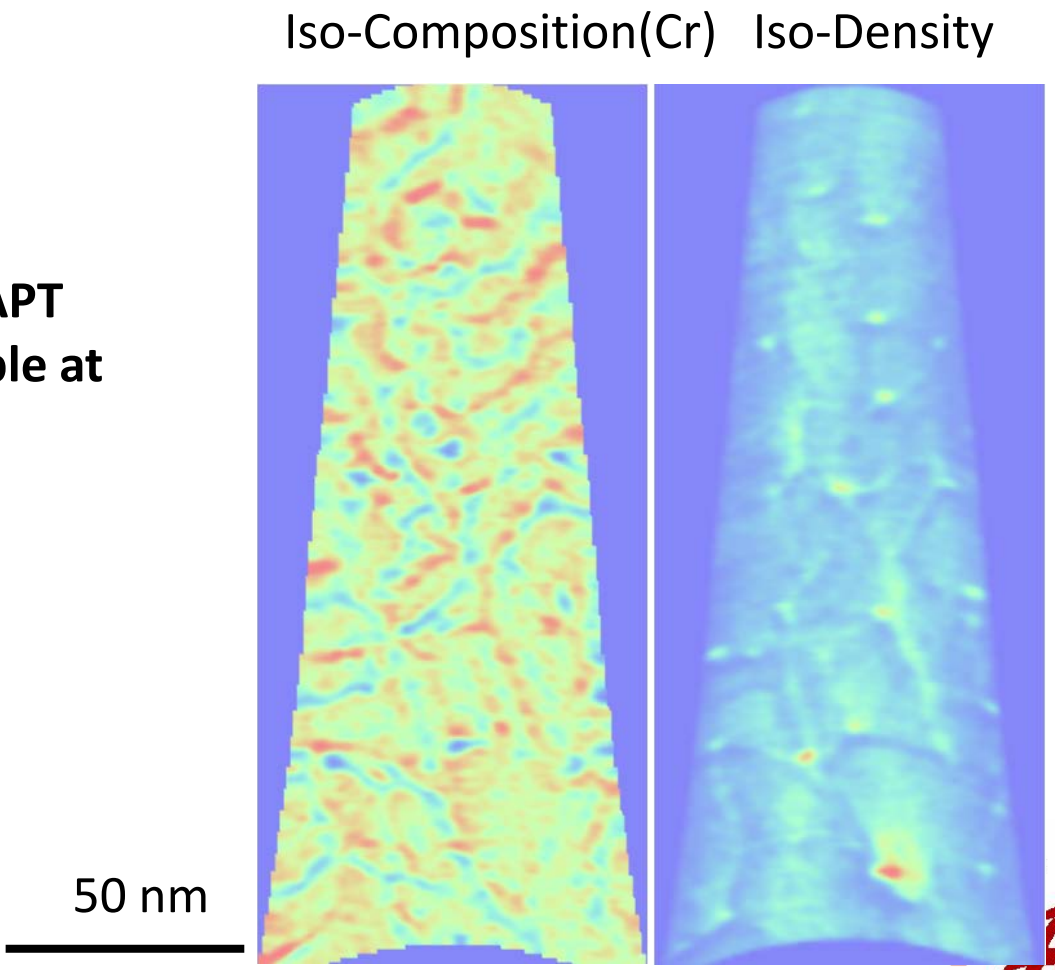

Correlated with PED data

2D contour plot from the APT data and GB map from PED data (FeCr17% 400°C)

APT: Composition(Cr) Density **PED:** GB type

Spinodal decomposition within the grain

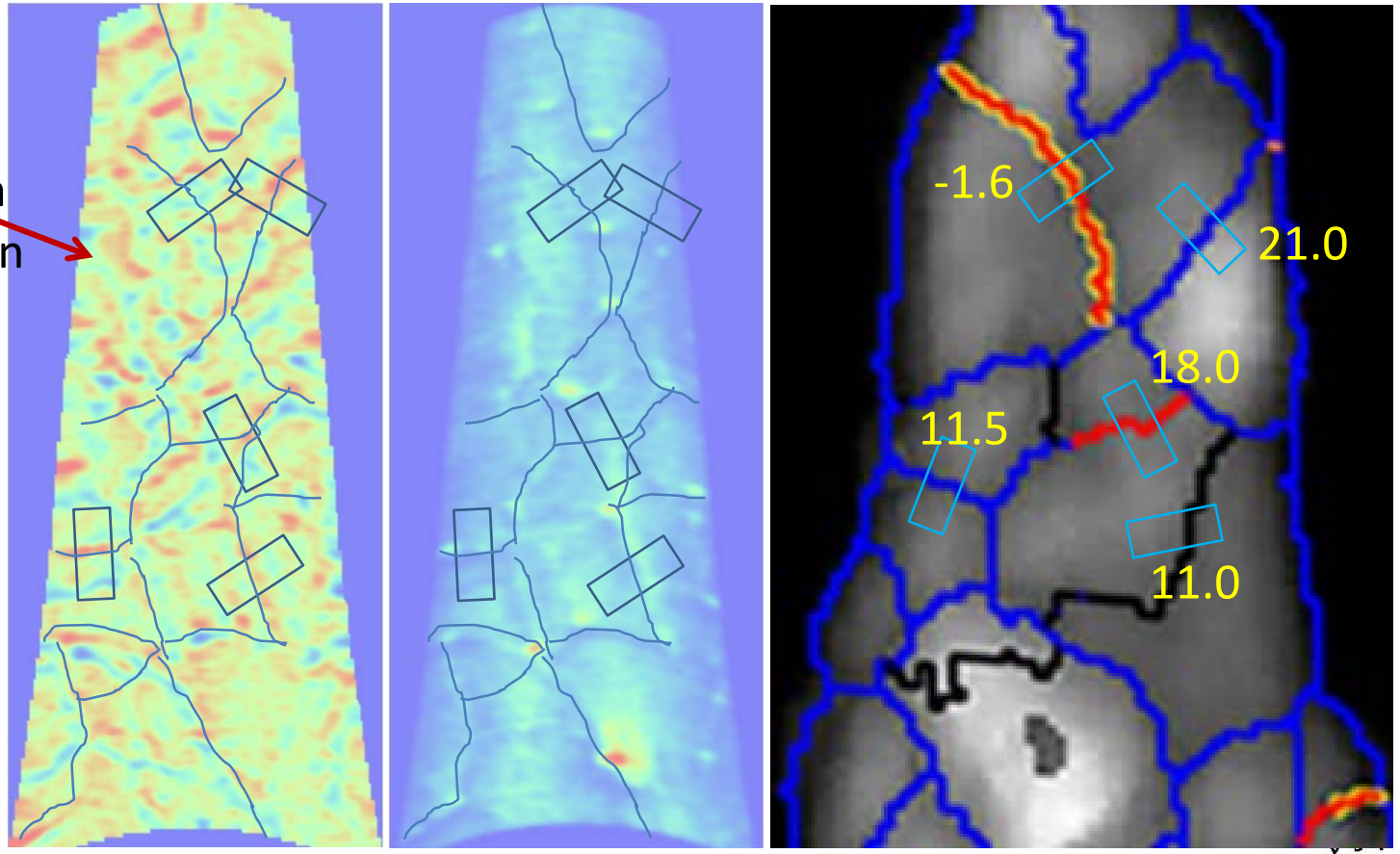

Segregation verses GB types - experimental

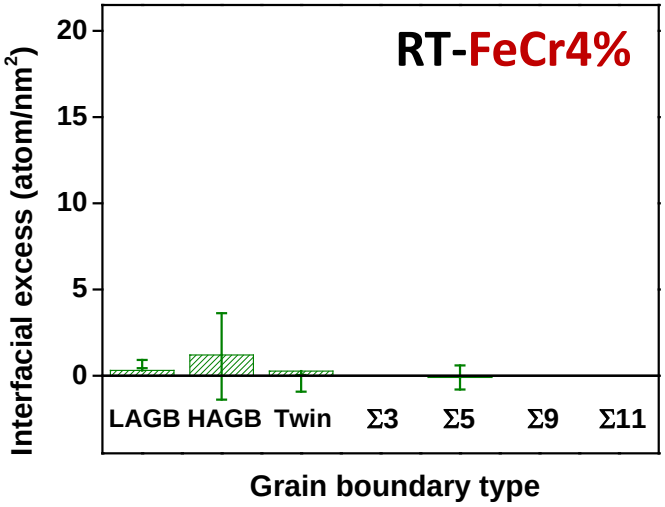

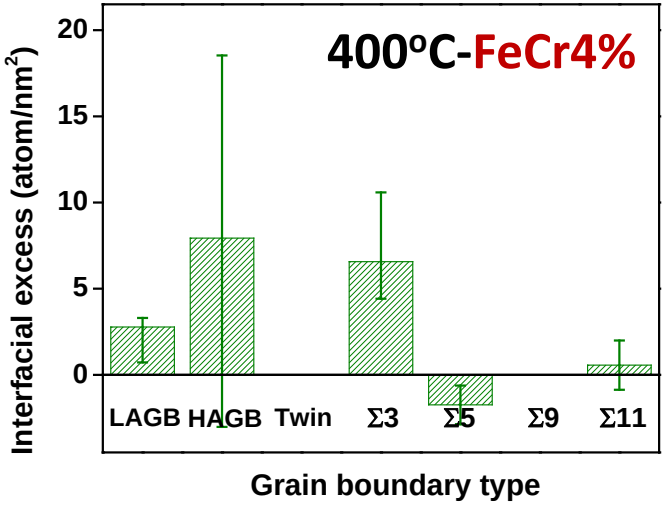

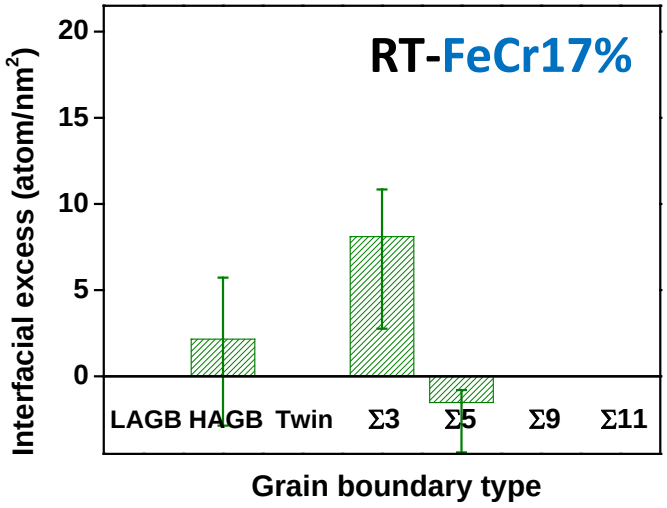

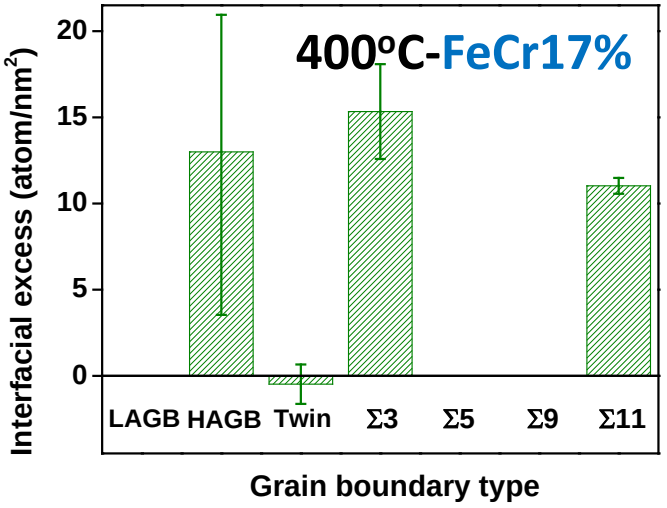

In situ annealing and PED correlation

- Two alloy targets, **FeCr-4%** and **FeCr-17%**, were existed
- 50 nm thick Fe(Cr) alloy films were deposited on the DensSolution chip.

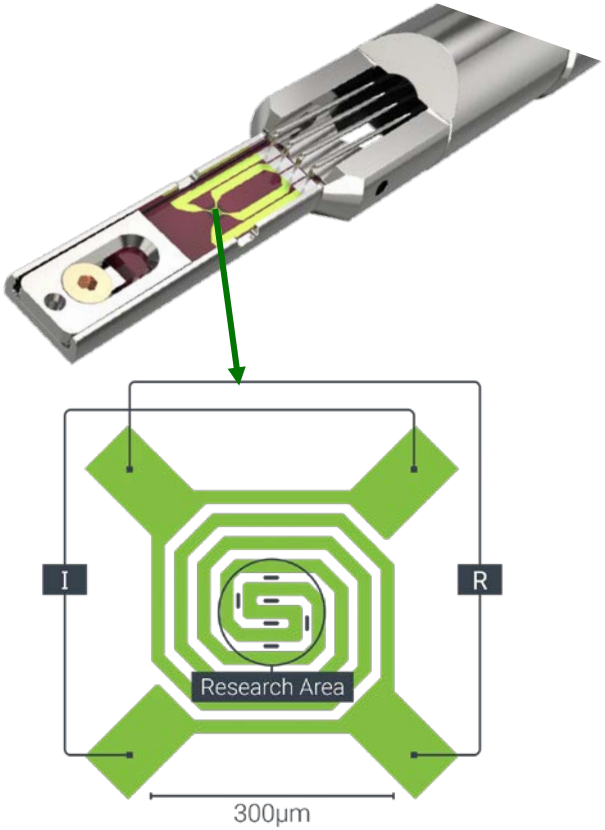

Heat treatment parameters:

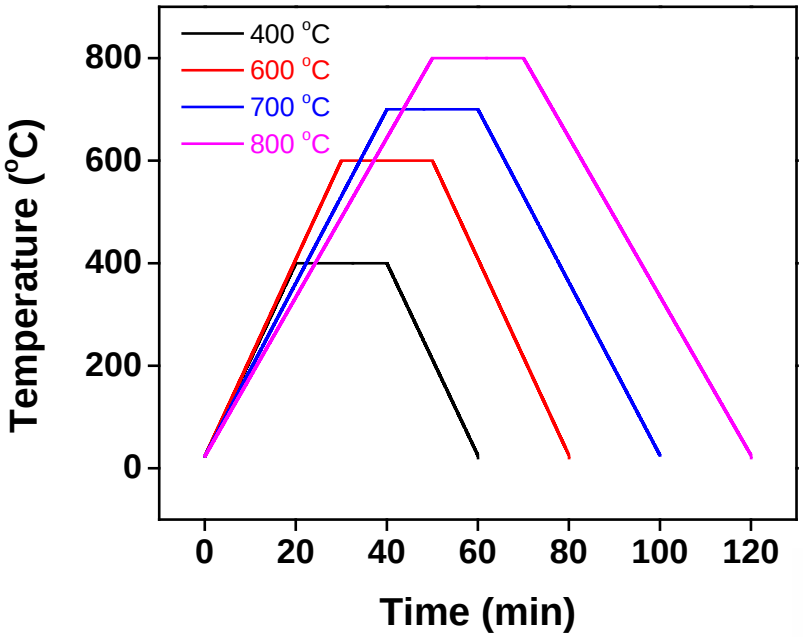

- Up to 1200°C at 10^6 °C/s
- Very thermally stable

http://denssolutions.com/products/heating/

Grain size verses Annealing temperature

17%Cr

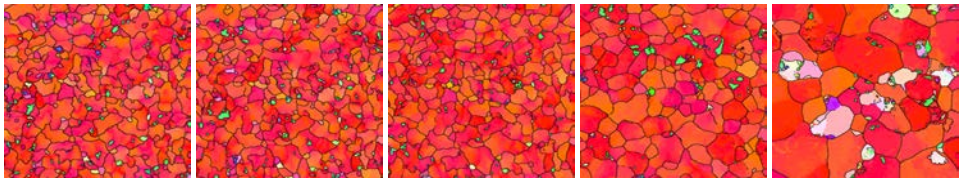

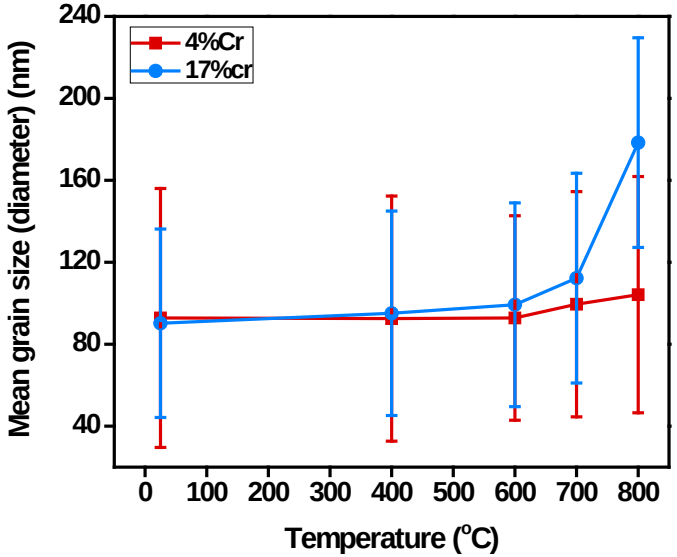

600 nm

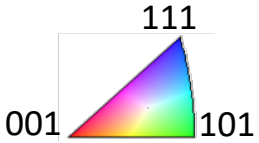

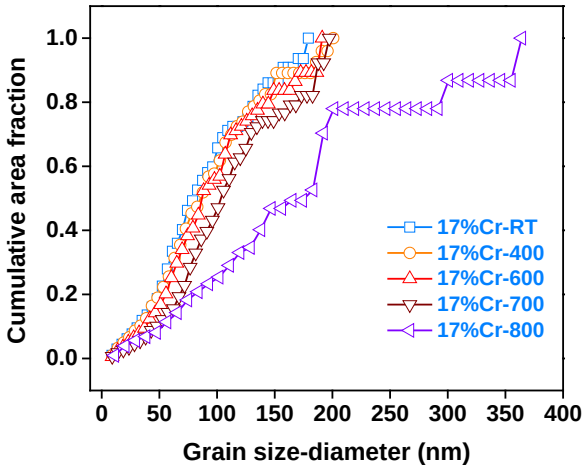

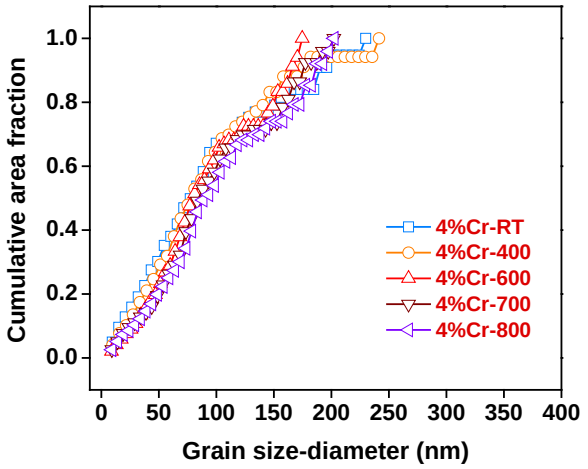

4%Cr

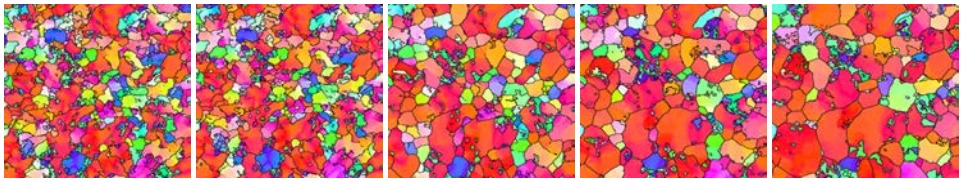

T

- For FeCr17%, obvious grain growth was observed at ~700°C
- For FeCr4%, no obvious grain growth was observed;
- @ 50 nm, {100} is the lowest energy surface (magnetic contribution)*
- @ RT, grain size of FeCr4% was different when compared 50 nm film and 300 nm film.

*M. Ropo, et al. PRB **76** (2007) 220401(R).

Oxidation!

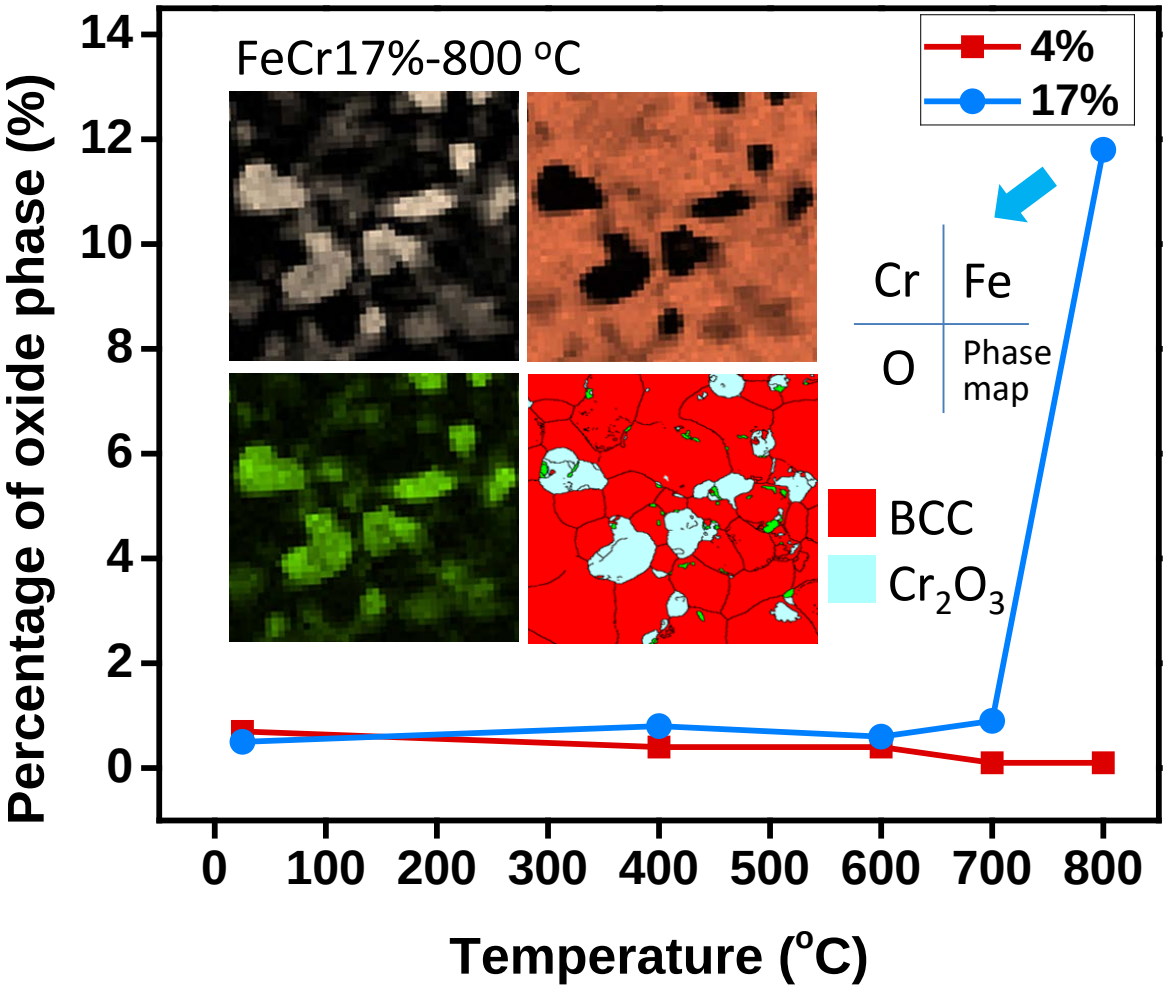

- For FeCr17% film:
  - ✓ Fe-Cr phase separation was observed @ 800°C
  - ✓ Oxides only form at Cr rich region
  - ✓ The composition of Cr oxides is about $CrO_{0.7}$
  - ✓ The structure of Cr oxides is Cr_2O_3 phase (167268-ICSD)
- For FeCr4% film:
  - ✓ No obvious oxide phase was observed at elevated temperature.

Understand anti-oxygenic properties (stainless steel)

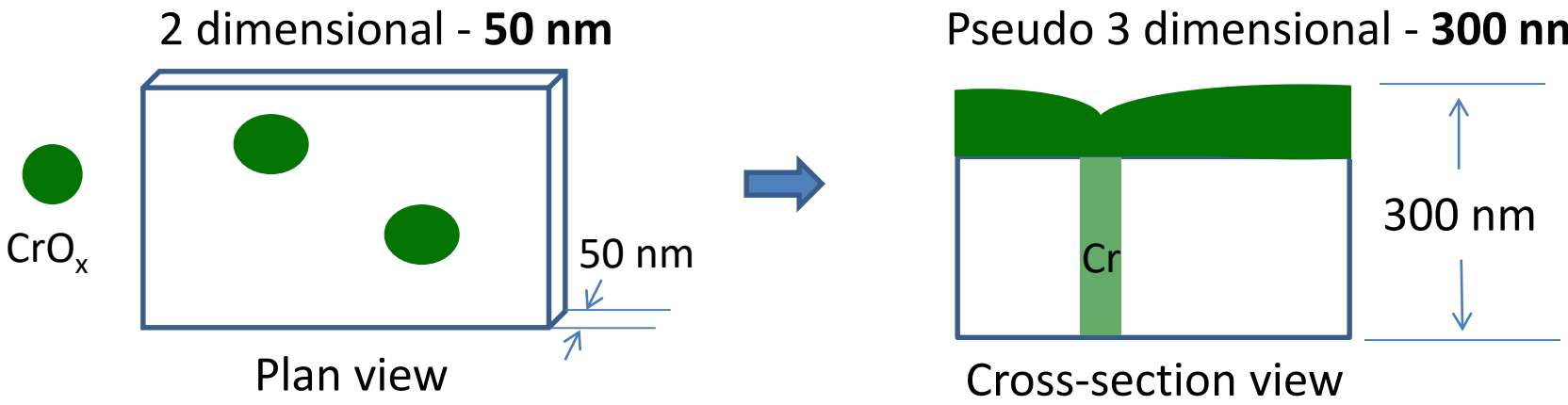

Phase separation promotes the formation of Cr_2O_3 phase

Low surface energy faciliates Cr atoms to surface which react CrO_x that protects Fe(Cr) from oxidation

Experimental verification (300 nm films annealed @700°C for 1 hour, 1X10^{-5} Torr)

Low Cr (~4%Cr)

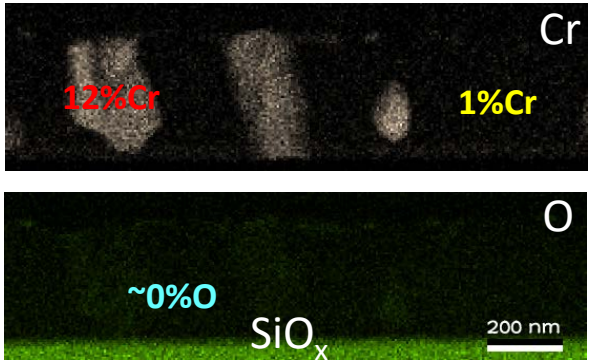

High Cr (~17%Cr)

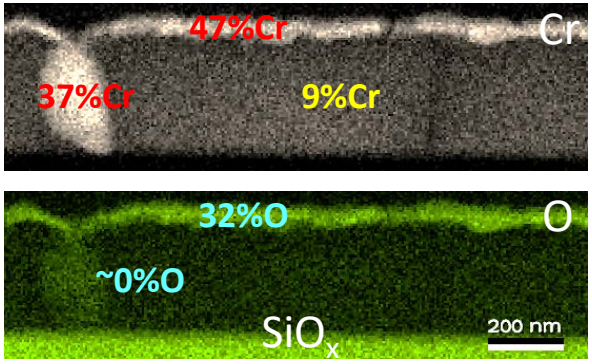

Surface chromium oxide layer was found on FeCr17% film but not on FeCr4% film*

*M. Ropo, et al. PRB **76** (2007) 220401(R).

Summary

- A series of Fe(Cr) nanocrystalline films were sputter deposited.
  - ✓ RT: At low Cr content (4%), the grains grew; at higher Cr contents (8%), the grains refined; AGG noted (17%)
  - ✓ Increasing Cr promoted more {110} texture
  - ✓ Annealing (400^{o}C) resulting in Cr segregation in all concentrations (4%, 17%) with grain refinement.
- GB-solute segregation specificity
  - ✓ PED-APT revealed grain boundary specific segregation
  - ✓ MD/MC model able to capture similar behavior
- *In situ* annealing
  - ✓ PED revealed a {100} texture, contributed to very thin thickness and magnetic contribution
  - ✓ Grain growth observed
  - ✓ At 800^{o}C, Cr-oxide was noted in the 17% sample (absent in 4%)
  - ✓ *Ex situ* anneals for thicker films reveal segregation and migration of Cr solute to the surface providing a protective oxide scale (absent in 4%)

The Application of Precession Electron Diffraction to Cross-correlative and *in situ* Microscopy

Xuyang Zhou[1], Qianying Guo[1], Justin Brons[2],
Khalid Hatter[3], Brad L. Boyce[3]
Gregory B. Thompson[1]

[1] *University of Alabama*
[2] *now at Apple*
[3] *Sandia National Laboratory*

This work was funded with support from the Army Research Office-W911NF1310436 and W911NF1510405 (DURIP) and the National Science Foundation DMR-1709803

The University of Alabama
Tuscaloosa, AL

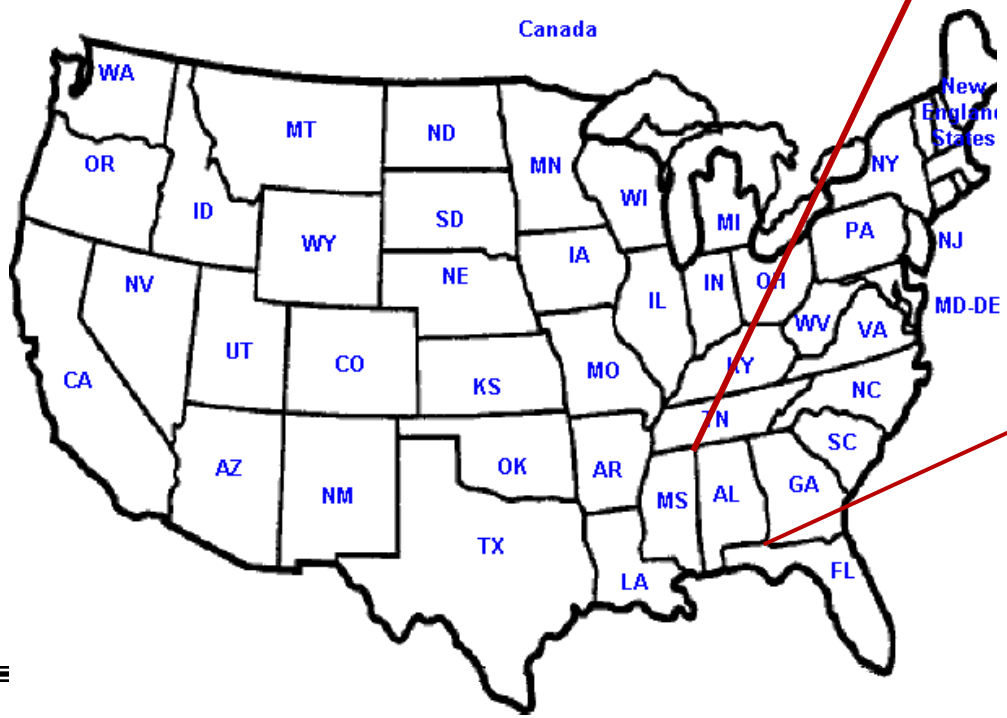

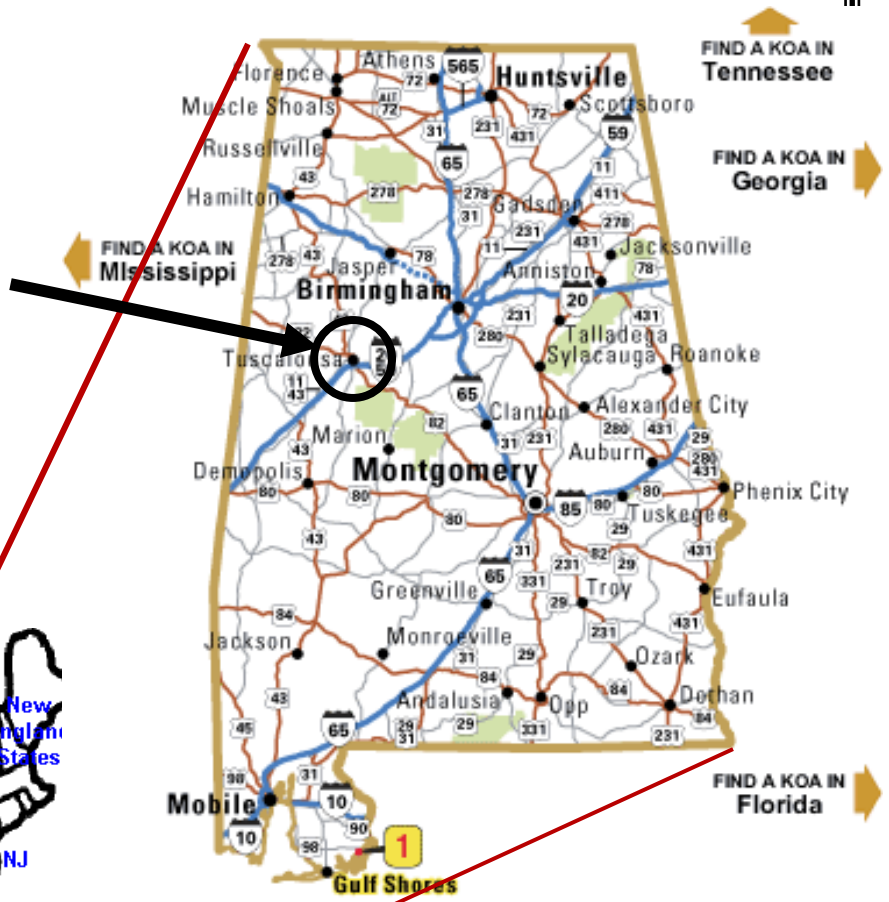

The University of Alabama

- Founded in 1831 (5th Oldest College of Engineering (1836) in the United States)

- Student enrollment: 38,500+ (>50% out-of-state)
  - Approximately 5100 students in COE with
  - In 2013, complete final 4-phase Science & Engineering $300M complex
  - Central Analytical Facility: $10M of various microscopes
    - FEI Tecnia F20 (S)TEM
    - FEI Quanta & Tescan Lyra dual beam FIBs
    - Cameca Instruments LEAP 5000XS
  - Metallurgical & Materials Engineering
    - 10 Faculty (fuel cells, thermal barrier coatings, magnetism, casting, etc.)
    - 120ish undergraduates; 30ish graduate students




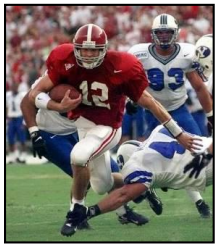


The Group's Research Activities:

ThompsonResearch.ua.edu

Magnetic materials

Hard drive materials

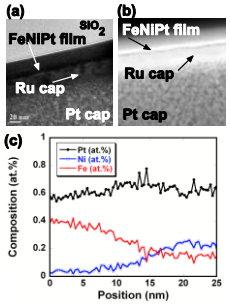

Soft magnetic composites

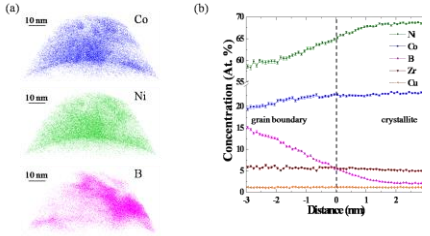

Phase and Deformation in UHTCs

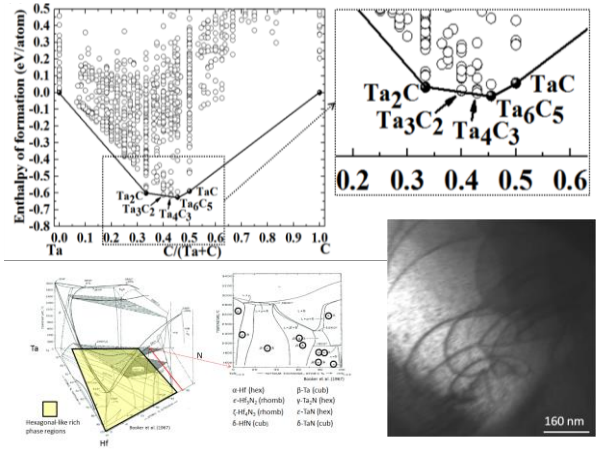

Shape Memory Alloys

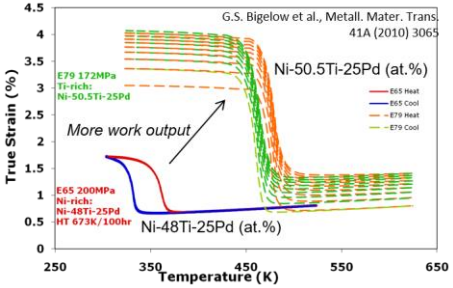

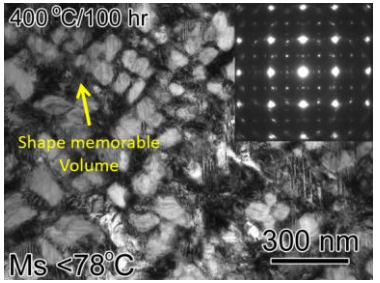

Laser-based Fiber Growth

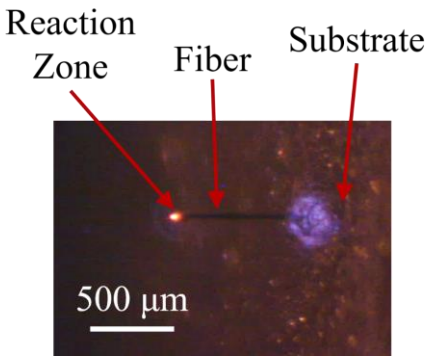

Nanocrystalline Alloys

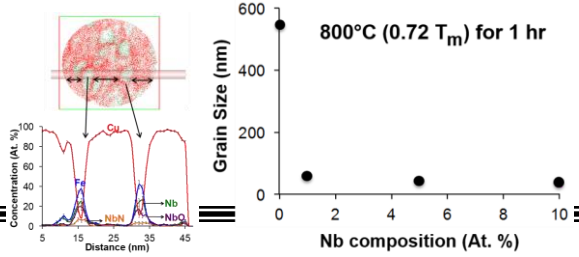

Thin Film Coatings

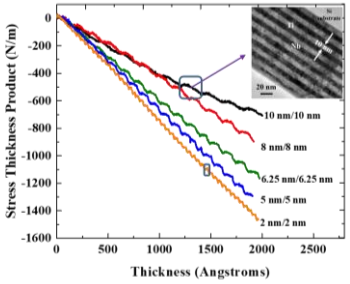

Grain Characteristic are Essential for Material Properties

Some examples…

Hall-Petch

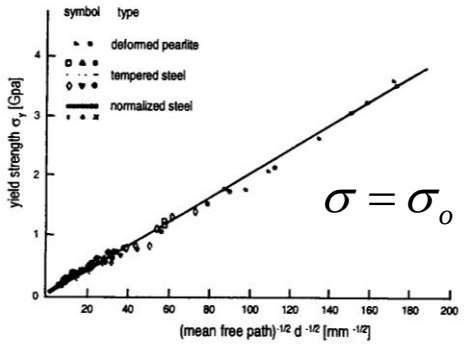

$$\sigma = \sigma_o + \frac{k_y}{\sqrt{D}}$$

Magnetic Recording Hard-drives

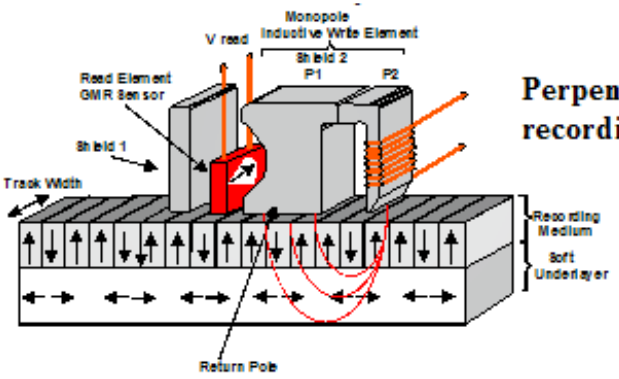

High frequency Power Transformers

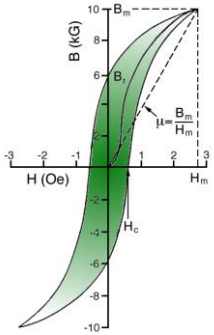

Residual Stress in Thin Films/Coatings

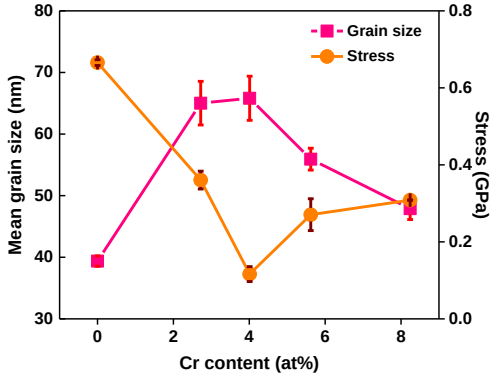

CAPSTONE ENGINEERING

Probing Nanoscale Boundaries:

Application of Precession Electron Diffraction (PED)

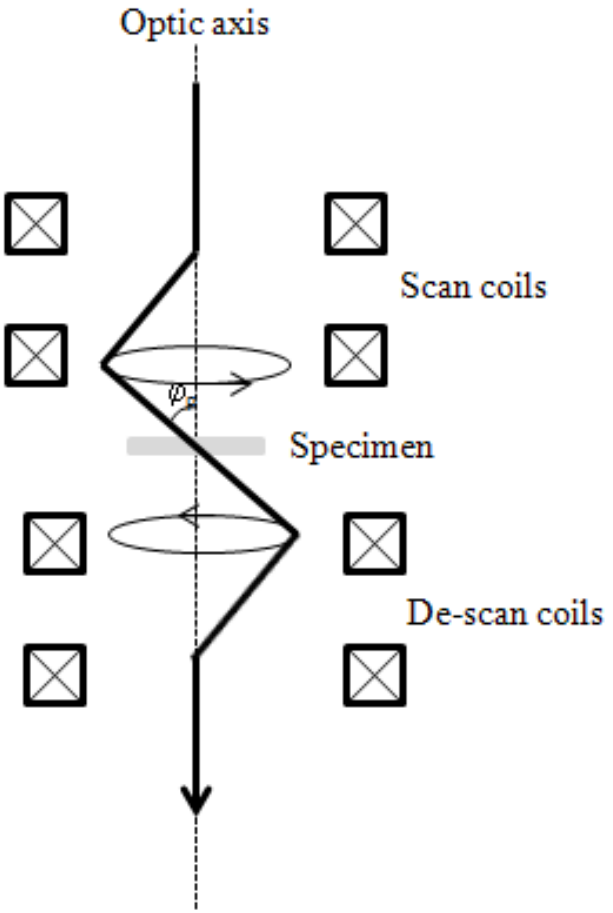

By precessing the beam, the following advantages are present:

- "Averages" the diffraction events yielding more of a kinematical effect = more uniform intensities
- Slices more of reciprocal space = more diffraction spots (higher reliability for indexing)
- Focused beam provides for higher spatial resolution (~1-3 nm)

R. Vincent, P.A. Midgley, Ultramicroscopy 53 (1994) 271

Precession-Electron-Diffraction (PED)

#1: Precess the beam

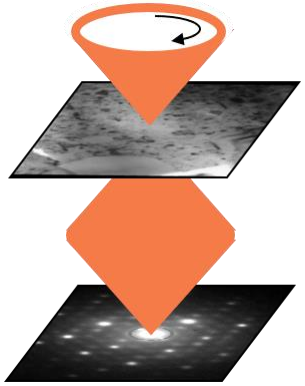

#2: Raster

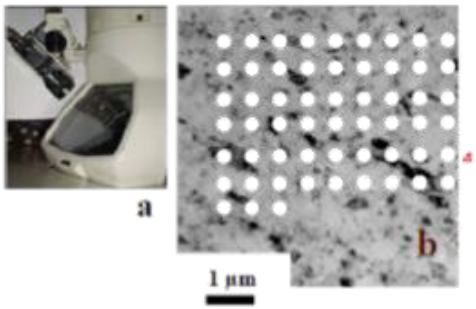

#3: Compare experimental DP to simulated orientations for matching

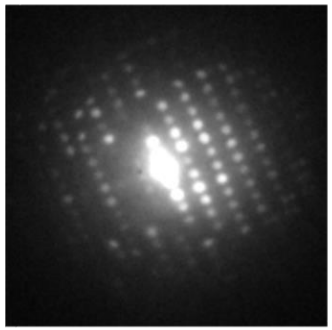

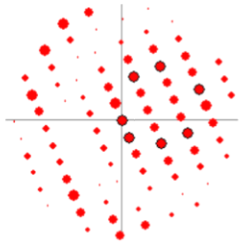

#4: Out put phase and orientation maps

Phase ID

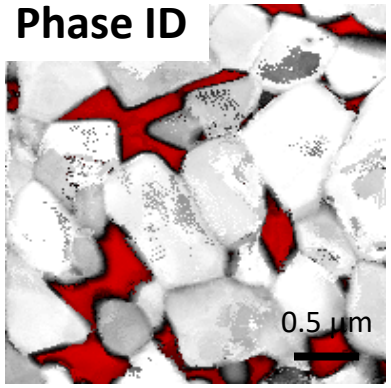

Orientation mapping

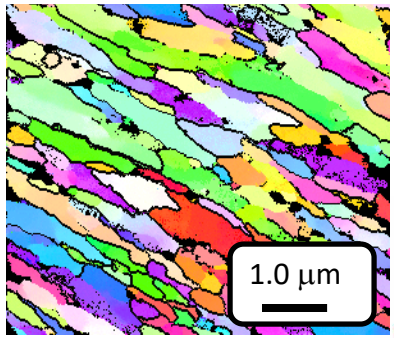

Images courtesy of E. Rauch

Reconstruction Issues and Ambiguities

Things to watch out for…

Thru-foil thickness - grains overlapping

Manifestations of these artifacts include a high density of smaller boundaries of the same type (with the creation of these boundaries within one to a few pixels in size)

Manual corrections (pseudo-symmetric clean-up routines) can be applied; proper nearest neighbor correlation values

Flags –

(1) Low reliability indexing of regions – sometimes cannot be helped if severe deformation strain is present

(2) Systematic row of single reflections – not capturing HOLZ

Azimuthal orientation - *"180^{o} ambiguity"* Spots being indexed as *(hkl) or (-h-k-l)* in the ZOLZ - creates inversions and false boundaries

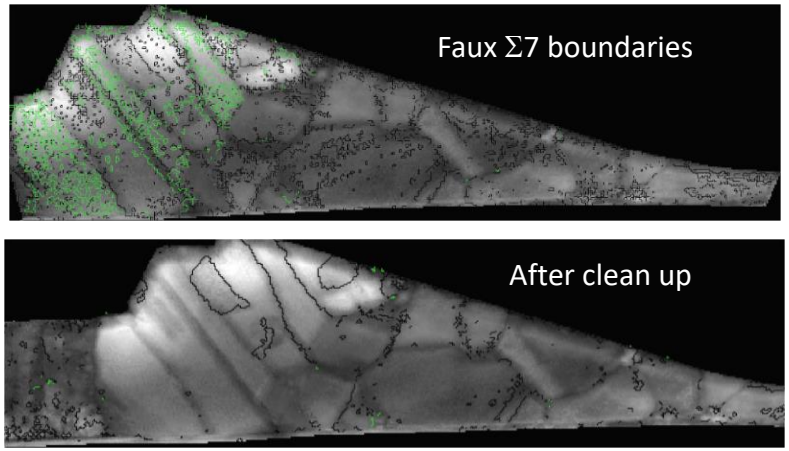

Topical Applications to Discuss

- **Correlative PED-APT**
  - F(Cr) nanocrystalline thin film system
- **Correlative PED-EDS**
  - *in situ* oxidation of Fe(Cr)
- **Correlative PED-deformation**
  - Cryogenic induced grain growth
  - *in situ* nanoindentation Cu
  - *in situ* nanoindentation of Cu/CuZr multilayers

PED-APT: Case study: Fe(Cr)

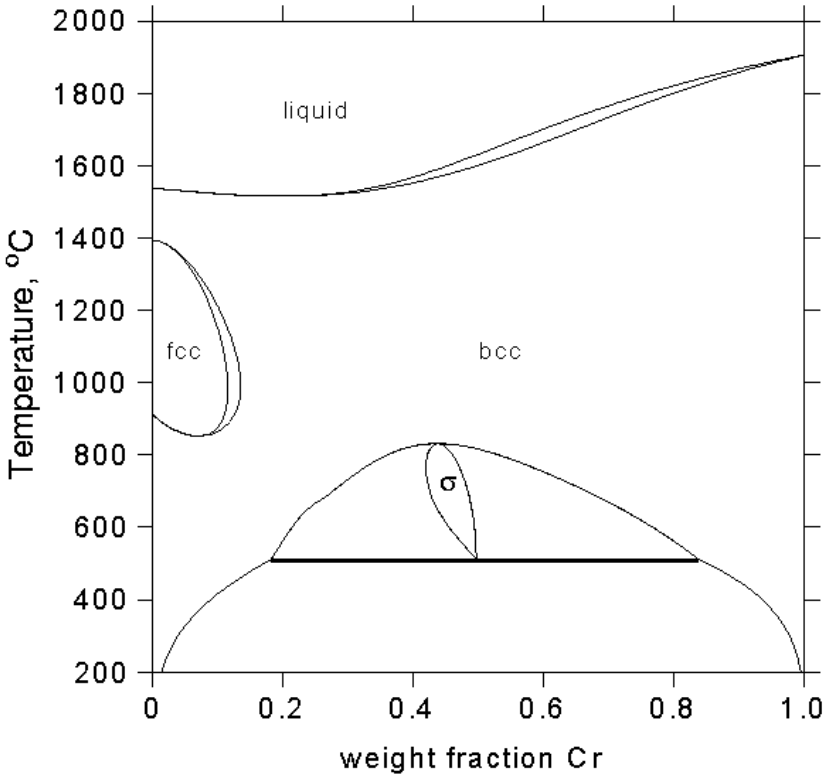

- Both BCC structures
- Exhibits a miscibility gap
- Technically important as basic building block species for stainless steel

- *How does segregation regulate nanocrystalline grain behavior in Fe-Cr?*
- *How does segregation scale with grain boundary types?*

Sputter-deposited Fe(Cr) nanocrystalline films

- <10^{-8} Torr
- ~2 mTorr UHP Ar
- Co-deposition from Fe and Cr targets
- RT deposition (and elevated temperature depositions when indicated)
- 30-300 nm thicknesses

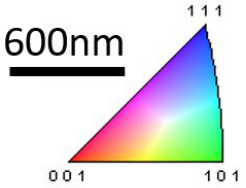

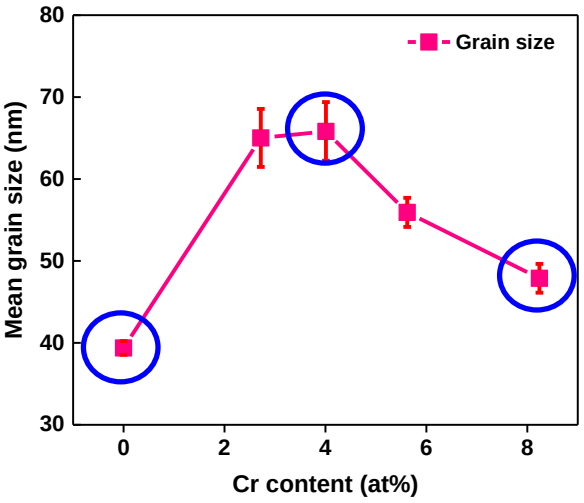

Cr solute changes the Fe grain size

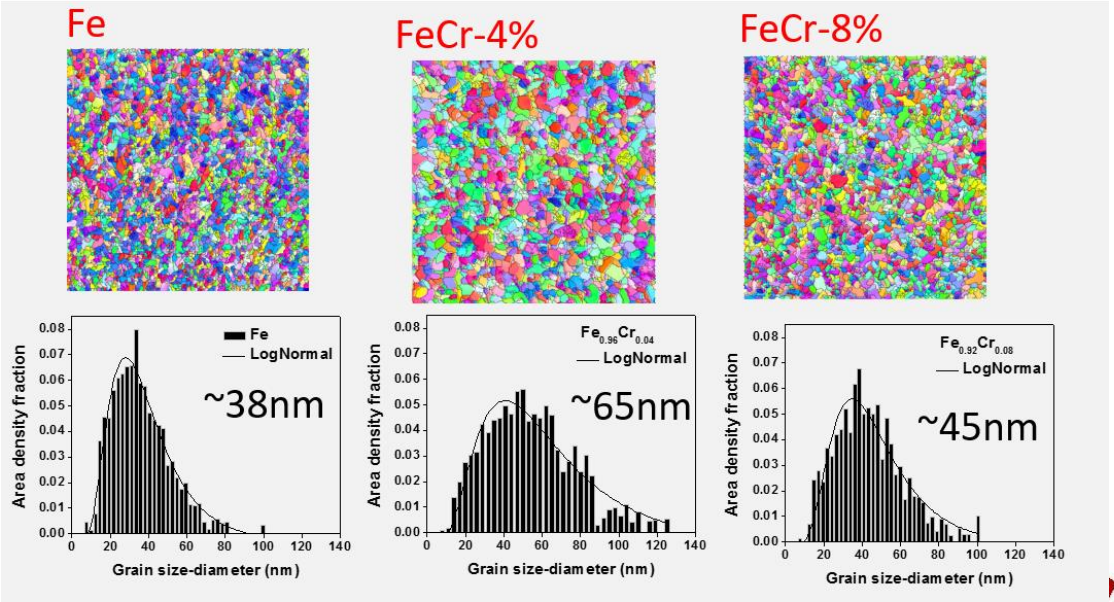

Initial APT analysis

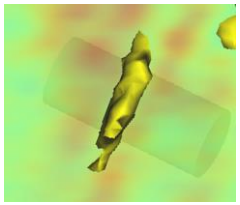

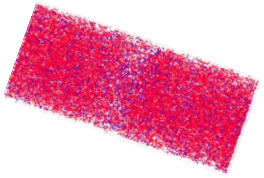

Fe
Cr

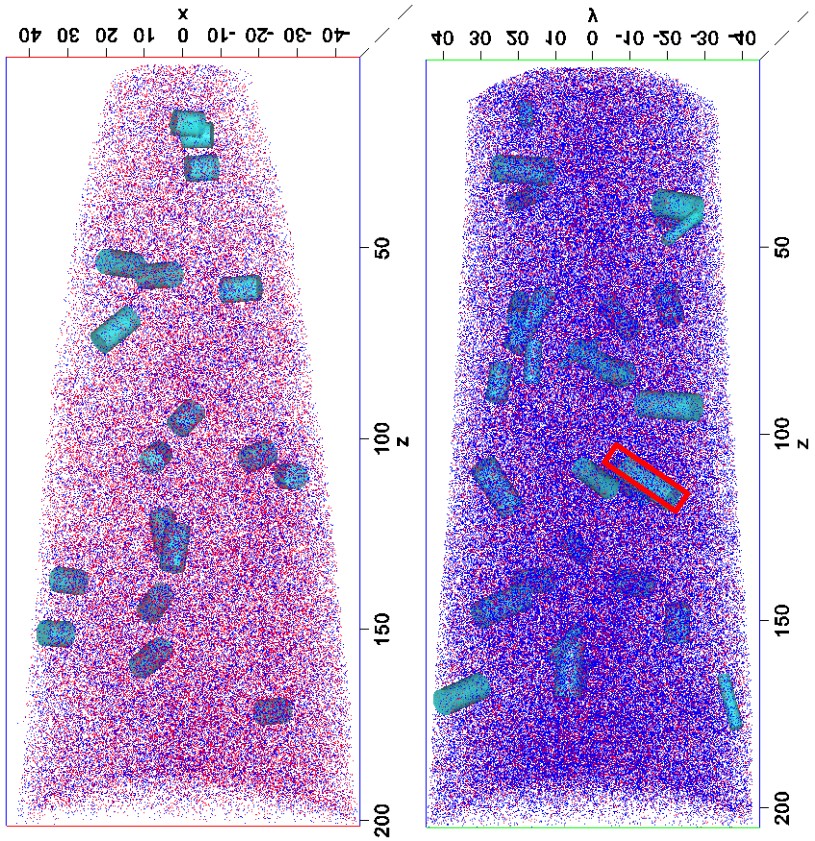

FeCr-3%

FeCr-8%

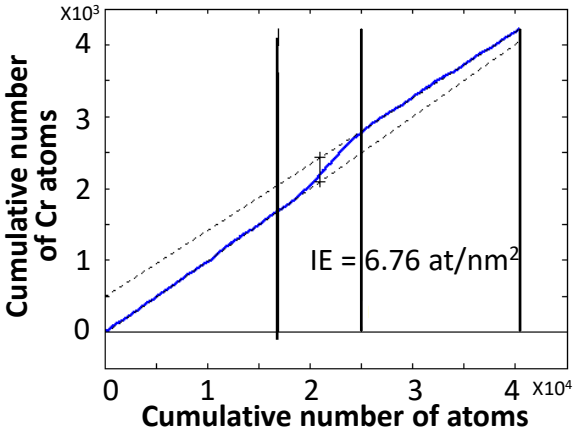

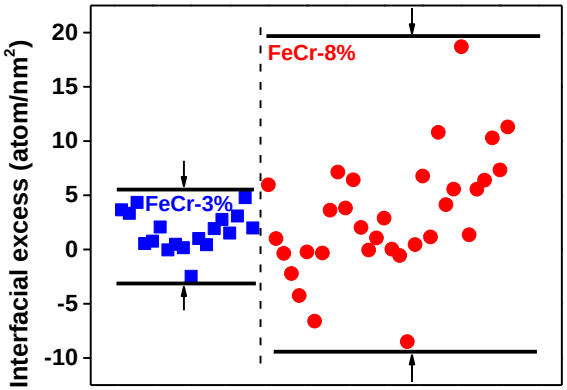

- The Interfacial Excess (IE) values of different GBs are quite different
- The range of IE value of FeCr-8% is larger than FeCr-3%.

*X. Zhou, et al. Thin Solid Films **612** (2016) 29-35.*

Phase separation → grain refinement growth

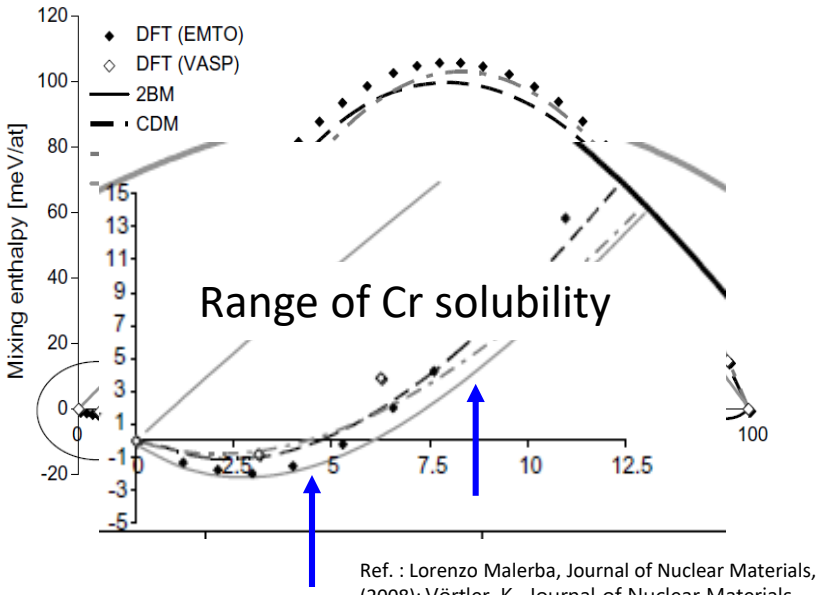

Ref. : Lorenzo Malerba, Journal of Nuclear Materials, (2008); Vörtler, K., Journal of Nuclear Materials, (2008)

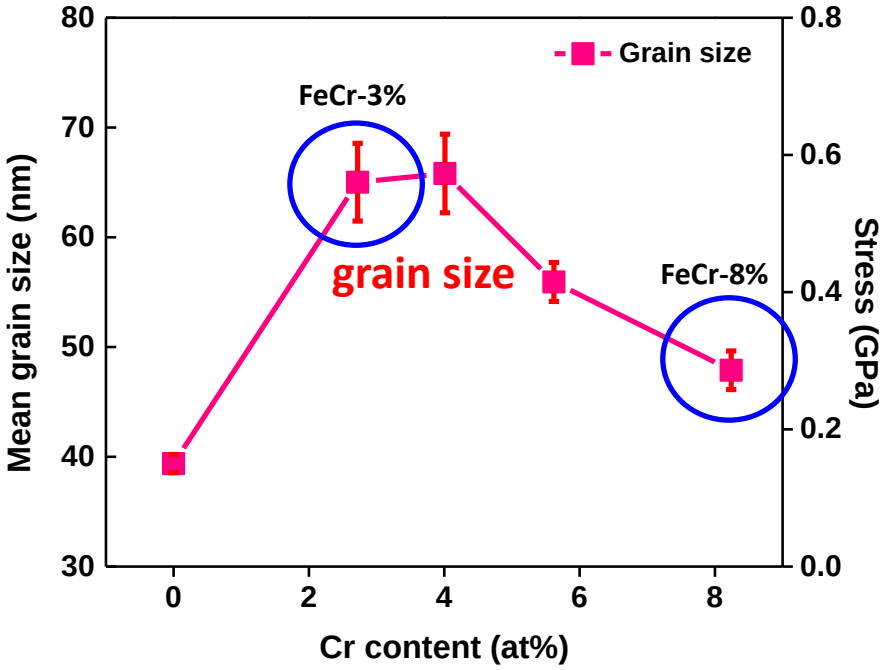

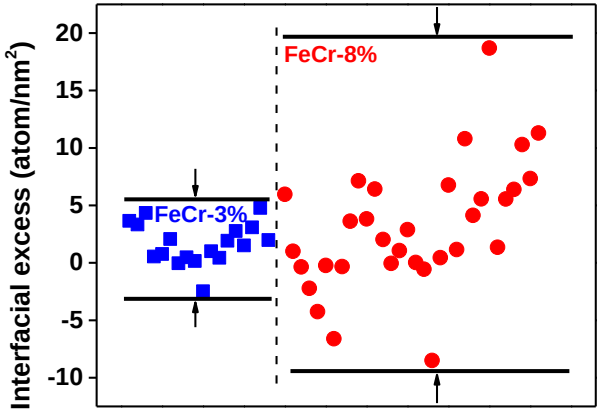

Cr content in the grain boundaries acts as a grain refiner.

*X. Zhou, et al. Thin Solid Films **612** (2016) 29-35.*

What is contributing to the interfacial excess spread?

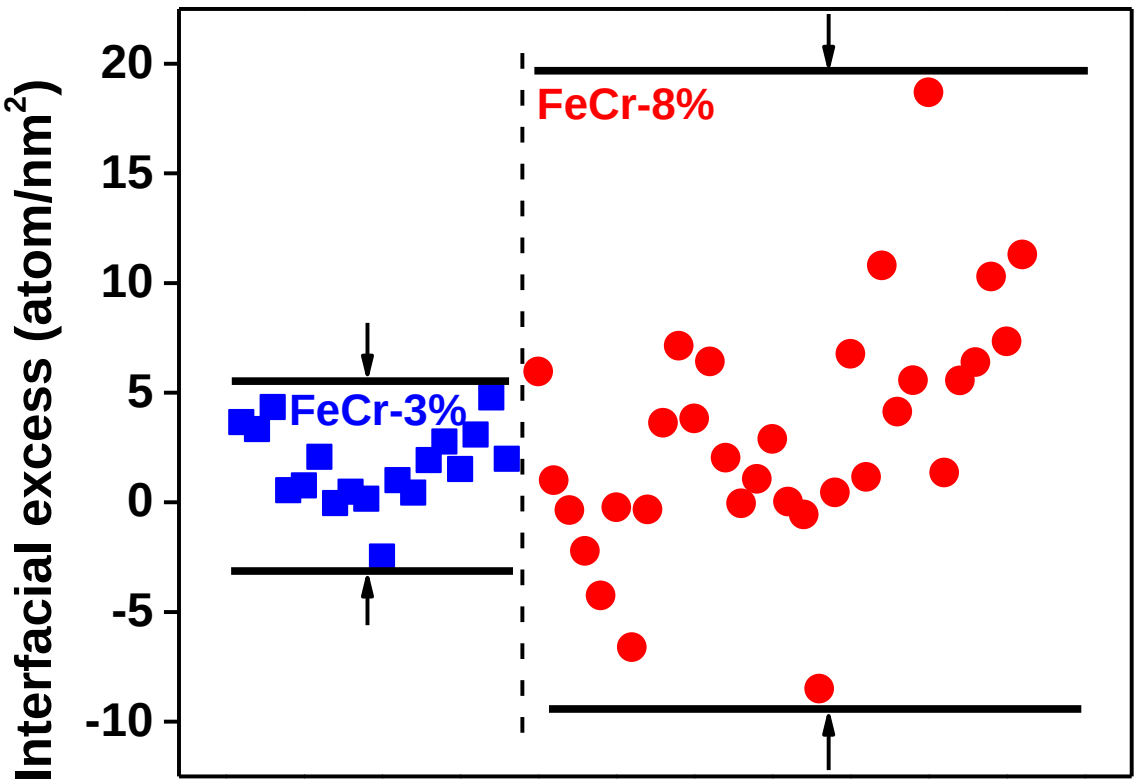

Grain Boundary Structure & Energy

Grain boundaries are diverse in their energy, structure, and mobility

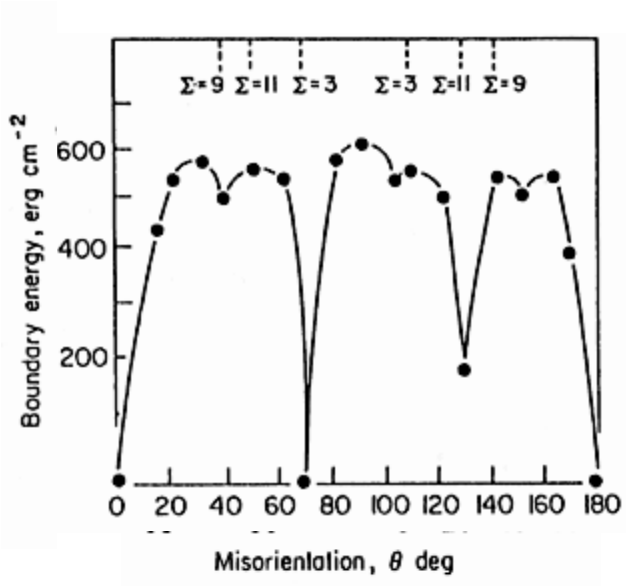

http://www.bing.com/images/search?q=concident+site+lattices+energies&view=detailv2&&id=6FE00B5BFE42DB142F14022C33DC3B6A737084F0&selectedIndex=0&ccid=1Yh1GLU7&simid=608012120133861912&thid=OIP.Md5887518b53ba78a5dbeb292d64d8921o0&ajaxhist=0

CSL or special character grain boundaries

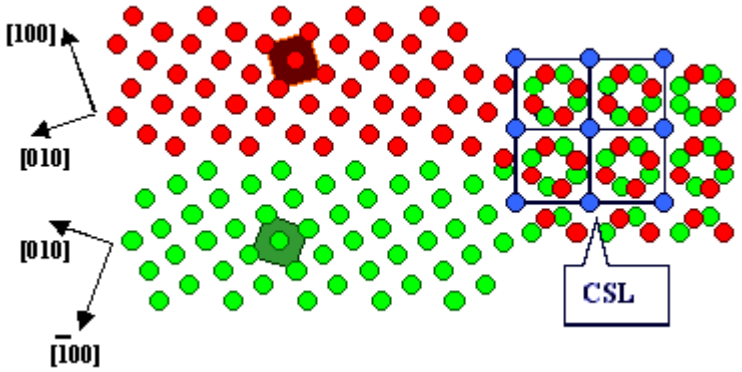

http://www.bing.com/images/search?q=concident+site+lattices+energies&view=detailv2&&id=6FE00B5BFE42DB142F14E4333C5083F589F2D15D&selectedIndex=1&ccid=7n4lN%2fZq&simid=608017398656994819&thid=OIP.Mee7e2537f66a3d9911d5b19927a1e5c2o0&ajaxhist=0

Quantifying Solutes in GBs – Cross correlation microscopy

- Requires **high spatial resolution** and **high chemical sensitivity**

Precession Electron Diffraction (PED)

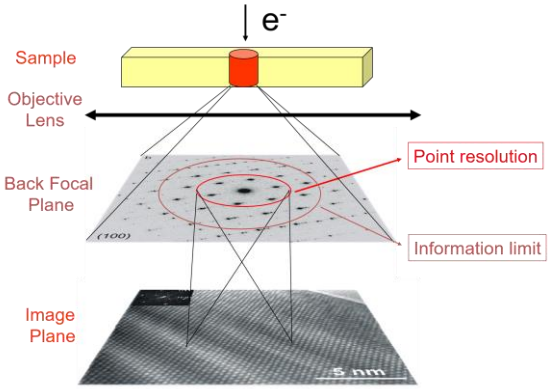

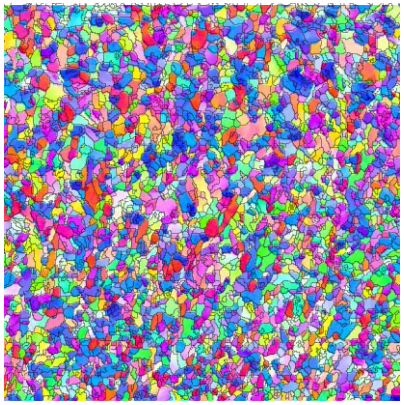

400 nm

Atom Probe Tomography (APT)

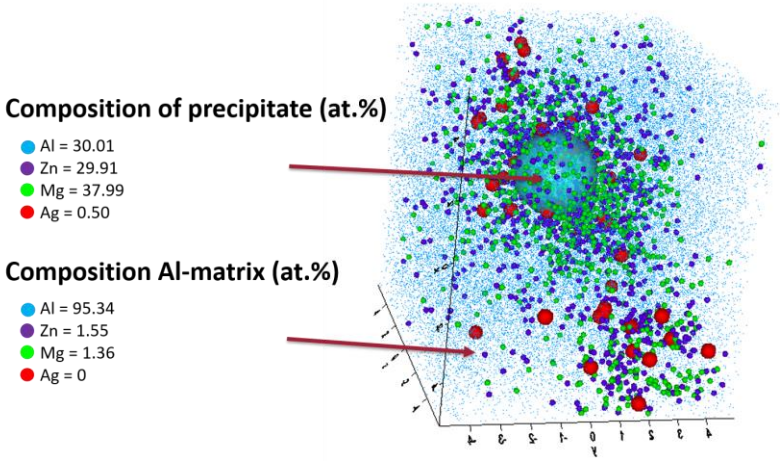

Assumes a constant field of evaporation

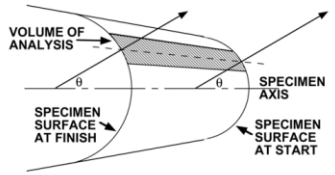

$$r_t = \frac{V}{k_f F}$$

r_t – radius of curvature V – apex voltage
k_f – geometric field factor F – evaporation field

Correlative PED & APT – sample preparation

Cut the edge by Ga⁺ ➡ **Lift-out a wedge** ➡ **Mount the wedge on Si half grid**

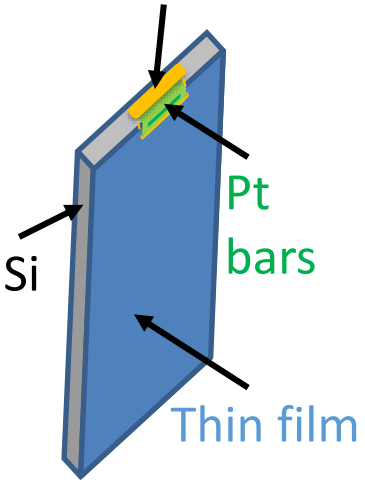

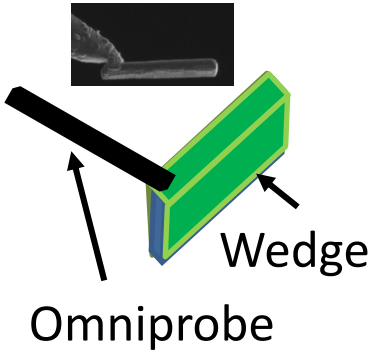

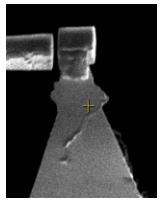

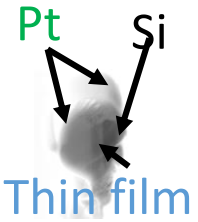

Si half grid

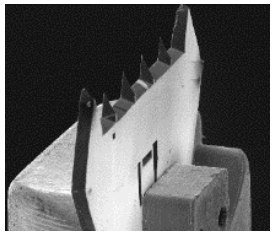

Sharpen tips by Ga⁺

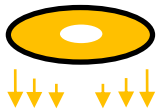

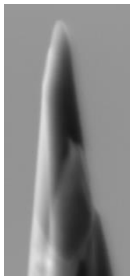

FIB

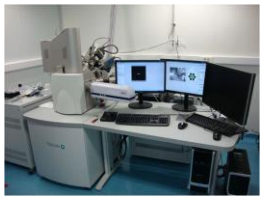

Tescan

Image tips in TEM

Hummingbird holder

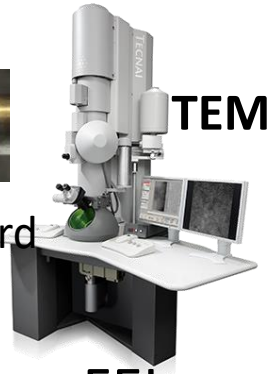

Evaporate tips in LEAP

Puck

LEAP

Cameca

*Zhou, X. et al. Sci. Rep. **6**, 34642; doi: 10.1038/srep34642 (2016)*

Correlative TEM & APT – Segregation to specific GBs

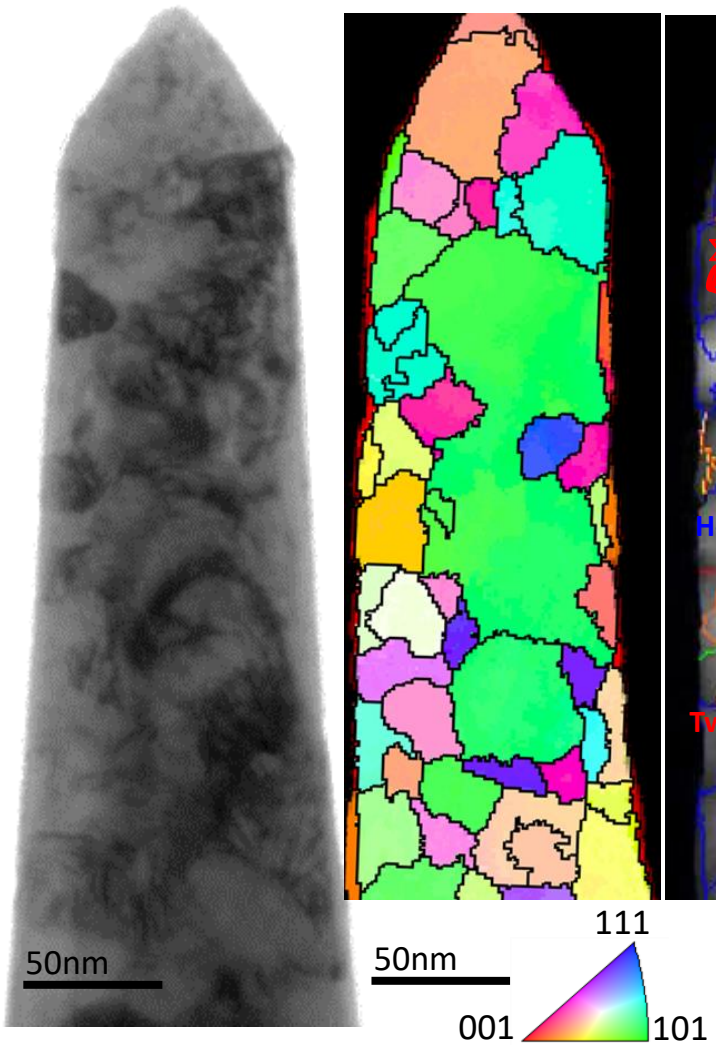

Zhou, X. et al. Sci. Rep. ***6****, 34642; doi: 10.1038/srep34642 (2016)*

Experimental Results of Cr Segregation to specific GBs

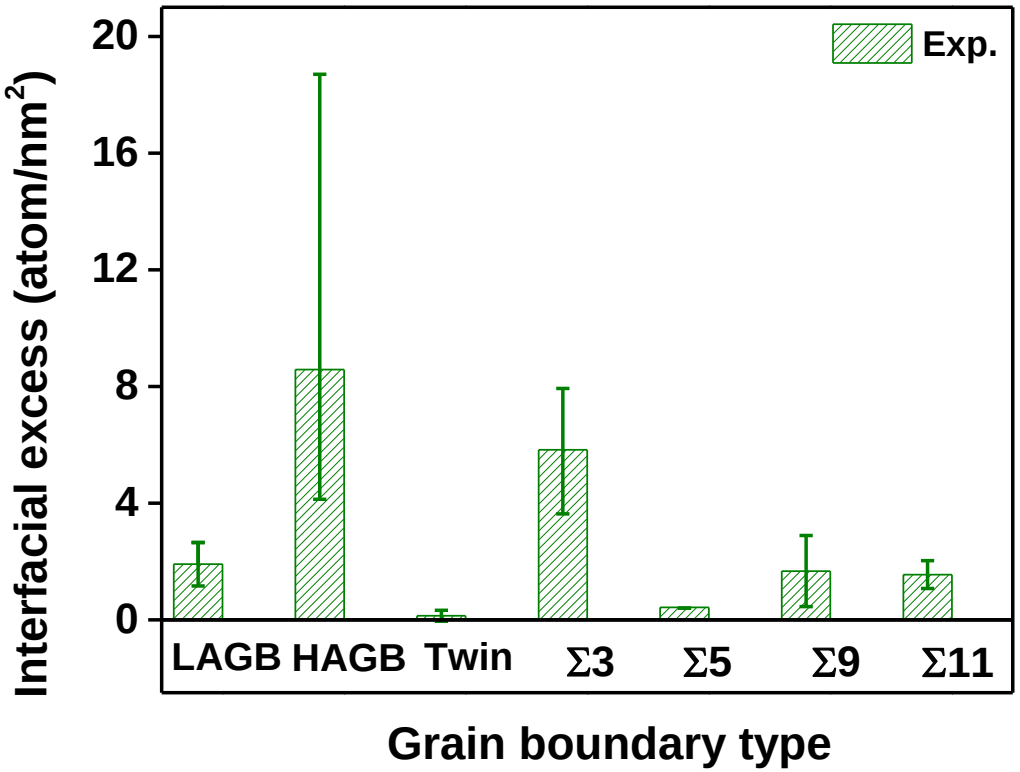

- Cr segregation is strongly related with GB types
- HAGBs appear to have both the largest Cr segregation and largest range
- **What is contributing to the range of values for the same mis-orientation?**

*Zhou, X. et al. Sci. Rep. **6**, 34642; doi: 10.1038/srep34642 (2016)*

Need to fully quantify the grain boundary character

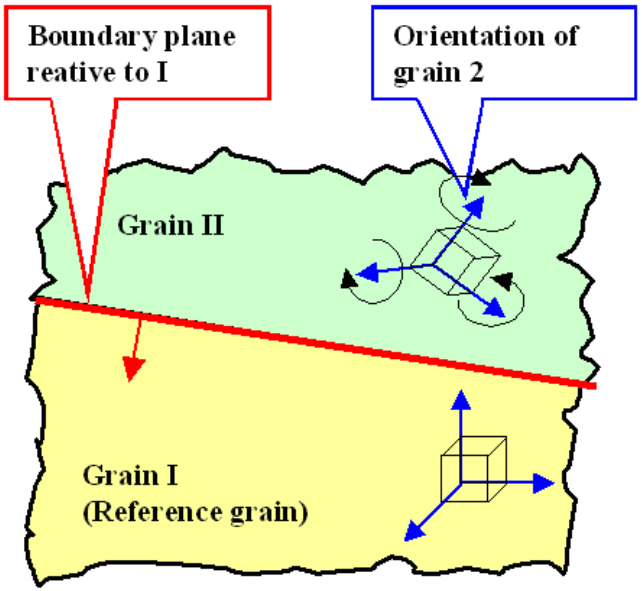

- Defining a grain boundary needs 5 parameters:
  - 3 for orientations related to adjacent grains
  - 2 for orientation GB plane inclination

http://www.tf.uni-kiel.de/matwis/amat/iss/kap_5/advanced/a5_3_1.html

GB Inclination:

Proof 1: Cross-section image

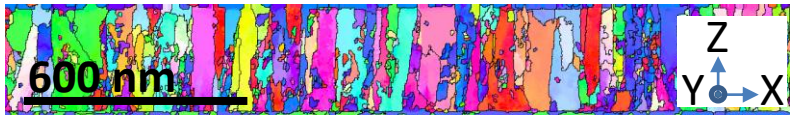

Proof 2: Measure the GB inclination

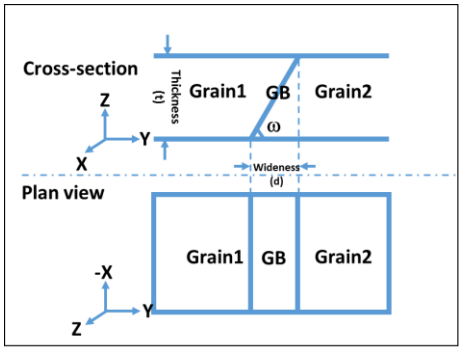

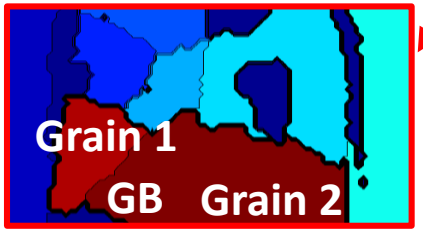

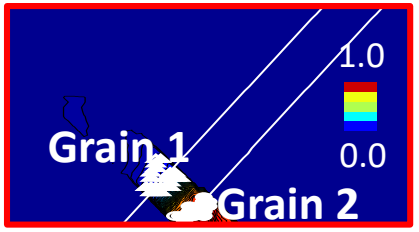

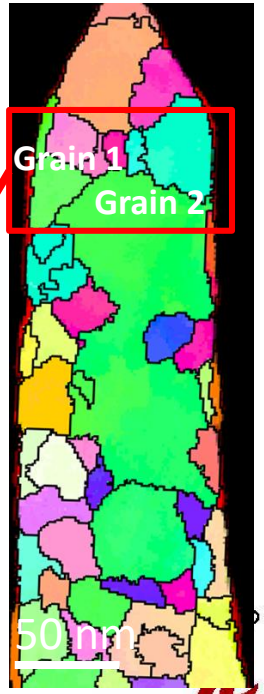

Quantifying the GB inclination

- Determine the GB plane projection (PED and/or planar assumption)
- Rotate the two lattices in each grain until a common (reference) plane is found
- The angle between the GB projection plane to the shared reference lattice plane defines the GB inclination

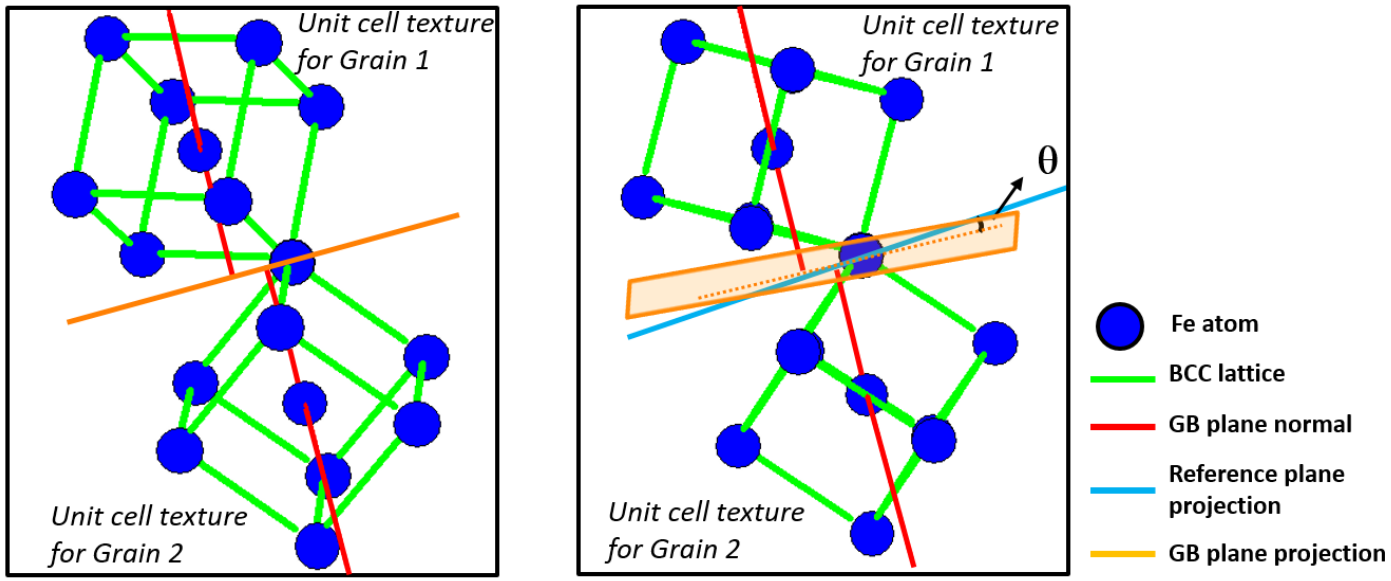

*Zhou, X. et al. Sci. Rep. **6**, 34642; doi: 10.1038/srep34642 (2016)*

Cr Segregation dependency on GB inclination

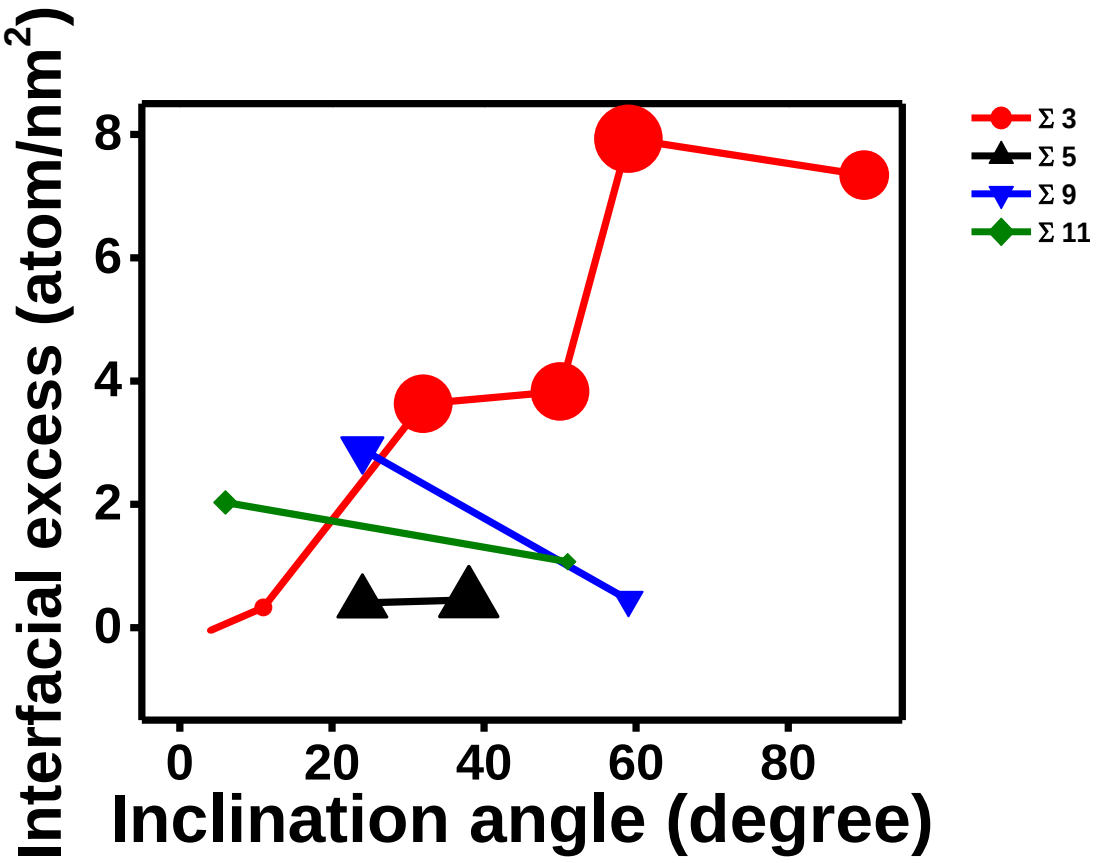

GB Simulation: *Hybrid Molecular Dynamics/Monte Carlo Calculation*

- Using the fully defined GB, equivalent GBs were simulated to determine solute behavior within the GBs
- A **hybrid MD/MC simulation*** was conducted in LAMMPS
- The segregated Fe(Cr) structure was obtained at a temperature of 300 K by using the Fe-Cr binary concentration dependent embedded atom model potential.

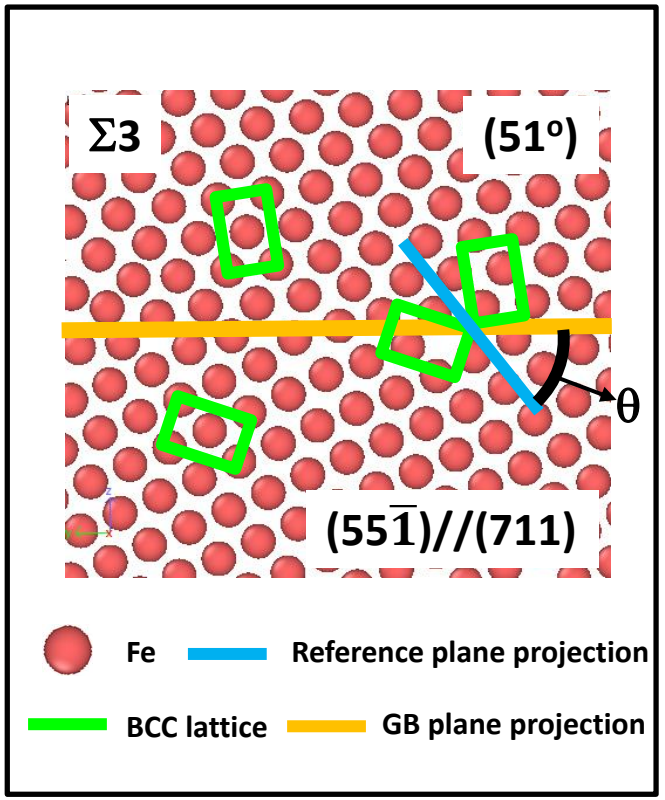

**Babak Sadigh, PRB, 2012*)

https://staff.aist.go.jp/h.ogawa/GBstudio/gbs3/GBs_PJ.html

Comparisons between experimental & simulated results

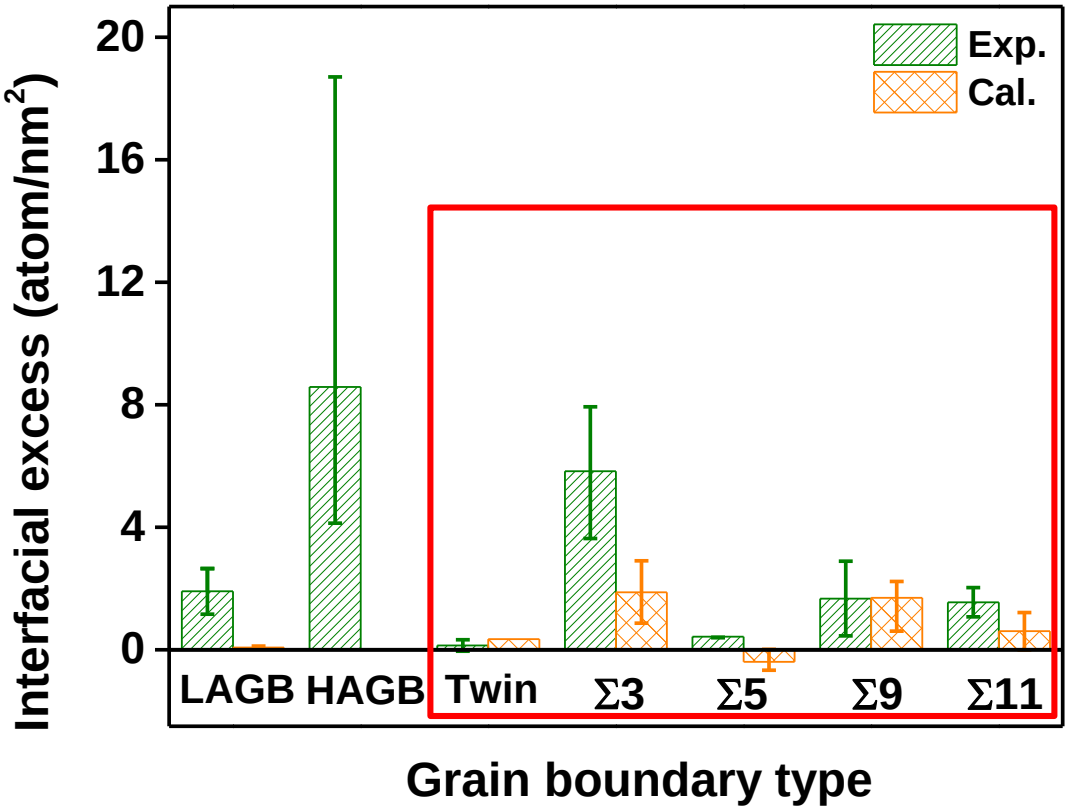

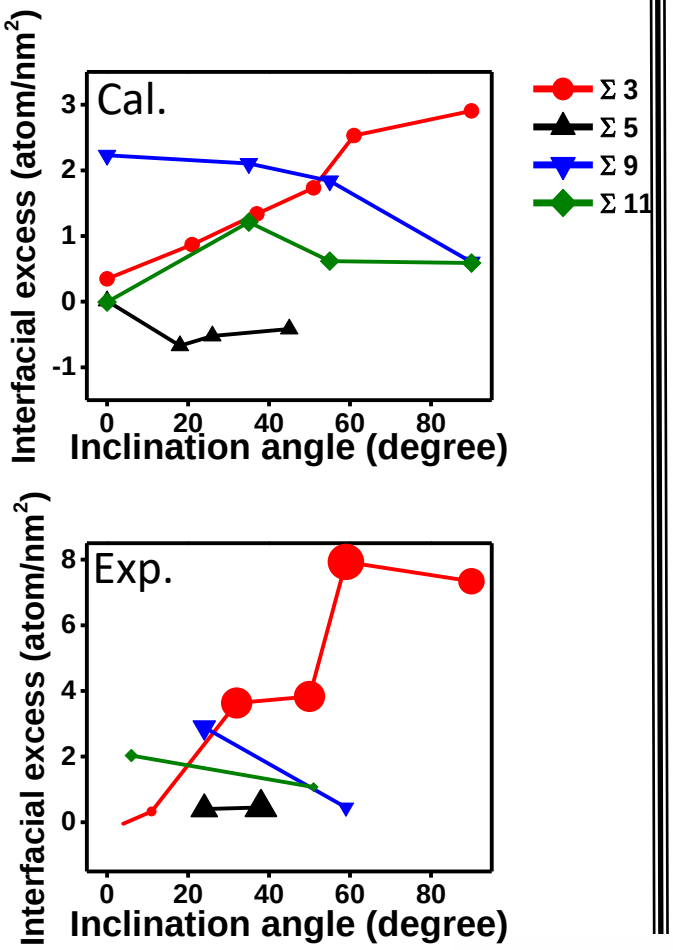

- Experimental IE values are similar to predicted values.

Zhou, X. et al. Sci. Rep. ***6****, 34642; doi: 10.1038/srep34642 (2016)*

Comparisons between experimental & simulated results

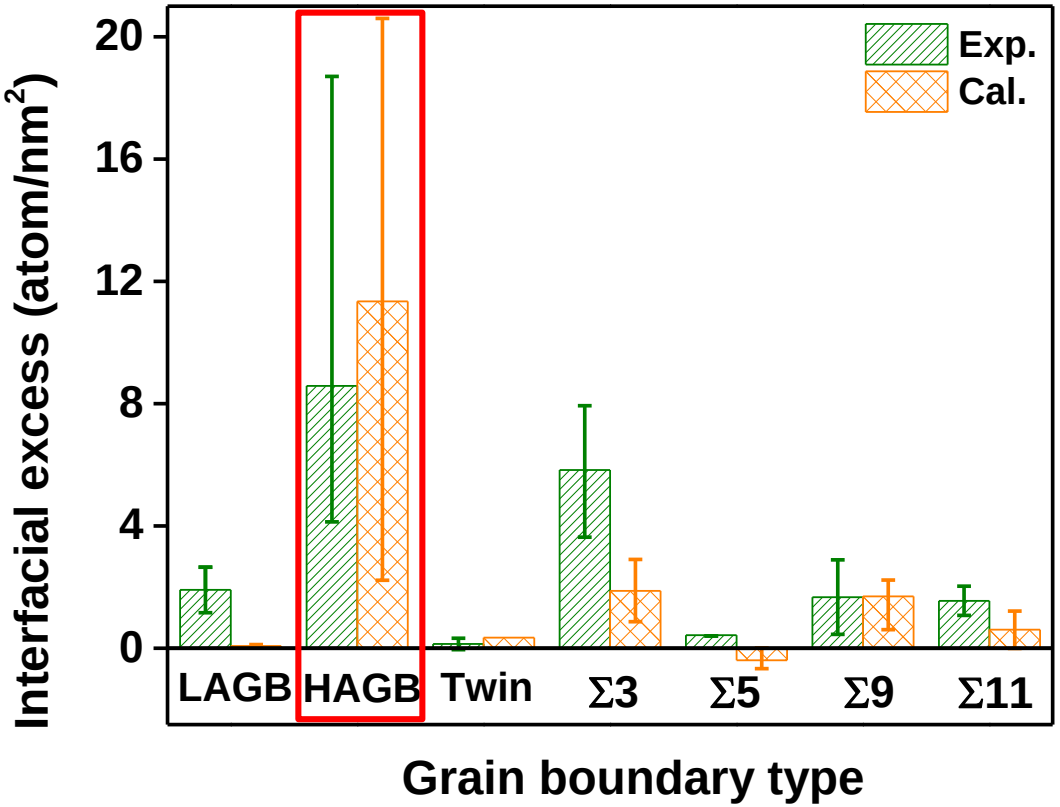

Clustering Analysis

Exp.

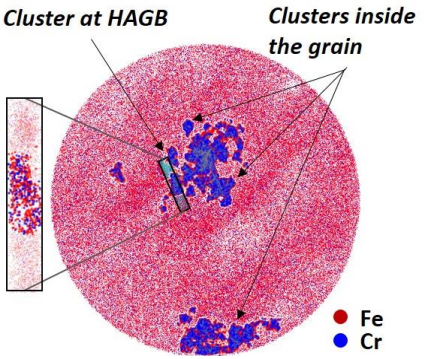

Cal.*

Poly-Crystal

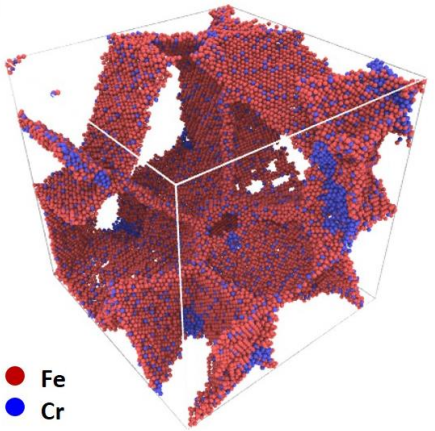

- Experimental IE values are similar to predicted values.
- Clusters form at high angle grain boundaries.

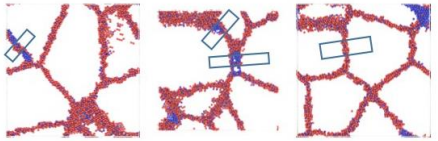

Comparison of GB behavior: specific types

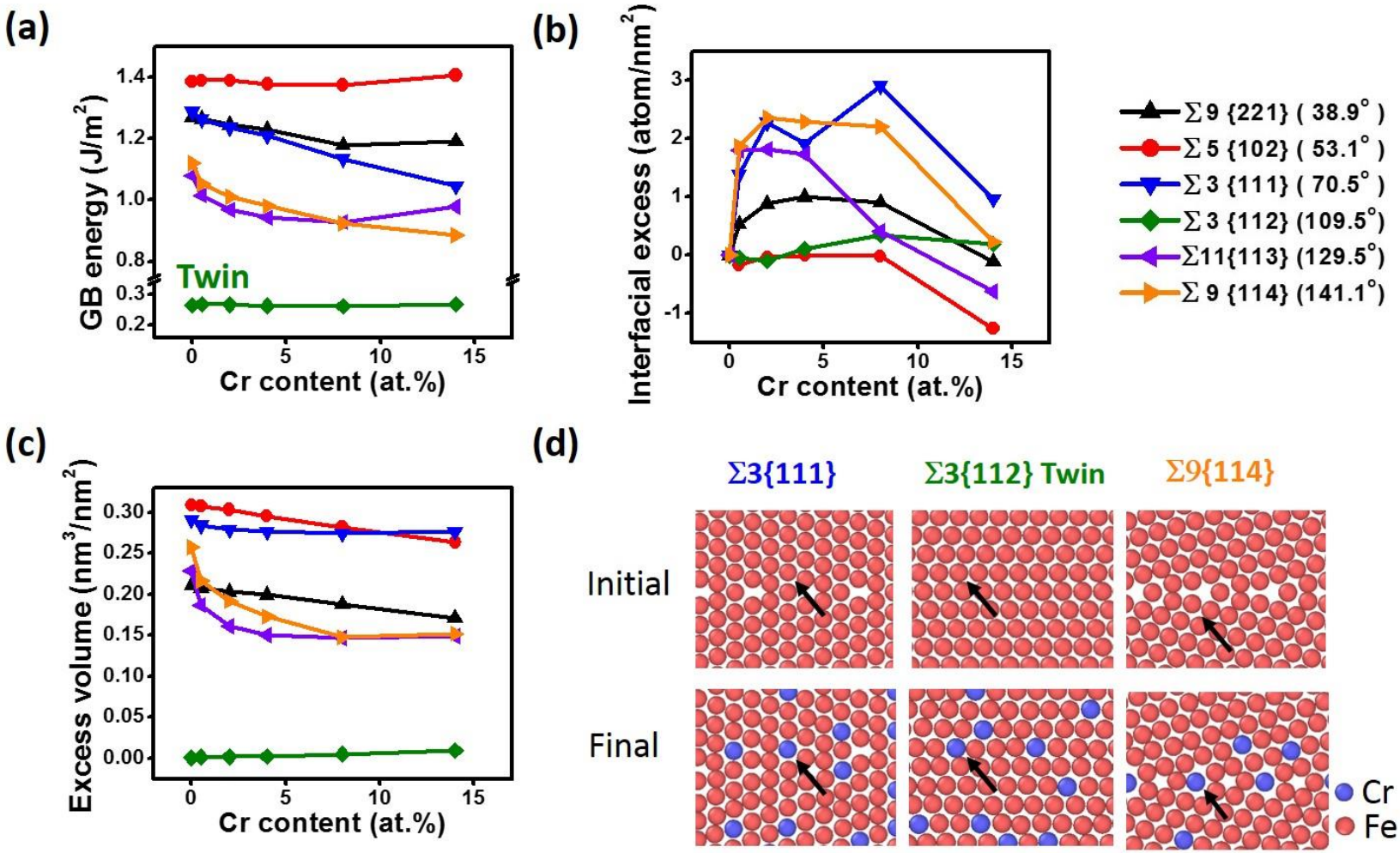

- In general, GB energy trended the excess volume behavior

(a) Calculated grain boundary energies **(b)** Interfacial excess **(c)** Excess volume for various Cr contents **(d)** Simulated atomic configuration for Σ-GBs with and without Cr segregation. The arrows direct to local lattice locations where relaxation from the initial to final states were tracked.

Zhou, X. et al. Sci. Rep. ***6****, 34642; doi: 10.1038/srep34642 (2016)*

Apply *in situ* annealing to drive the solutes towards equilibrium

Grain Size Evolution

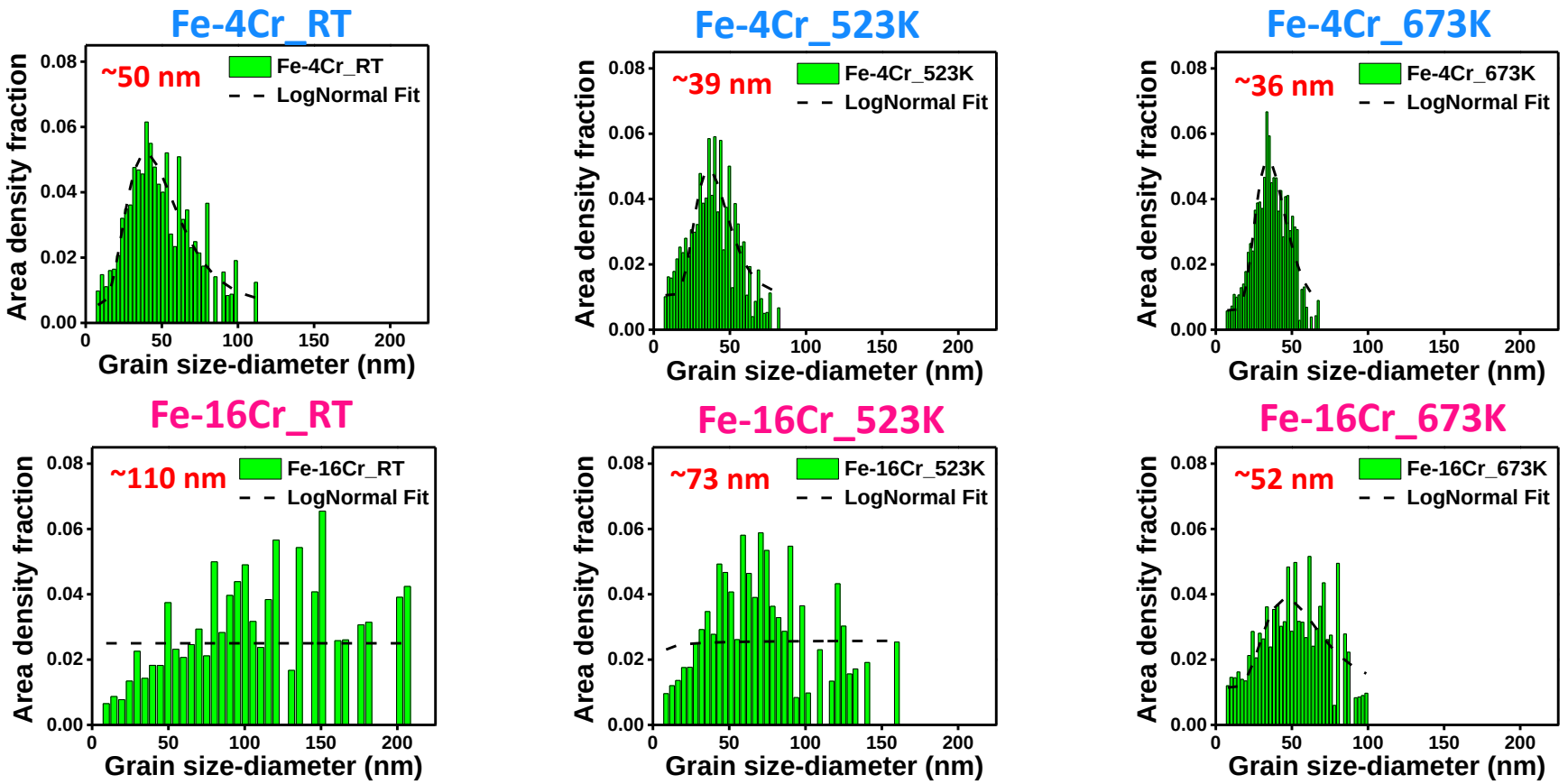

- When the temperature was increased, the grain sizes were reduced and the distribution was tightened up.

Grain Texture Evolution - <101>

Fe-4Cr_RT

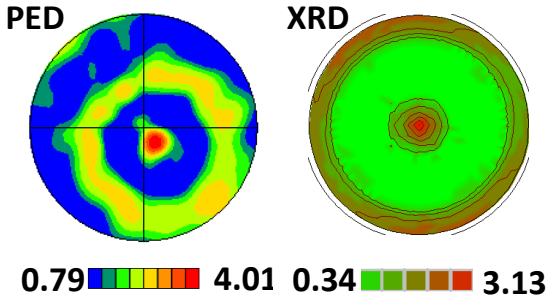

Fe-4Cr_523K

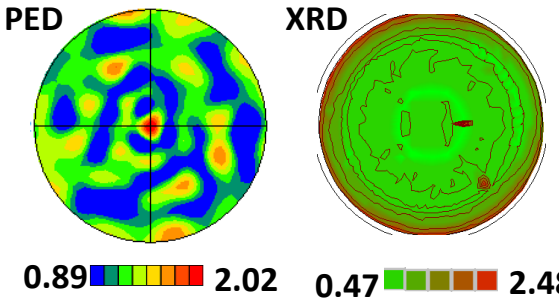

Fe-4Cr_673K

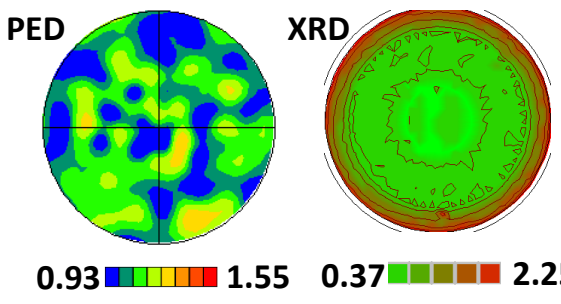

Fe-16Cr_RT

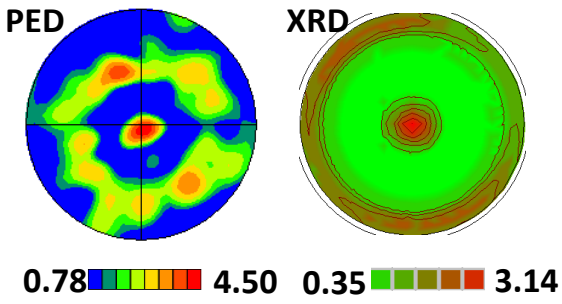

Fe-16Cr_523K

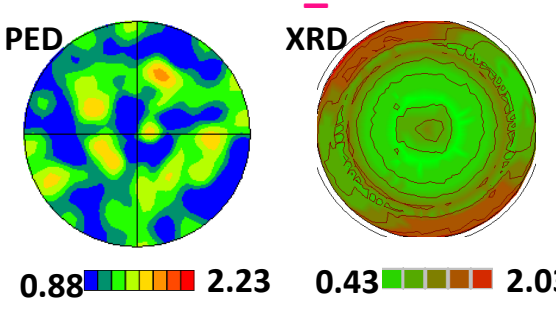

Fe-16Cr_673K

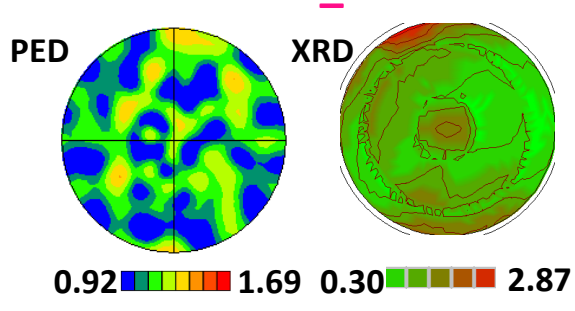

- When the temperature was increased, both Fe-4Cr and Fe-16Cr films gradually lost the preferred <101> texture.

Grain boundary composition

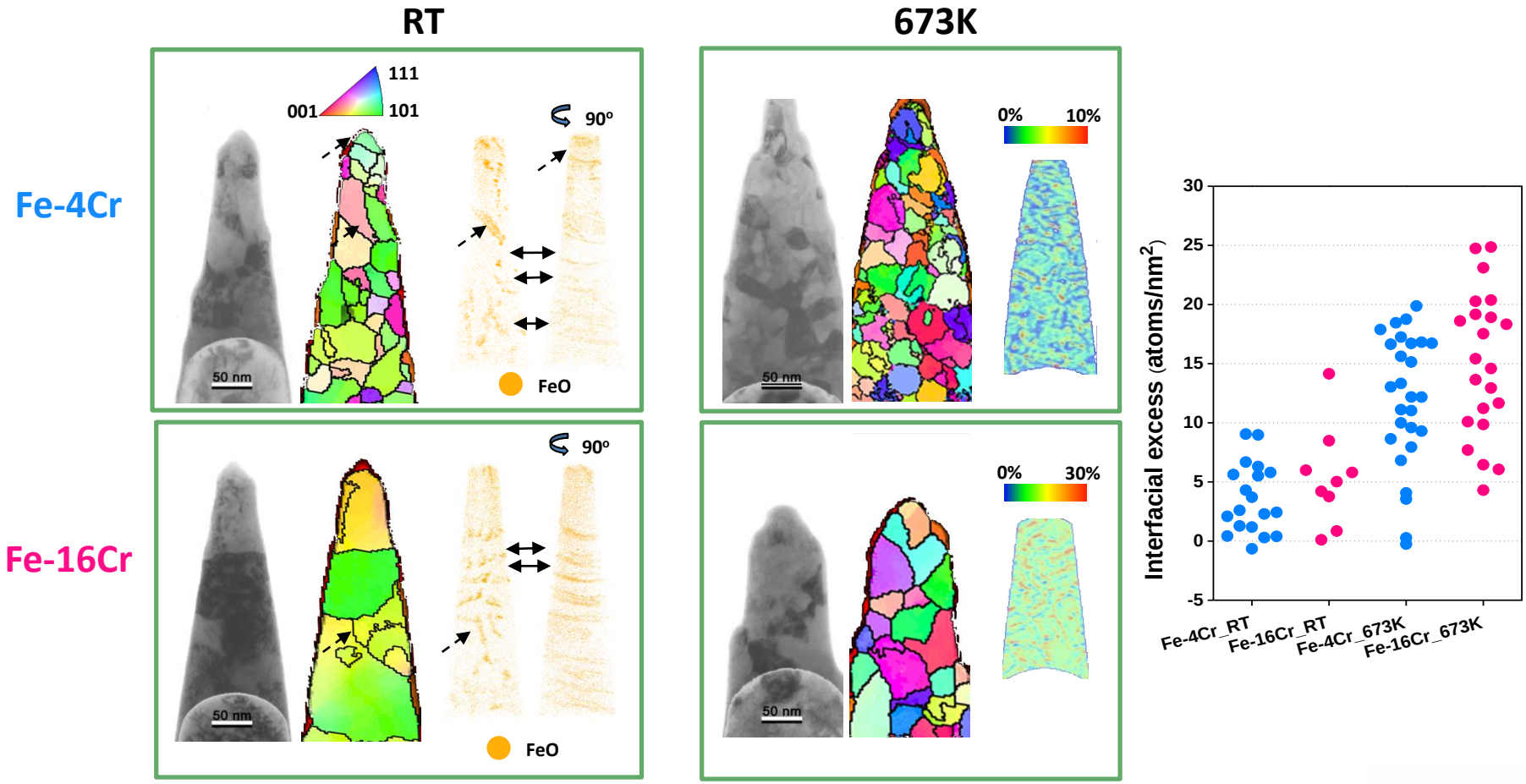

Specificity in Grain Boundary Partitioning

PED: GB type

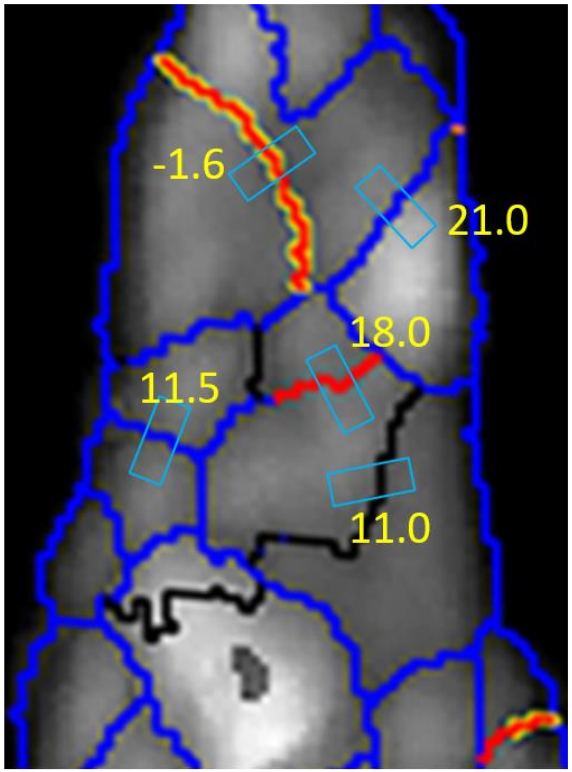

Number: IE(atoms/nm^2)

50 nm

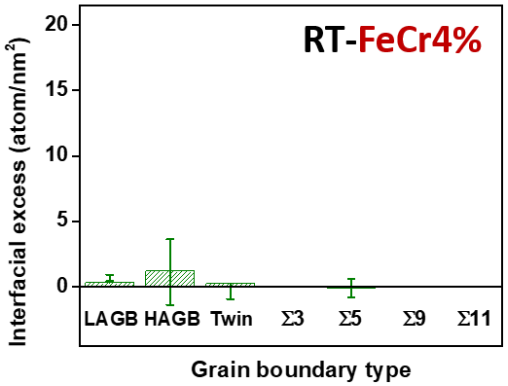

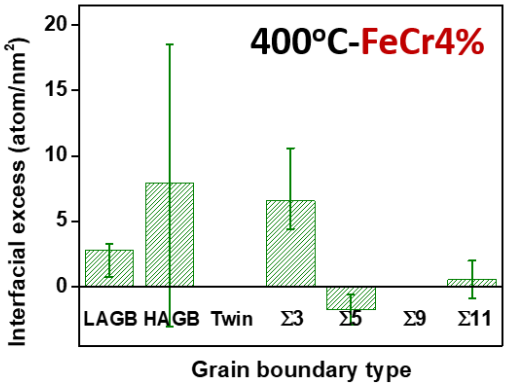

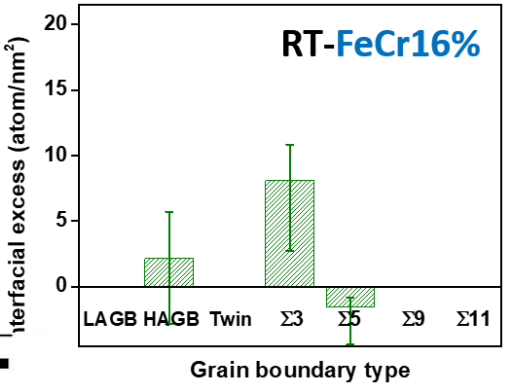

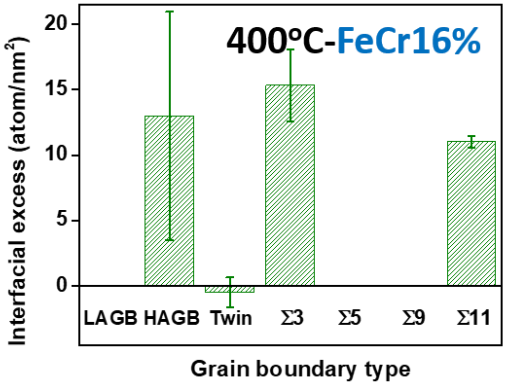

Spinodal Decomposition

2D contour plot from the APT data and GB map from PED data (FeCr16% 400°C)

APT: Composition(Cr) Density **PED:** GB type

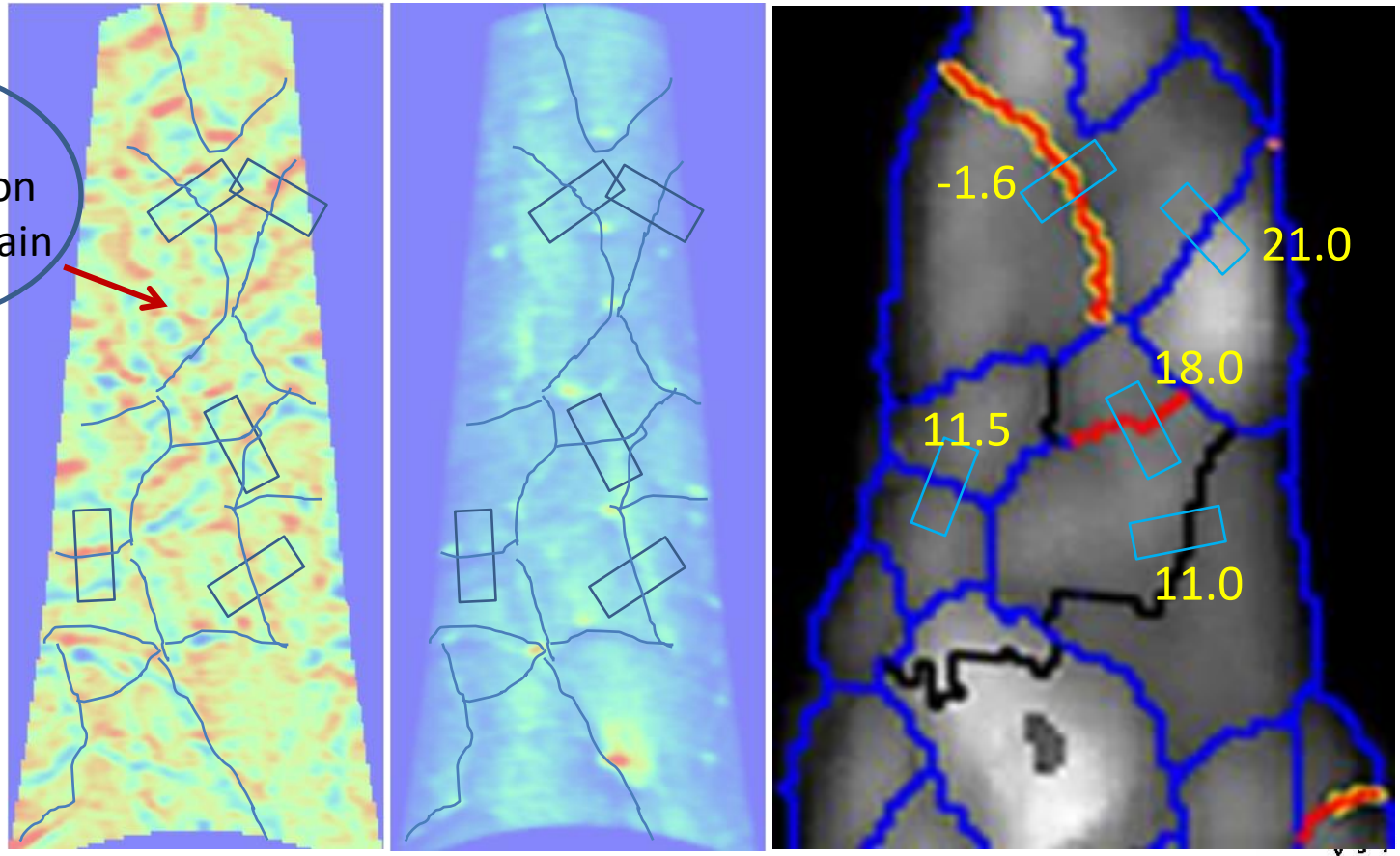

Spinodol Decomposition

APT analysis

Fe-4Cr_673K

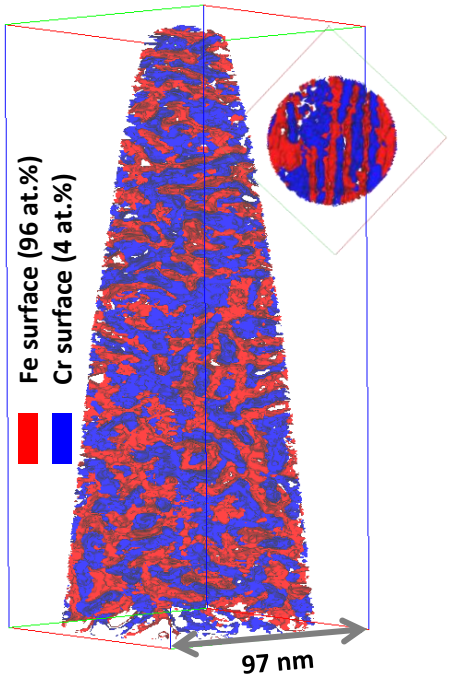

Fe-16Cr_673K

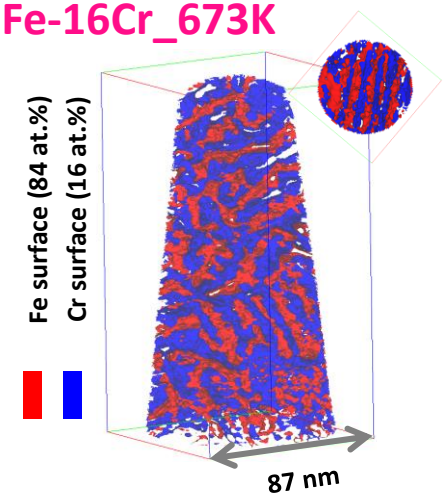

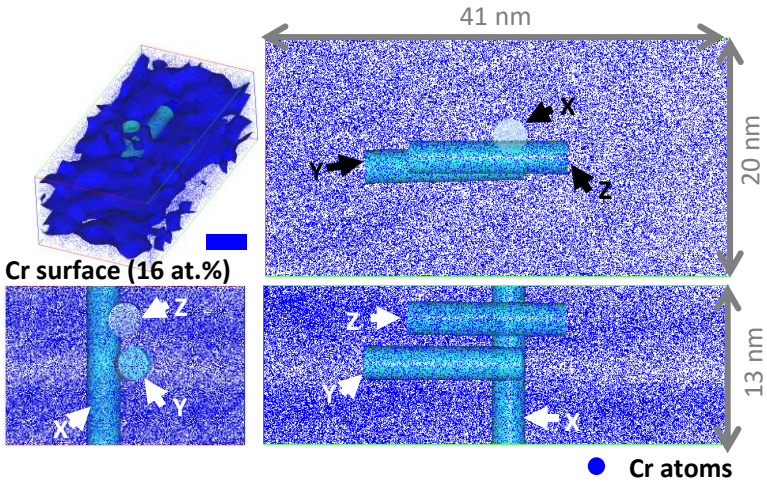

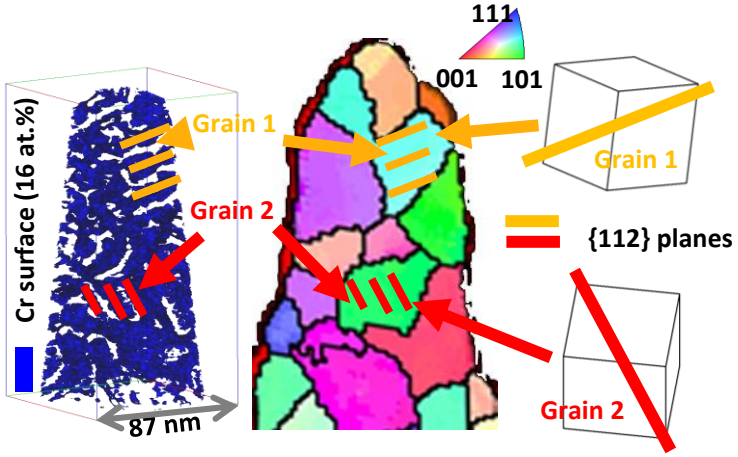

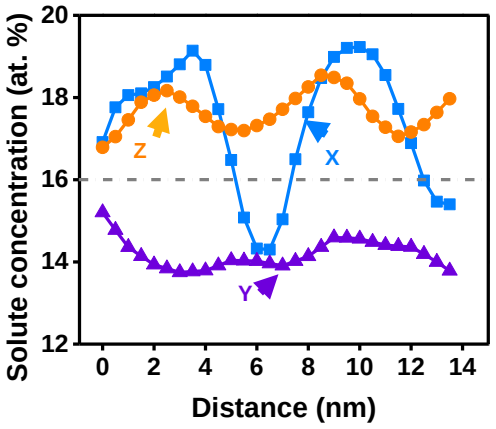

In situ annealing and PED correlation

- Two alloy targets, **FeCr-4%** and **FeCr-16%**, were existed
- 50 nm thick Fe(Cr) alloy films were deposited on the DensSolution chip.

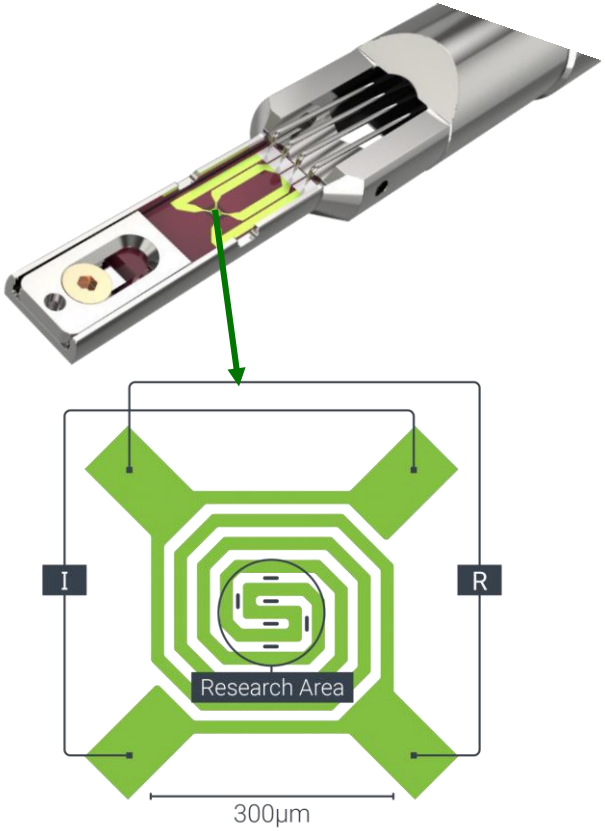

Heat treatment parameters:

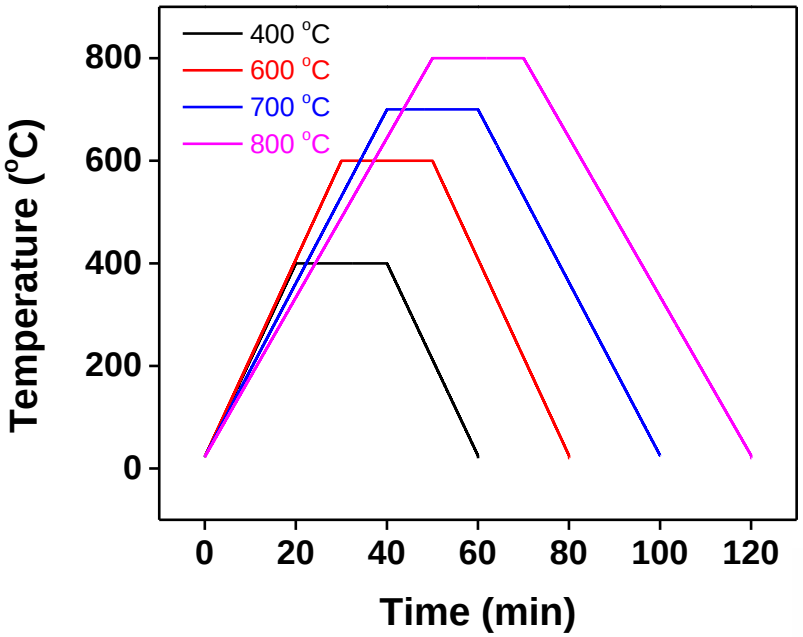

- Up to 1200°C at 10^6 °C/s
- Very thermally stable

http://denssolutions.com/products/heating/

Grain size verses Annealing temperature

17%Cr

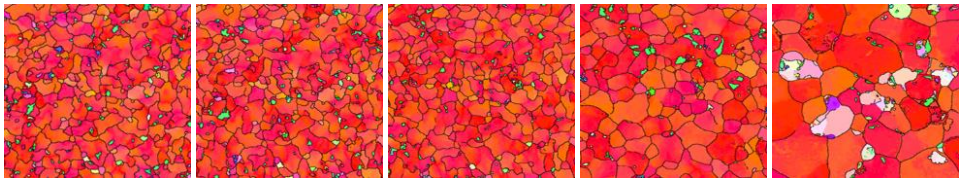

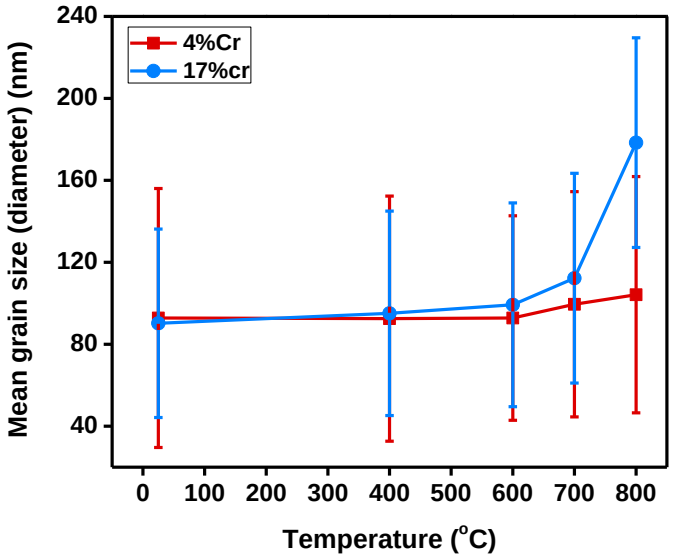

600 nm

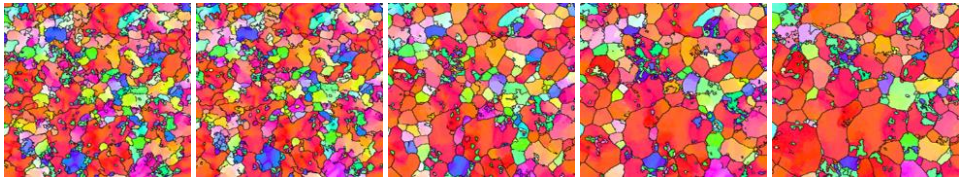

4%Cr

T

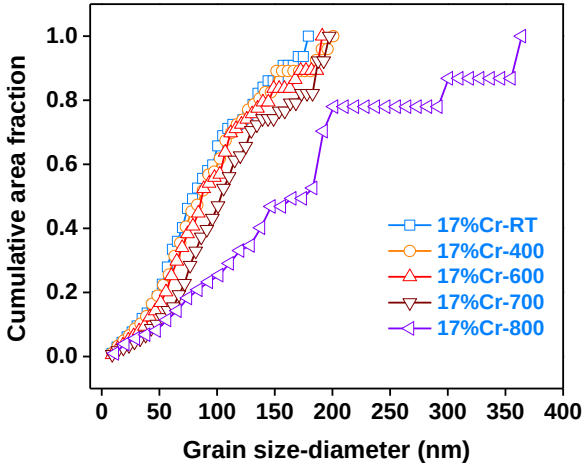

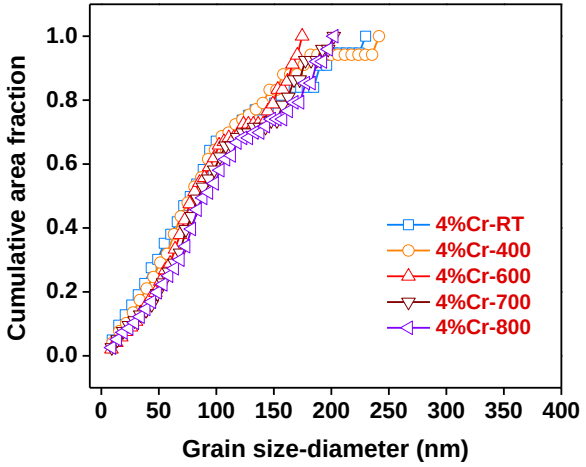

- For FeCr17%, obvious grain growth was observed at ~700°C
- For FeCr4%, no obvious grain growth was observed;
- @ 50 nm, {100} is the lowest energy surface (magnetic contribution)*

*M. Ropo, et al. PRB **76** (2007) 220401(R).

Cross-correlative: PED + EDS …*Oxidation!*

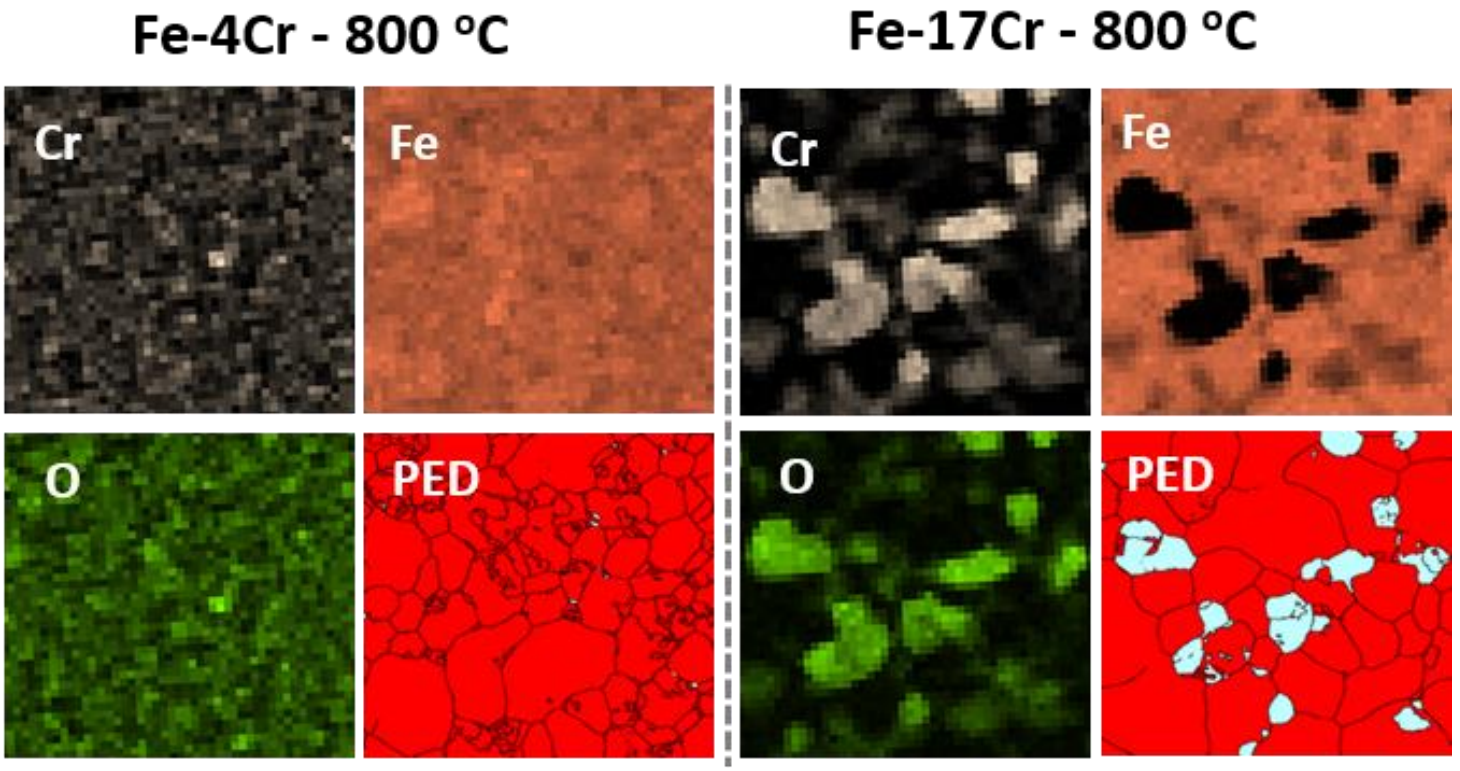

Ellingham diagram of Fe and Cr

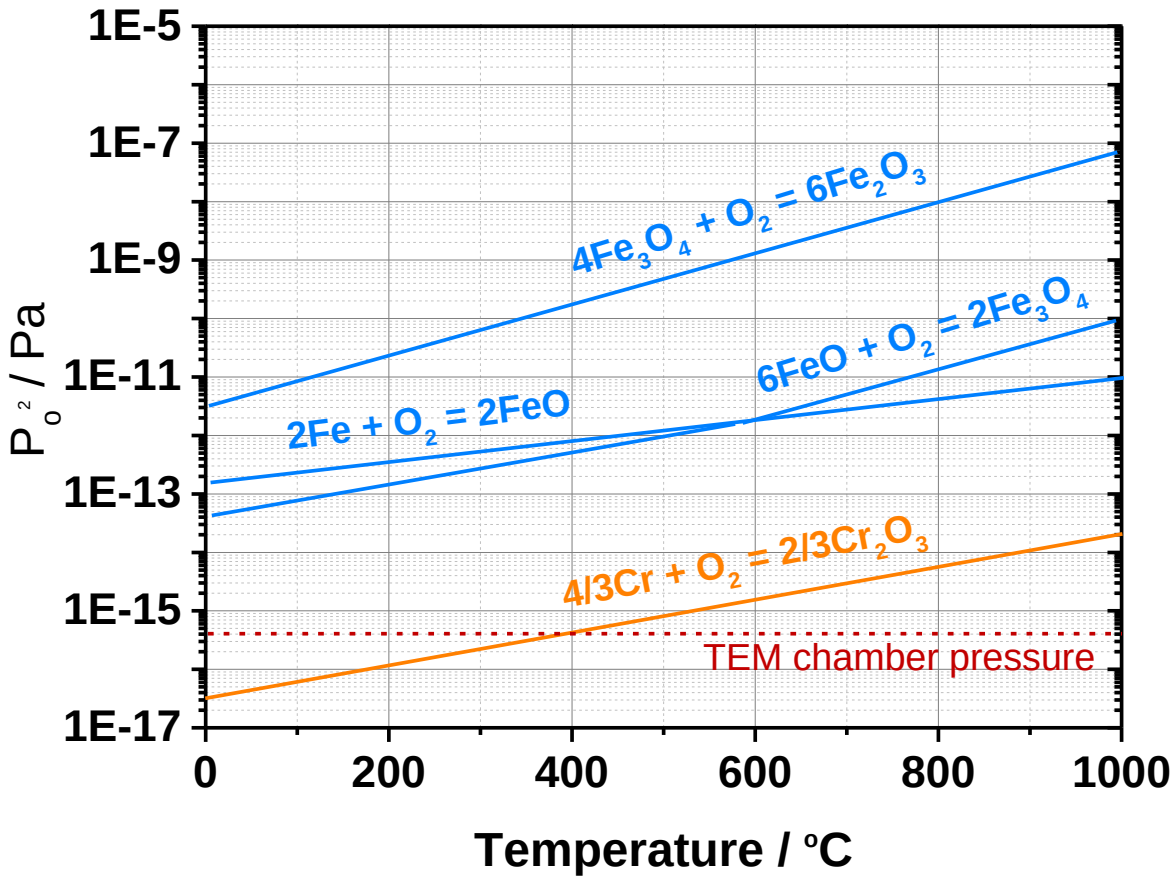

STEM-HAADF: 800°C

Fe-4Cr

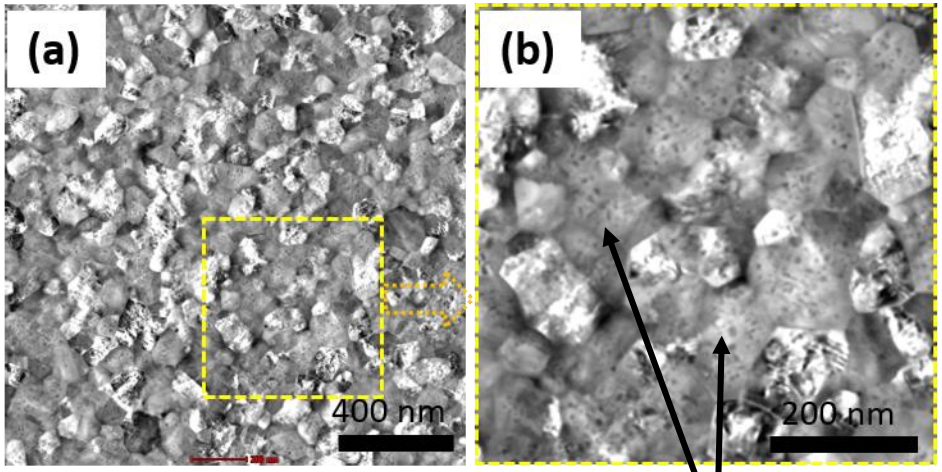

Fe-17Cr

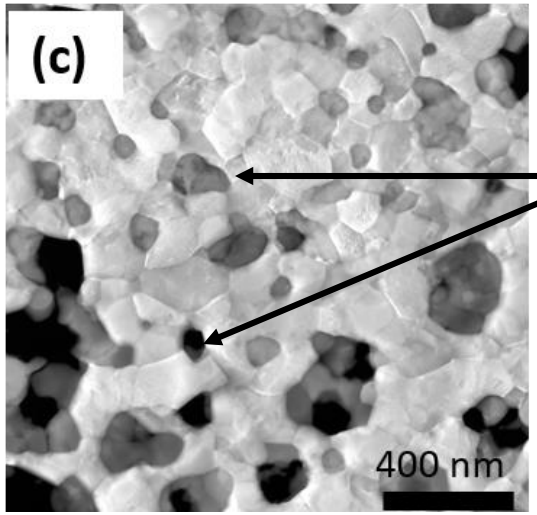

Note the small oxide features in the Fe-4Cr sample

Large, granular oxide grains

Fe-17Cr @ 700°C/ 1hr

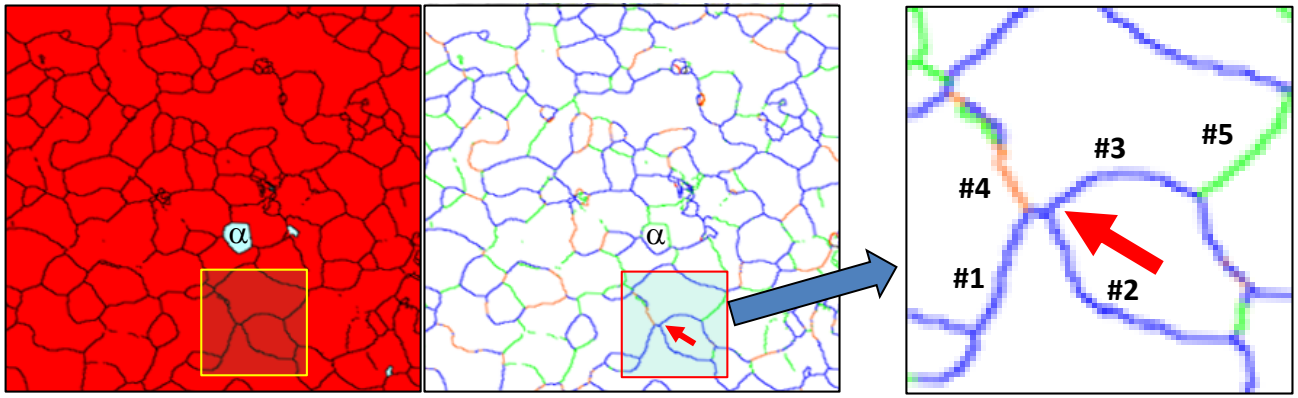

Fe-17Cr @ 800°C / 1 hr

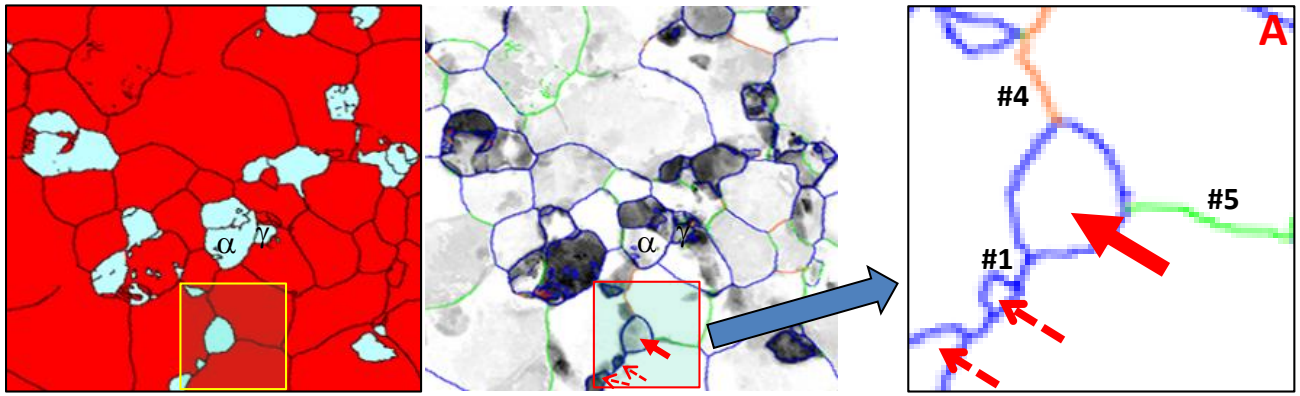

Fe BCC

Cr_2O_3

LAGB

HAGB

Σ5

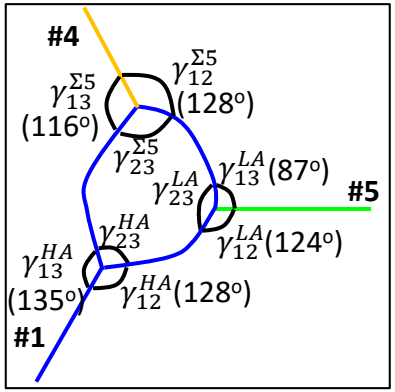

- Oxide precipitating and growing out of HAGBs (and preservation of LAGB; Σ5)

Application of PED to Deformation Investigations

Early Reports of Cryogenic Grain Growth

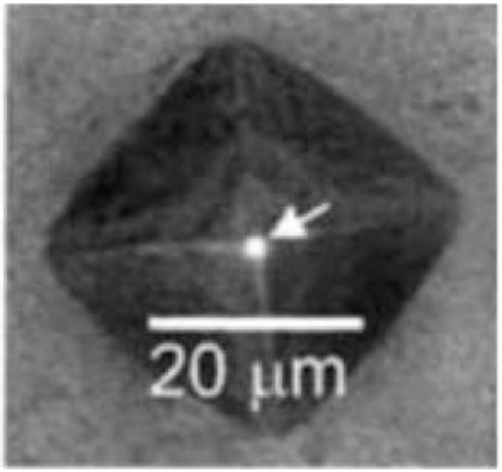

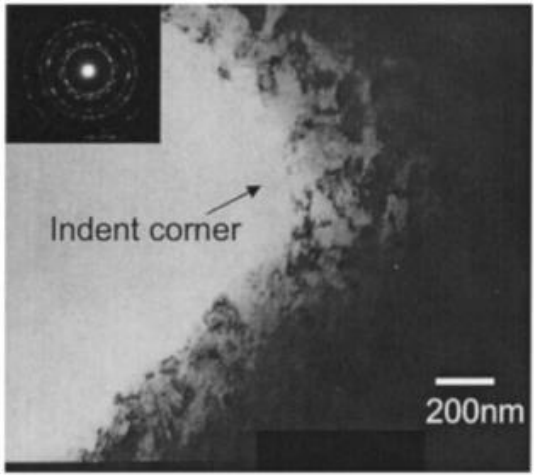

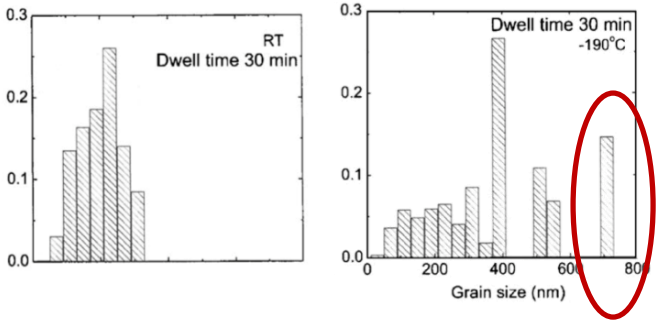

Taken from Zhang *et al., APL*, **87** (2005) 6192

Zhang, Weertman, and Eastman (APL 2005) reported grain growth in nanocrystalline Cu films under indentation at 77 K.

- ✓ When the temperature is sufficient and a driving force is present, it is understood why the system exhibits growth.
- ✓In their report, where *mobility* is significantly hindered, the kinetics of grain growth are poorly understood.

A Quick Primer on Grain Growth

Grain growth occurs via grain boundary migration – typically a product of two factors

$$v = P * m$$

Driving Force, P

-Curvature (~1/r)
- Stored deformation energy
- Grain boundary energy
- Surface energy
- Elastic energy
- Chemical/thermal gradient

Mobility

The means for atoms to migrate to reduce the applied driving force.

Cryogenic Indentation

Untwinned and nanotwinned Cu films were indented using a Vickers indentation tip at a load of 55g while submerged in liquid Nitrogen for 600 seconds.

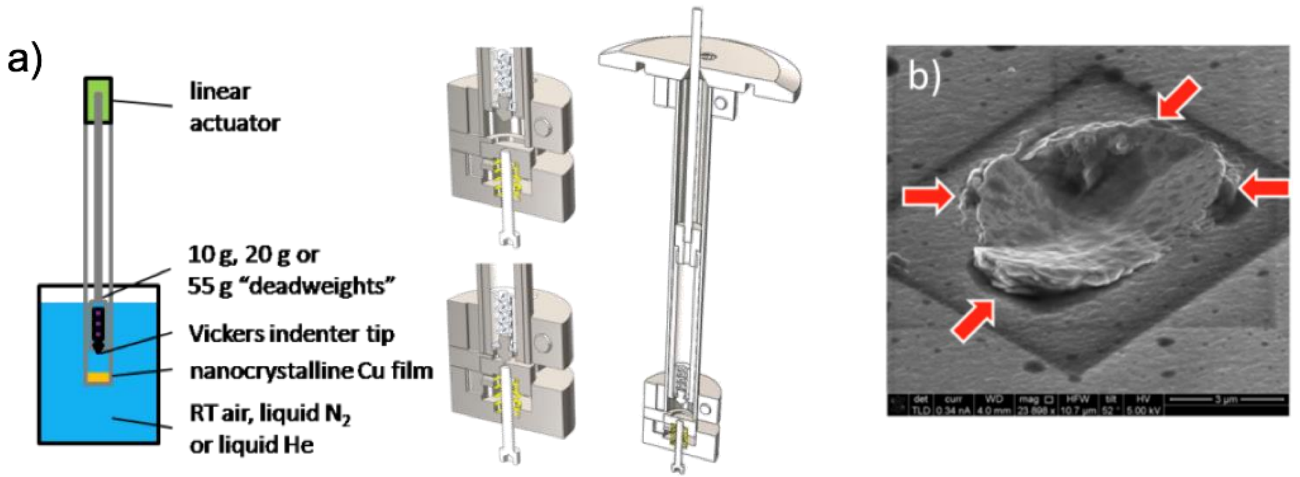

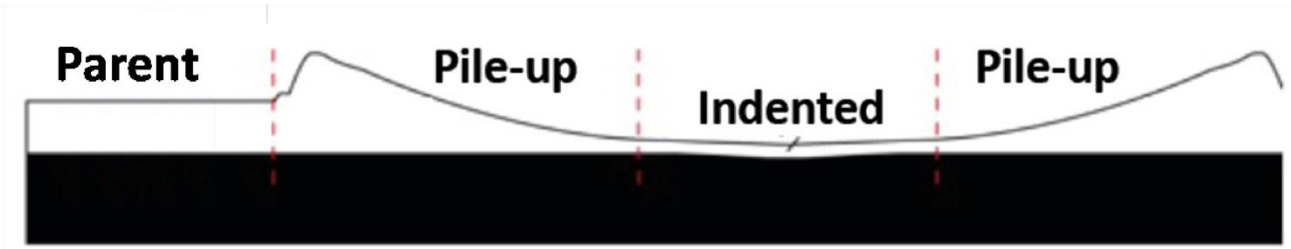

Brons, et al. *Scripta Materilia*, **68** (2013) 781-784

PLD of Nanocrystalline films

(with and without a high density of twins)

A series of nanostructured films Cu films with and without a high density of twin boundaries were fabricated by Pulsed Laser Deposition (PLD) processes.

- <111> nanocrystalline (nanostructured) Cu films with **no twins (NS)**

-Two fiber orientations <111> and <100> with a high density of **twins (NT).**

- Orientation change achieved by line-of-site of substrate to target; twin formation promoted by changing substrate temperature during growth

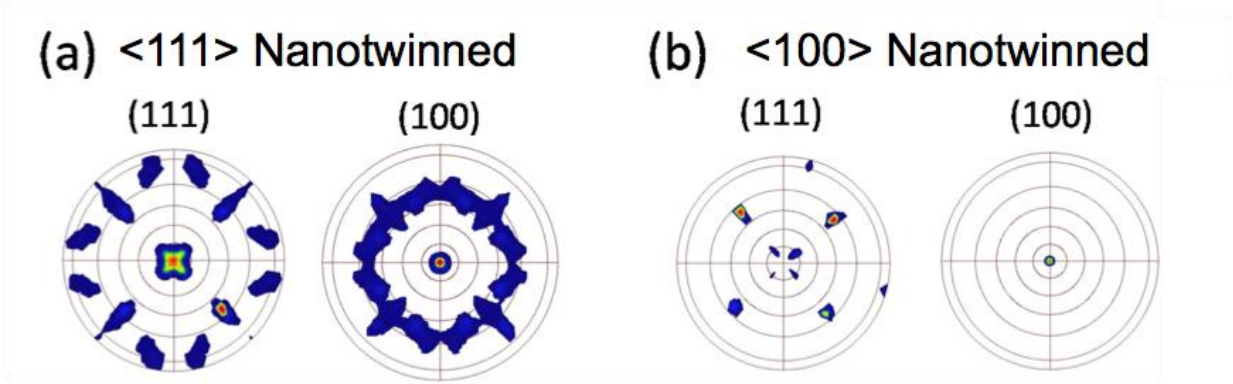

Brons, et al. *Materials Science and Eng. A 2013*

Microstructure of as-deposited films

Nanostructured Cu | *<100> Nanotwinned Cu* | *<111> Nanotwinned Cu*

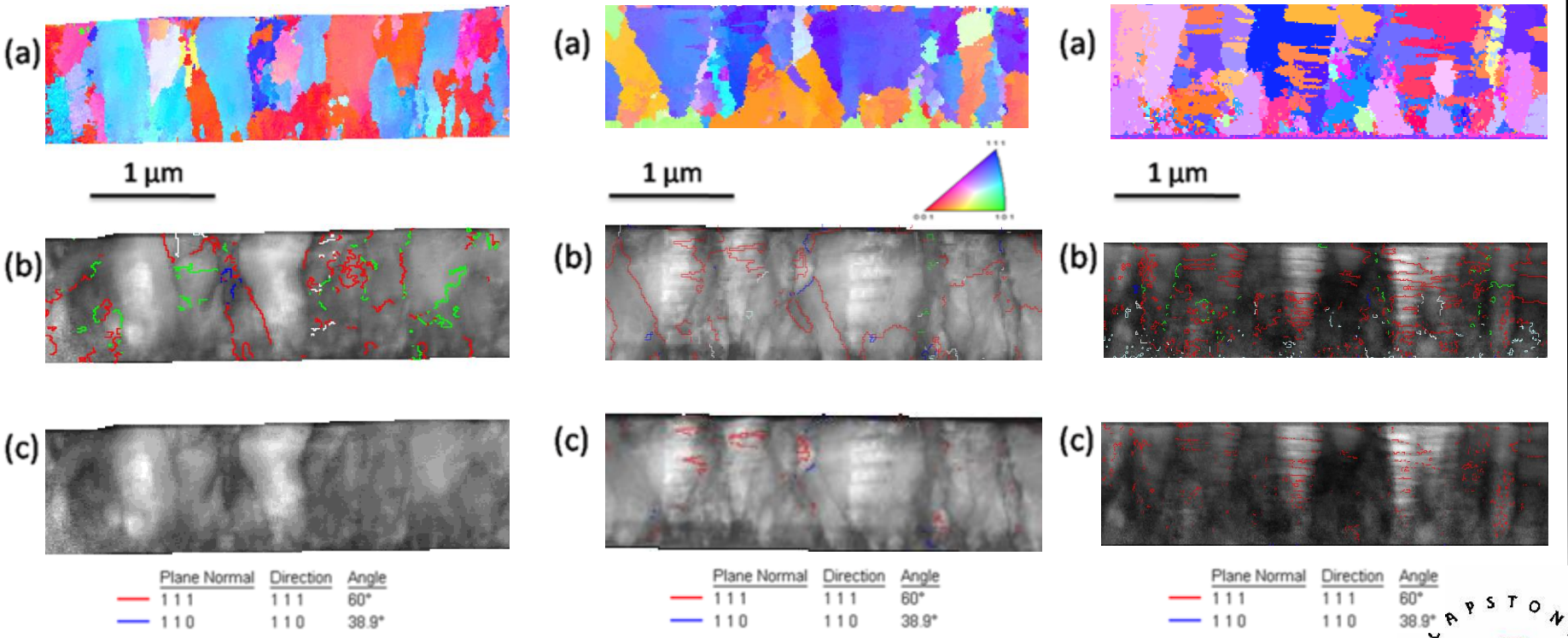

Twins plotted in (c)

Sigma: 3 5 7 9 11

Brons, et al. *Materials Science and Eng. A 2013*

Nanostructured Cu Indent

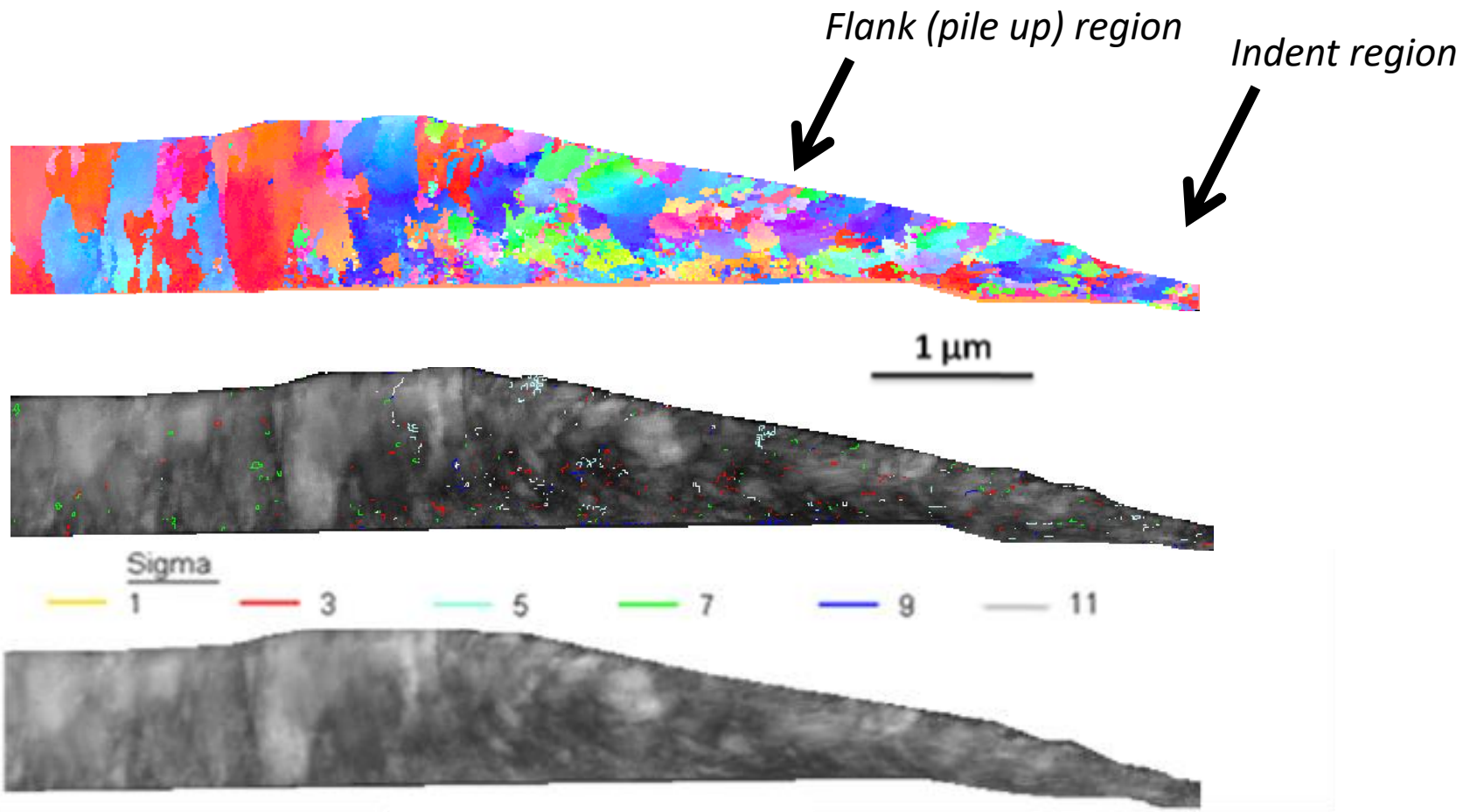

Grain distortion occurs in the flank of the indent - along with low angle boundary formation. No evidence of grain growth.

Brons, et al. *Materials Science and Eng. A 2013*

When Twin Boundaries are present, grain growth is observed

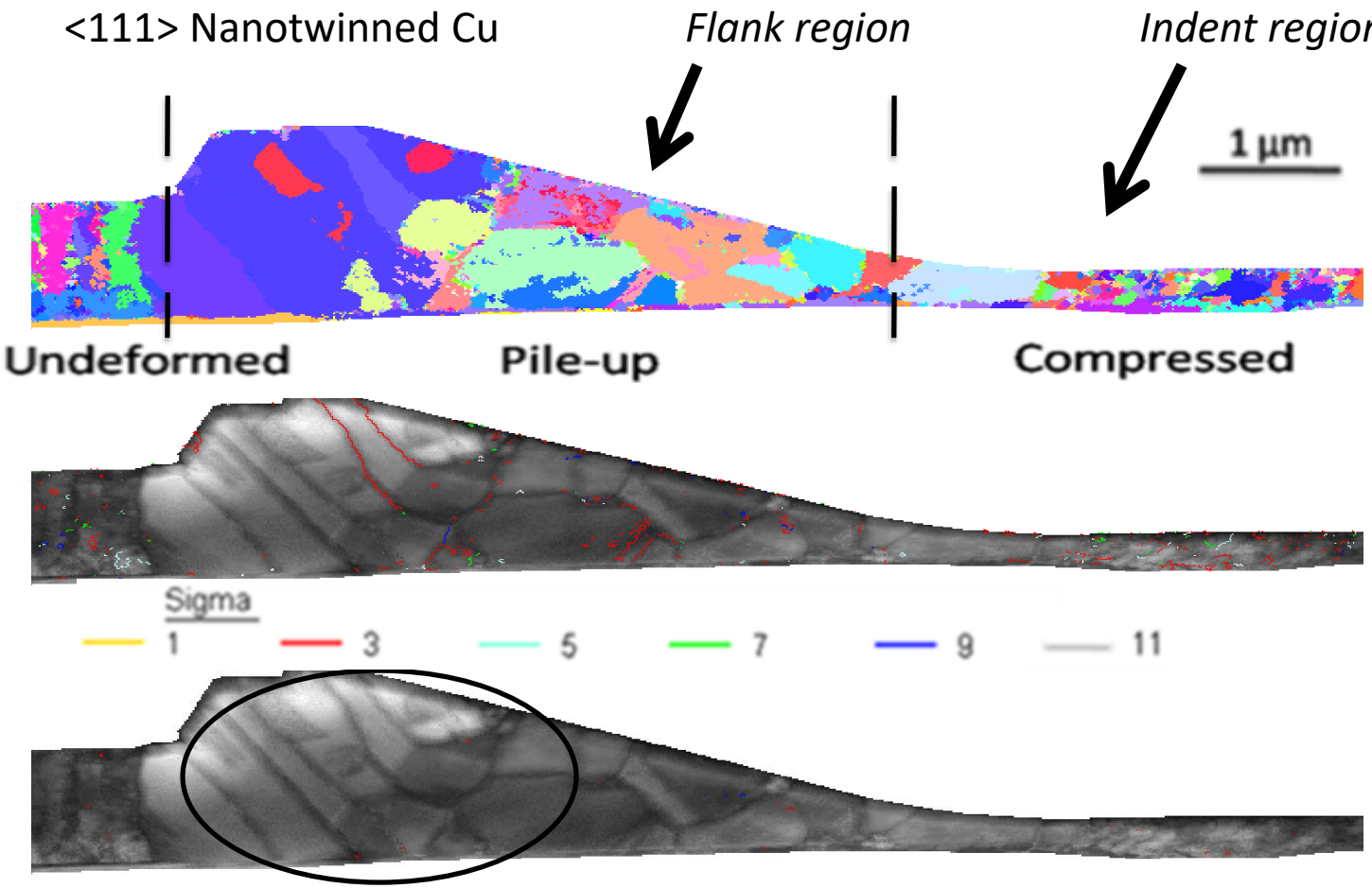

Grain growth evident in flank region

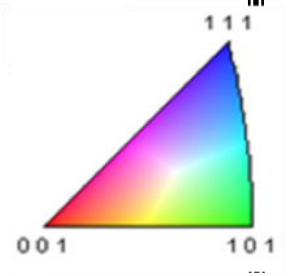

No twin boundaries detected, more to come

Brons, et al. *Materials Science and Eng. A 2013*

When Twin Boundaries are present, grain growth is observed

<100> Nanotwinned Cu

Flank (pile up) region

Indent region

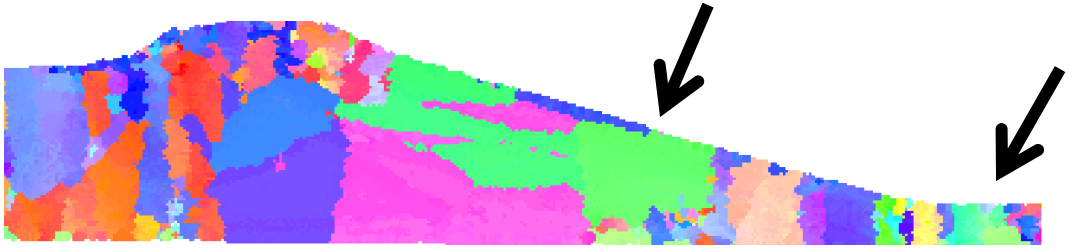

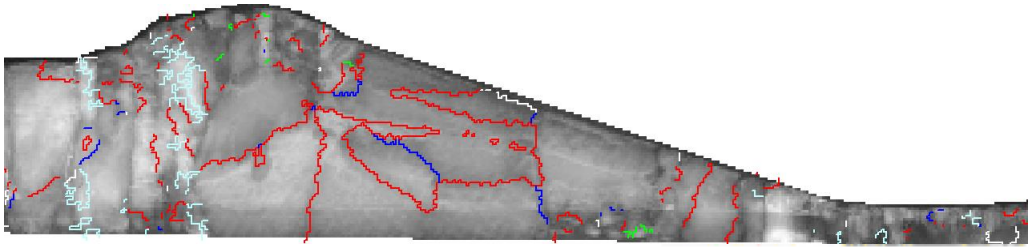

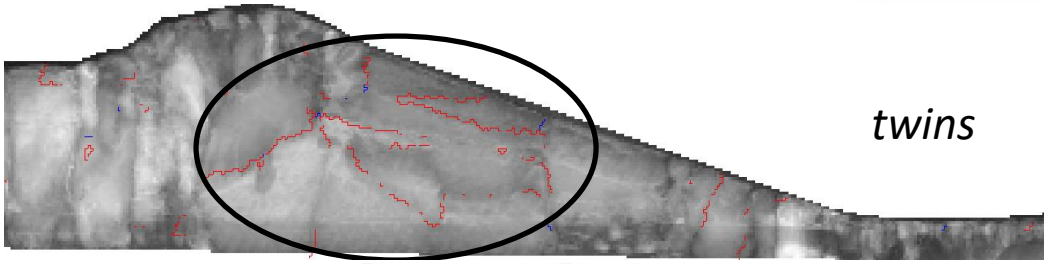

twins

Plane Normal	Direction	Angle
1 1 1	1 1 1	60°
1 1 0	1 1 0	38.9°

Grain growth evident in flank region

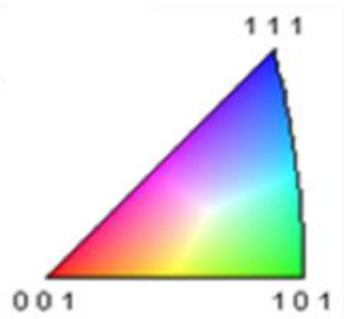

Brons, et al. *Materials Science and Eng. A 2013*

Analyzing the Grain Size Evolution

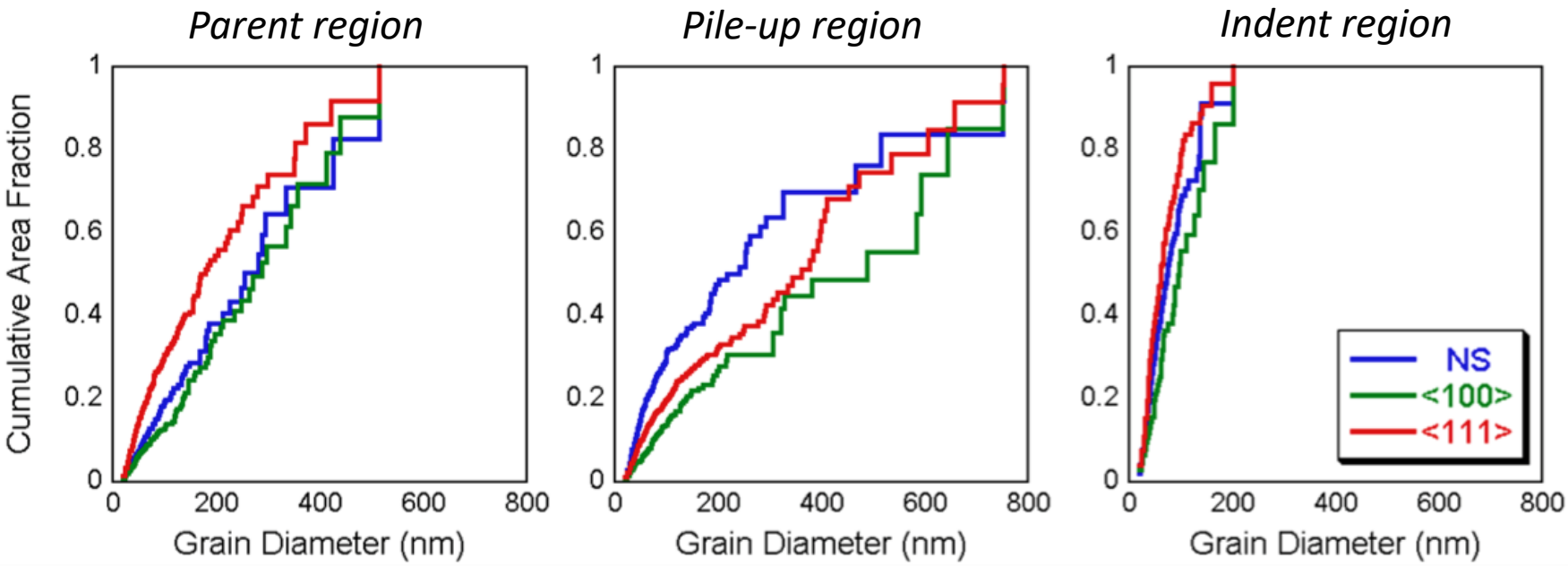

The ledges within the cumulative distribution plots are representative of grains that evolved from a mechanical load on the film

- All three films have similar grain size distributions in the parent and indented regions.
- **<100> NT Cu**: Initially 75% of the grains had a diameter < 400 nm. In the pile-up region, 45% of the grains had a grain size > 600 nm.
- **<111> NT Cu**: Initially more than 80% of the grains had a diameter < 400 nm. In the pile-up region, only 50% of the grains had a diameter < 400 nm. There was considerable grain growth, with 20% of the grains (by area) having a diameter > 600 nm.

Analyzing the CSL Boundary Evolution

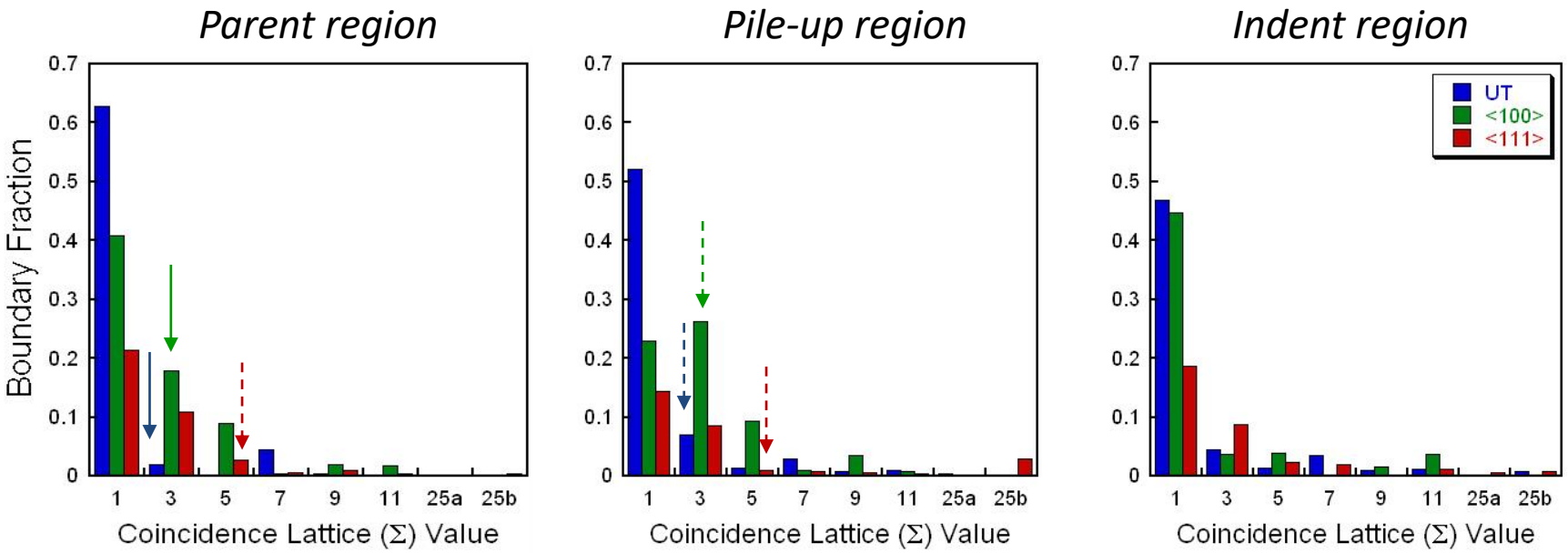

The pile-up regions show differences in boundary character-

UT & <100> NT: the fraction of the **Σ3 and Σ3 increases**

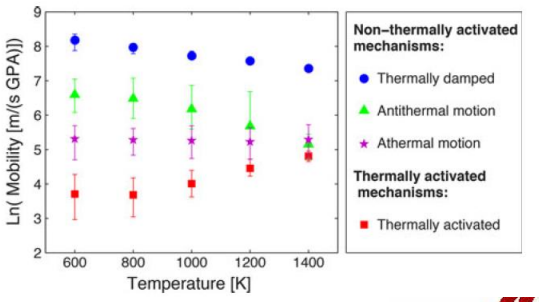

**Homer et al (JOM 2013) simulations even suggest some Σ GBs (some Σ3) could move anti-thermally*

<111> NT: reduction of Σ5

Brons, et al. *Materials Science and Eng. A 2013*

Σ1 : grains that are < 15 degrees

Why the Grain Growth?

Hint: the "loss" of Twin Boundaries

Parent material

High density of twins

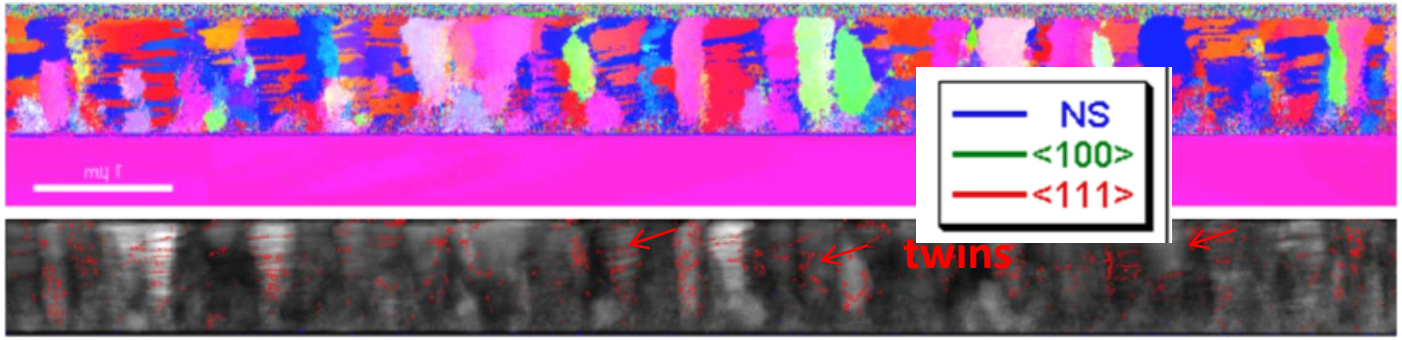

Indent material

No evidence of twins

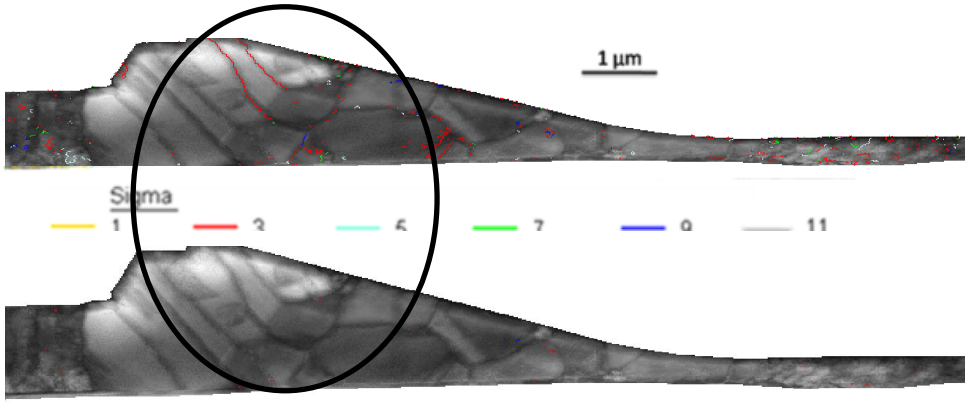

Within the pile up region, a decrease in twin boundaries was noted as compared to the parent material

A Possible De-twinning Mechanism?

Although twin boundaries are more resistant to migration than other boundaries, Chen *et al.** explained that apparent de-twinning processes are found to exist.

Dislocation arrays are often found at the migrating twin boundary front.

This allows **twin boundaries to annihilate locally and convert themselves into single dislocation lines through detwinning mechanisms**:

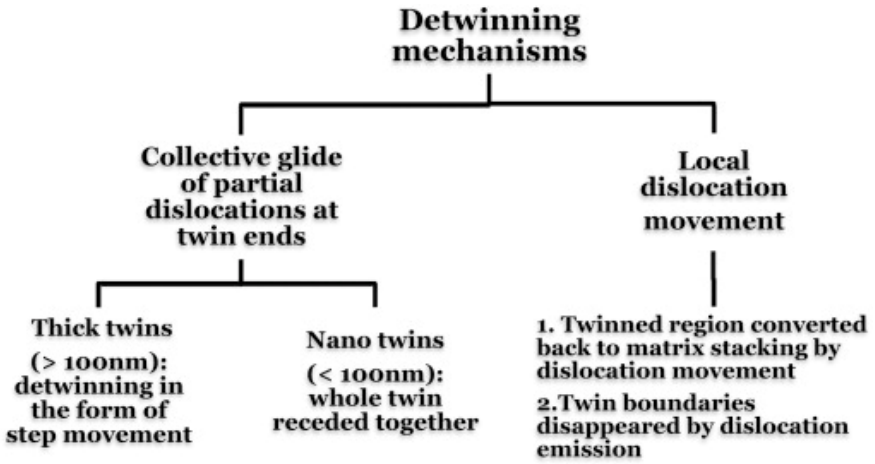

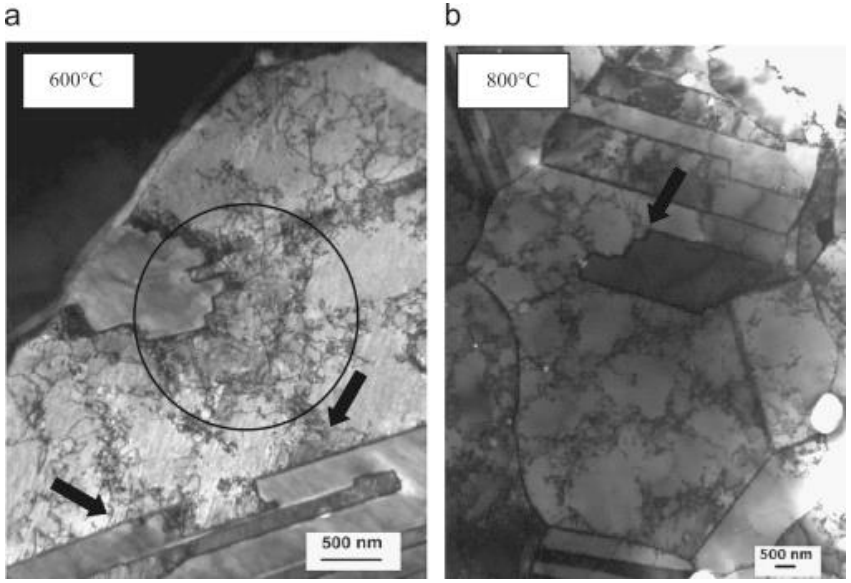

Wang *et al*. presented detwinning simulations.

The driving force for detwinning was attributed to the interaction between two twin boundaries, arising from the variation in the energy of the twin boundaries.

They also showed that shear stresses enable the twin boundaries to migrate easily.

*Chen *et al*. *Materials Science and Engineering A*. 2012.

Differences in De-twinning Grain Growth Sizes

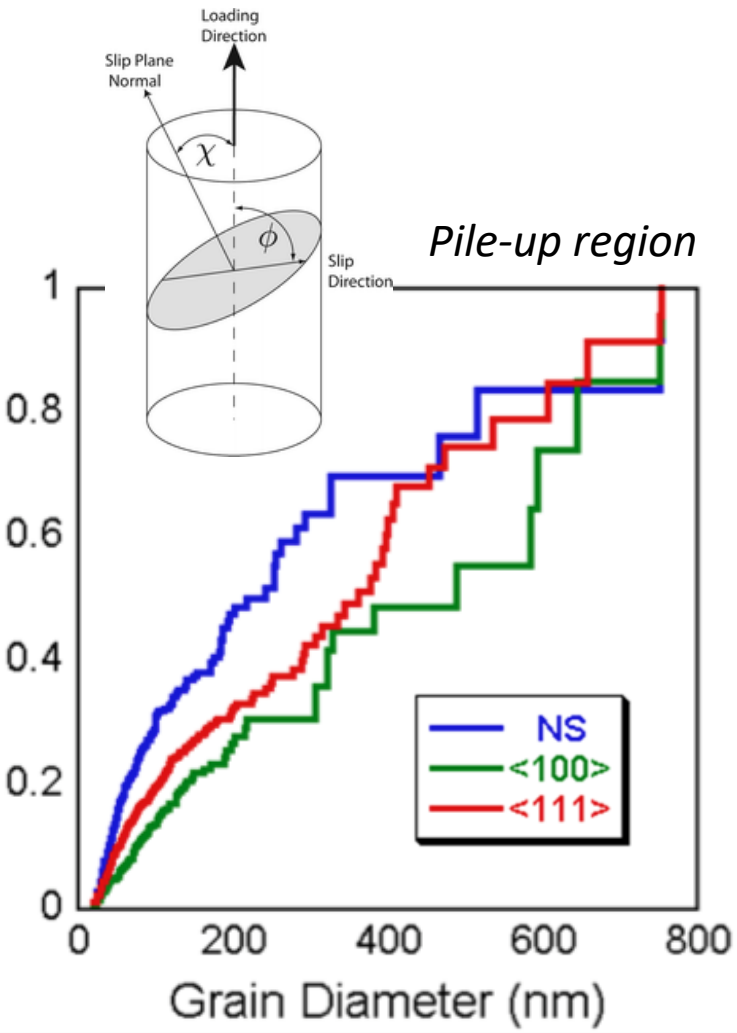

For the <100> orientated NT films, the twins (on {111} planes) would be inclined to the indentation normal to the surface

- Results in nonzero Schmid factor (appreciable stress) → more driving forces to de-twin (larger grains)

For <111> orientated NT films, the twins (on the {111} planes) would be normal to the indentation to the surface

- For a non-zero Schmid factor, the deformed material flowing along the flank of the indent would experience a complex stress state allowing stress to facilitate de-twinning; since this loading orientation was not at the original state

Where are we going: *in situ* Mechanical Tests

PI 95 TEM Indenter

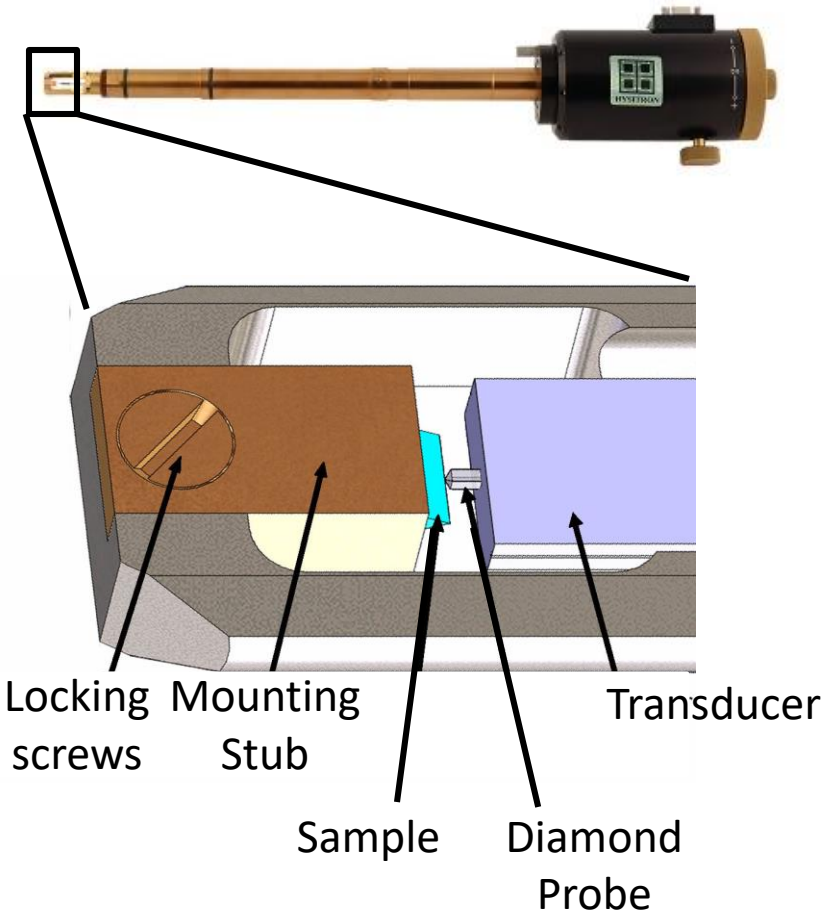

Sample preparation

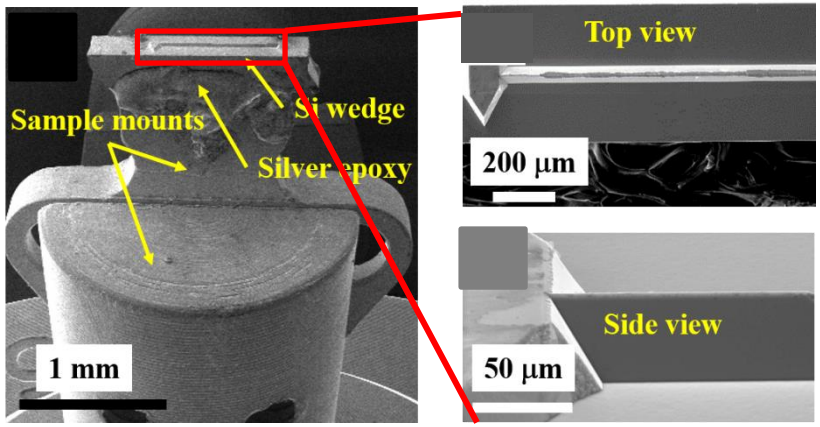

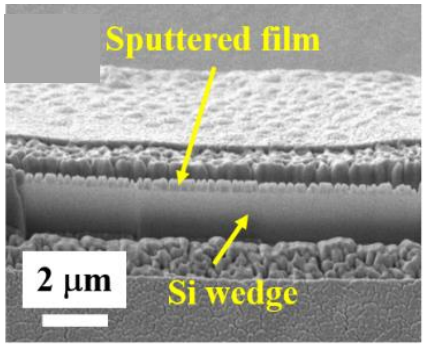

Indentation of Polycrystalline Cu film

~1.5 μm Cu film. Indentation depth 200 nm, speed 0.5 nm/s

10X indentation speed

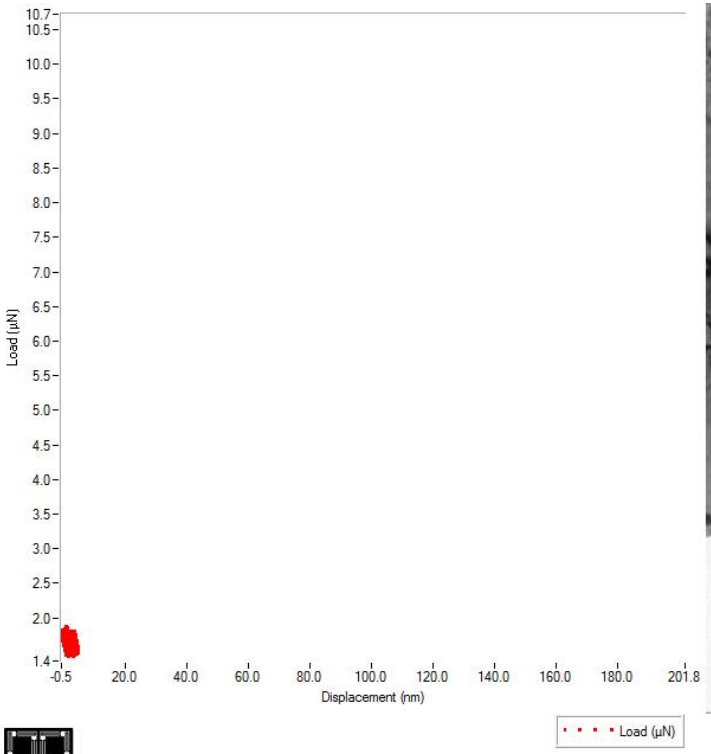

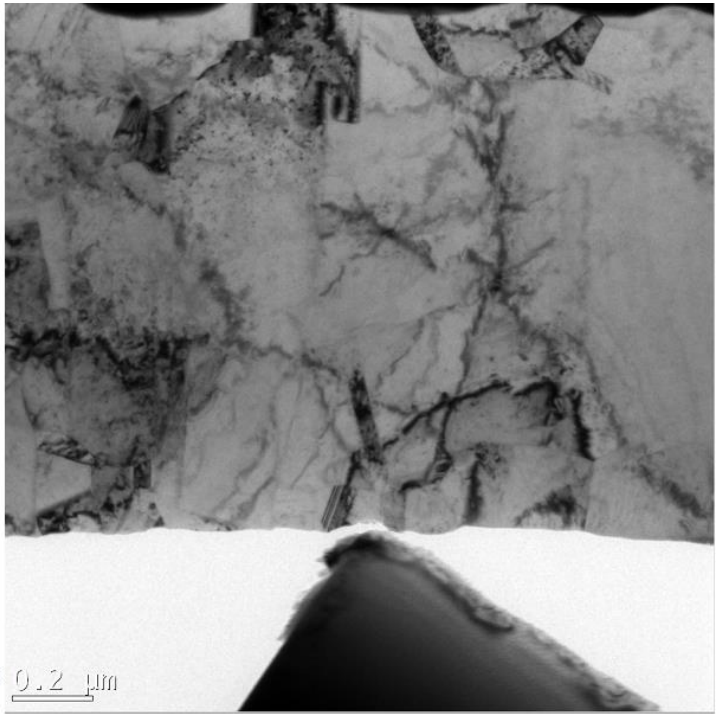

HYSITRON™

Indentation of Polycrystalline Cu film

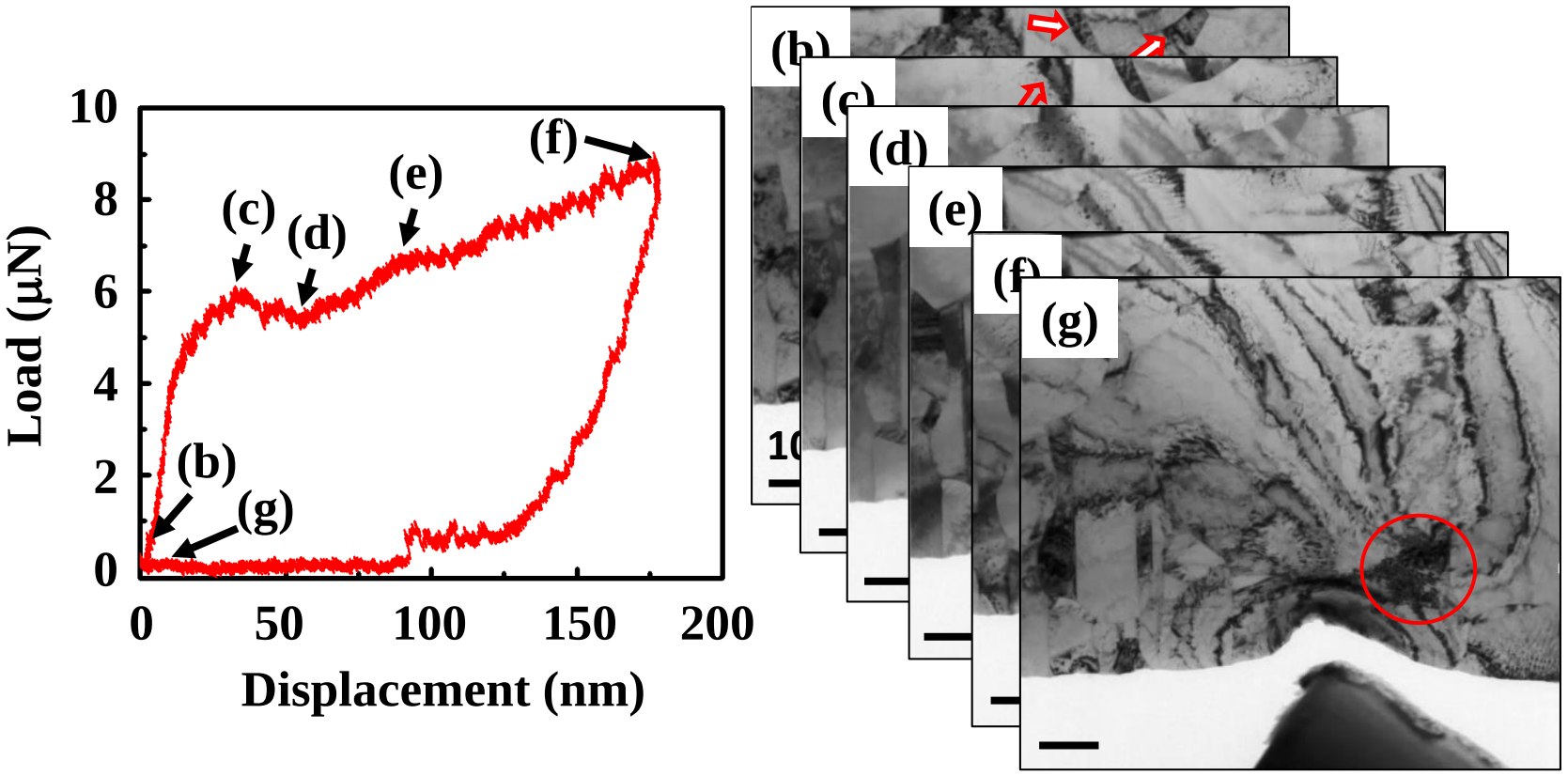

Bright field images:

1. Variable contrast will mask some of the microstructural features.
2. Qualitative results. Need a Quantitative analytical method.

PED Analysis: *revealing features through the diffraction contrast*

Pre-indentation

Post-indentation

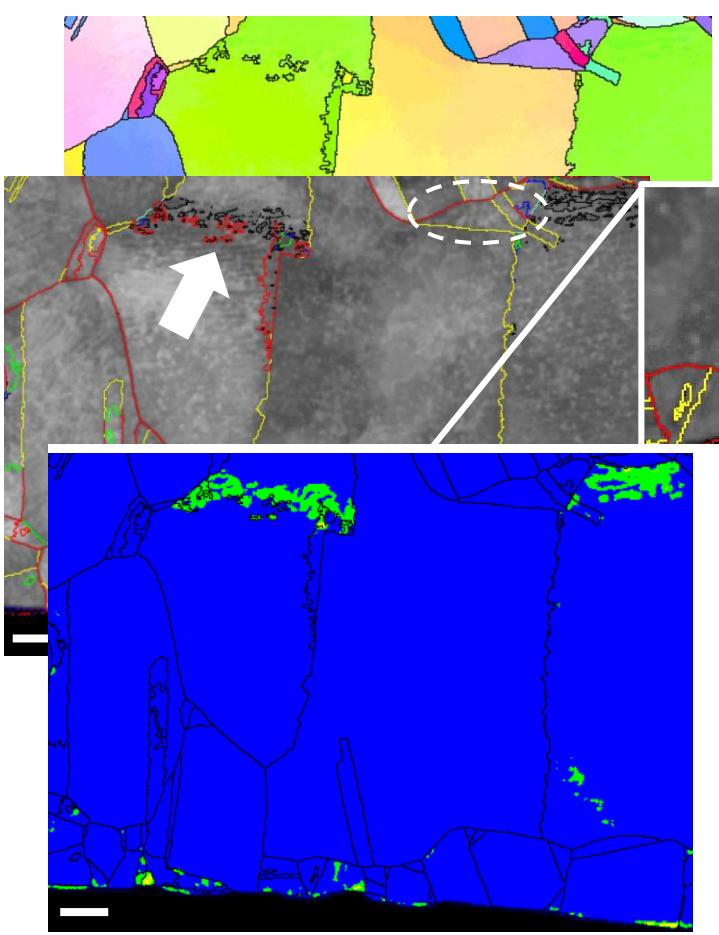

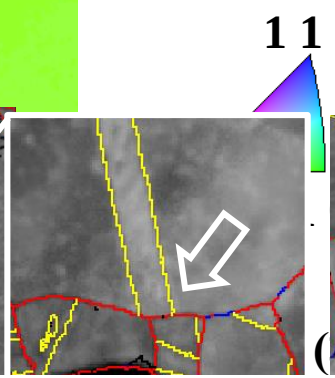

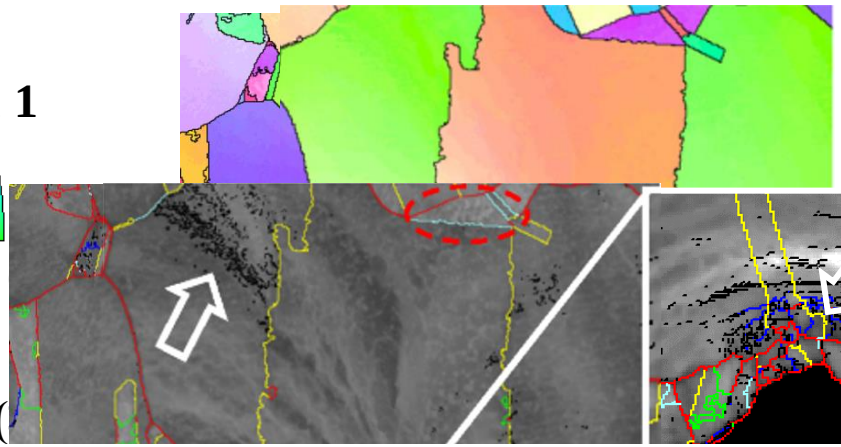

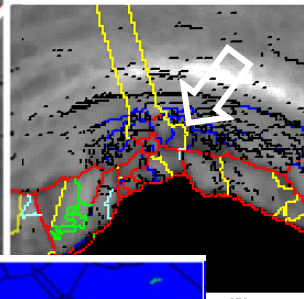

Min	Max
0	1.0
1.0	2.0
2.0	3.0
3.0	4.0

GBs (> 5°)

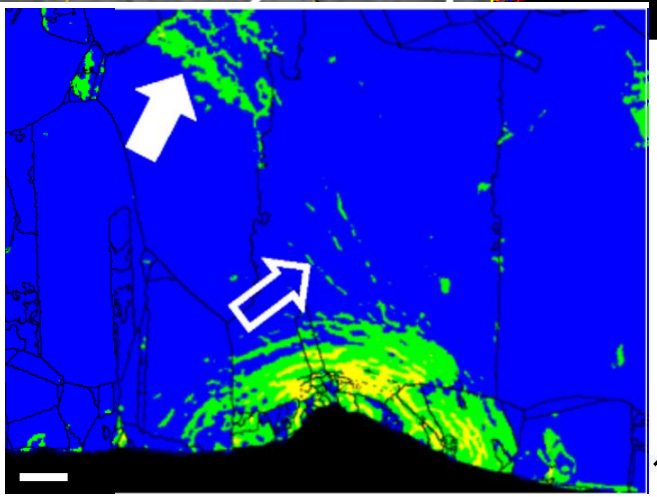

Guo and Thompson JOM 2018

Composite Crystalline/Glassy Nanolaminates

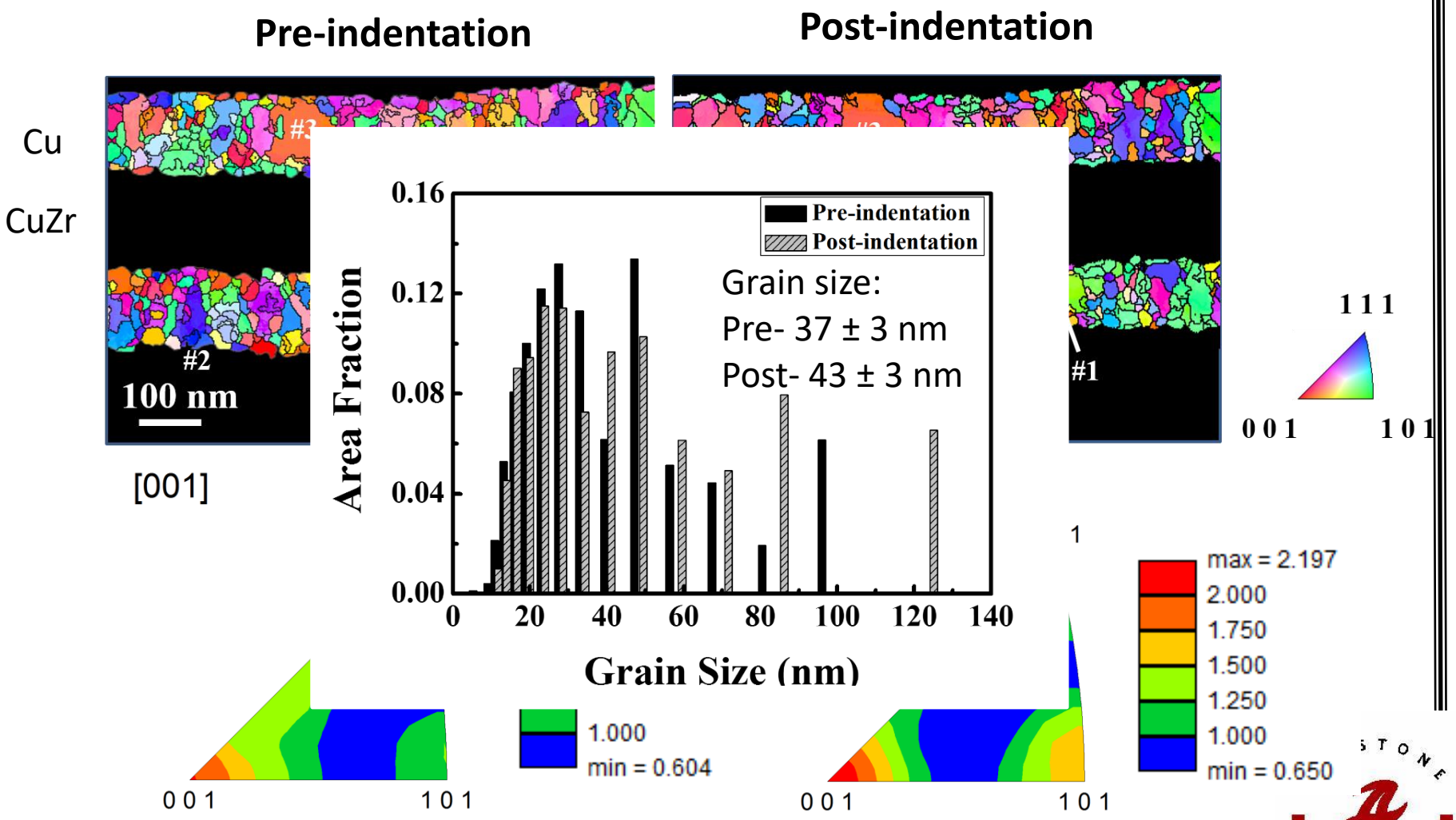

Summary

- PED provides a powerful means to understand stability in nanostructured materials
  - PED cross-correlative capability enables solute concentration to be linked to grain boundary types via APT
  - PED quantifies grain size and boundary evolution during early oxidation
  - PED to grain boundary (and size) stability under deformation (revealing what boundaries are critical and unmasking features lost in diffraction contrast)